2009

Enhancement of engine simulation using LES turbulence modeling and advanced numerical schemes

Yuanhong Li
Iowa State University

Enhancement of engine simulation using LES turbulence modeling and advanced numerical schemes

by

Yuanhong Li

A dissertation submitted to the graduate faculty

in partial fulfillment of the requirements for the degree of

DOCTOR OF PHILOSOPHY

Major: Mechanical Engineering

Program of Study Committee:
Song-Charng Kong, Major Professor
Theodore J. Heindel
Shankar Subramaniam
Zhijian Wang
Hailiang Liu

Iowa State University

Ames, Iowa

2009

DEDICATION

To my parents, Silai Li and Lianfeng Lin

TABLE OF CONTENTS

LIST OF TABLES

LIST OF FIGURES

NOMENCLATURE

Roman Symbols

a	acceleration or a pressure gradient scaling parameter for low Mach flow
$a_{1,2}, a_{4,3}, a_{c,cn}$	geometric coefficients
$\mathbf{A}_f$	face area vector
A_0	a switch for turbulent or laminar flow
A_{sf}	constant
B_0	constant
c_l	liquid specific heat
$C_{1,}C_2, C_3$	model coefficients or constants
C_b, C_d, C_e, C_F	constants
c_D	drag coefficient
C_m	constant
$C_{\varepsilon 1,}C_{\varepsilon 2}$	turbulent model constants
$C_k, C_\varepsilon, C_\mu, C_s$	constants
c_p	specific heat at constant pressure
C_{t1}, C_{t2}	coefficients for turbulent dissipation rate equation
c_v	specific heat at constant volume
d	droplet diamter

$D_{l,i}, D$	binary diffusion coefficients or material derivative
D_a	Damkohler number
D_c	gas diffusion coefficient
D_s	average particle diameter
e	specific internal energy
E	computational efficiency
f	probability density function
F_j^s	rate of momentum gain per unit volume due to spray
$\mathbf{g}$	gravity vector
G	filter function at the grid level
G_T	filter function at the test level
$\mathbf{i}, \mathbf{j}, \mathbf{k}$	unit vectors in x,y, z coordinate directions, respectively
I	specific internal energy
k	turbulent kinetic energy
k_1	a constant
K_g	thermal conductivity
L	latent heat of vaporization
L_A	turbulence length scale
L_b	breakup length
L_{ij}	Leonard stress tensor

$M_{C_2H_2}$	mass of acetylene
M_{ij}	a stress tensor
M_s, M_{sf}, M_{so}	masses of soot, soot formation and soot oxidation
Mw_c	soot molecular weight
$\hat{\mathbf{n}}$	outward unit normal vector
N	total number of species or cells or processors
n_{sc}	number of convective sub-cycles
Nu_d	Nusselt number
$h_s, h_{s,l}$	enthalpy
p	thermodynamic pressure
P_k	production term in turbulent kinetic energy equation
Pr	turbulent Prandtl number
q	molecular heat flux by conduction or generic cell-centered variable
Q	generic cell-centered variable
$\dot{Q}^c$	source term in energy equation due to chemical reactions
Q_d	rate of heat transfer to drop surface per unit area by conduction
$\dot{Q}^s$	source term in energy equation due to spray vaporization
$\dot{Q}_T$	general source term in energy equation
r	droplet radius in spherical shape
R	universal gas constant

r_{crit}	critical value for mesh refinement and coarsening
Re	Reynolds number
r_m	ratio of the total mass of liquid and vapor in a cell to total injected fuel mass
R_{Total}	surface mass oxidation rate
s	stoichiometric coefficient for a fuel
S	speedup
Sc	turbulent Schmidt number
S_{ij}	rate of strain tensor
$\|S\|$	magnitude of the rate of strain tensor
St	Stokes number
t	time
T	Taylor number or clock time
T_{ij}	'test' level stress tensor
u	velocity
u^*	modeled instantaneous velocity
V	computational cell volume
$\dot{W}^s$	rate of work done by turbulent eddies to disperse spray droplets
We_g	Weber number
x, y, z	coordinate direction
y	normalized droplet distortion
Y_l	species mass fraction

z	mixture fraction
Z	Ohnesorg number

Greek Symbols

α, β	constants for mesh refinement and coarsening
χ	scalar dissipation rate or a distribution
Δ	grid filter length
$\widehat{\Delta}$	test filter length
δ_{ij}	Kronecker delta function
δV_f	face volume change
$\Delta t, \Delta t_c$	a main computational timestep and a subcycle timestep
ε	turbulent dissipation rate
ε_{lij}	the alternating tensor
ϕ	a generic variable
κ_Δ	cut-off wave number
λ	thermal conductivity
Λ	wave length
μ	molecular or effective viscosity
μ_t	turbulent viscosity
∇	gradient operator
ν	molecular kinematic viscosity
ν_t	turbulent kinematic viscosity

$\dot{\omega}$	rate of chemical reaction
ω	turbulence frequency
Ω	wave growth rate
ρ	thermodynamic density
ρ_s	soot density
ϕ	a variable
π	a constant (=3.1415926)
σ	surface tension force
σ_{ij}	viscous stress tensor
$\sigma_k, \sigma_\varepsilon$	model constants
θ	combustion progress variable
τ	standard deviation
τ_A	turbulence time scale
$\tau_{c,j}$	indicator for mesh refinement and coarsening
τ_{coll}	turbulence correlation time
τ_{break}	droplet breakup time
τ_{burst}	bubble burst time
τ_e	eddy life time
$\tau_{F_{si}u_i}$	subgrid droplet-gas interaction
τ_{ij}	subgrid scale stress tensor
τ_r	droplet aerodynamic response time

$\tau_{u_i Y_l}$	subgrid turbulent species flux
$\tau_{u_i T}$	subgrid turbulent energy flux

Subscripts and superscripts

c	source term due to chemistry or child cell
drop	spray droplet
eff	effective
f	a face
F	fuel
g	gas phase
h	higher level child cell
hole	nozzle hole
inj	fuel injection
i, j, k	indices for Cartesian coordinates
l	index for species or liquid phase or lower level cell
L, L^0	Lagrangian phase at time n+1 and n, respectively
O	oxidizer
p	parent cell
P	product
rel	relative
s	source term due to spray or a surface
st	stoichiometric
T	matrix transpose

vap	vapor

Other Symbols

$\bar{}$	mean quantity of ensemble average or resolved scale of LES filtering in incompressible flows
~	mean quantity of Favre ensemble average or resolved scale of Favre filtered quantity in compressible flows
=	two times ensemble average or LES filtering in incompressible flows
≈	two times Favre ensemble average or Favre LES filtering in compressible flows
≋	three times Favre LES filtering in compressible flows
⌒	filtered quantity at the test filter level
'	fluctuation with respect to ensemble average, or subgrid scale component of filtered quantity
"	fluctuation with respect to Favre ensemble average, or subgrid scale component of Favre filtered quantity

Abbreviations

AMR	adaptive mesh refinement
ATDC	after top dead center
BDC	bottom dead center
CAD	crank angle degree
CFD	computational fluid dynamics
CHEMKIN	a chemistry solver that solves complex chemical kinetics problems

CO	carbon monoxide
DI	direct injection
DNS	direct numerical simulation
EGR	exhaust gas recirculation
EVO	exhaust valve open
ICEM-CFD	a commercial package for computational grid generation
IVC	intake valve close
KIVA	a computer code developed at Los Alamos National Laboratory
KIVA-3V	version 3 of KIVA computer code
KIVA-4	version 4 of KIVA computer code
LES,VLES	large eddy simulation, and very large eddy simulation, respectively
MPI	Message Passing Interface
METIS	a software package for parallel domain decomposition based on a multilevel recursive-bisection scheme
h METIS	a software package for parallel domain decomposition based on multilevel hypergraph partitioning schemes
NO	nitric oxide
NO_2	nitrogen dioxide
N_2O	nitrous oxide
NO_x	nitrogen oxides ($NO+NO_2$)
NS	Navier-Stokes
PDF	probability density function

PLII	planar laser induced incandescence
RANS	Reynolds Averaged Navier-Stokes
RNG	Renormalization group
RPM	reciprocation per minute
RSM	Reynolds stress models
SGS	subgrid scale
SOI	start of injection
TAB	Taylor analogy breakup
TDC	top dead center
TKE	turbulent kinetic energy

ACKNOWLEDGEMENTS

First and foremost, I would like to express my sincerest gratitude to my advisor, Professor Song-Charng Kong, for accepting me as his PhD student and for his guidance, encouragement, patience, and numerous other helps in various aspects. He not only broadened my knowledge of numerical simulation, combustion, and IC engine but also inspired me to overcome so many obstacles in my research. His thorough reviews on my papers and thesis also helped me greatly improve my writing skills. I am grateful to other committee members for their efforts and contributions to this work. Professor Theodore J. Heindel patiently read through my thesis manuscript and provided very detailed and critical comments on the improvement of my thesis. Professor Shankar Subramaniam provided me with useful knowledge of multiphase flow modeling and multi-scale modeling. Professor Zhijian Wang taught me various advanced numerical methods in CFD and provided insightful comments on the numerical schemes for adaptive mesh refinement. Professor Hailiang Liu served as representative of my Master minor from Mathematics Department and also taught me a great deal of knowledge about numerical analysis. Finally, I would like to thank Professor Richard H. Pletcher for accepting me into the PhD program in Mechanical Engineering and leading me into the field of LES turbulence modeling. Without their help, this work would not have been possible.

I am indebted to Dr. David J. Torres at Los Alamos National Laboratory for providing me important comments and help in the development of parallel AMR into KIVA-4. I would like

to thank other faculty, staff, and so many graduate students in Mechanical Engineering Department for their help throughout my study at ISU.

I am deeply indebted to my parents for their continual and strong support. I also thank other family members for their encouragement and great support.

This research was partially supported by Ames Laboratory, U.S. Department of Energy, and Ford Motor Company. The computer resources provided by the Iowa State High Performance Computing Group are also gratefully acknowledged.

ABSTRACT

The goal of this study is to develop advanced numerical models and algorithms to improve the accuracy of engine spray combustion simulation. This study developed a large eddy simulation (LES) turbulence model and adaptive mesh refinement (AMR) algorithms to enhance the accuracy and computational efficiency of engine simulation.

The LES approach for turbulence modeling is advantageous over the traditional Reynolds Averaged Navier Stokes (RANS) approach due to its capability to obtain more detailed flow information by resolving large-scale structures which are strongly geometry dependent. The current LES approach used a one-equation, non-viscosity, dynamic structure model for the sub-grid stress tensor and also used a gradient method for the sub-grid scalar fluxes. The LES implementation was validated by comparing the predicted spray penetrations and structures in a non-evaporating diesel spray. The present LES model, when coupled with spray breakup and detailed chemistry models, were able to predict the overall cylinder pressure history, heat release rate data, and the trends of NO_x and soot emissions with respect to different injection timings and EGR levels in a heavy-duty diesel engine. Results also indicated that the LES model could predict the unsteadiness of in-cylinder flows and have the potential to provide more detailed flow structures compared to the RANS model.

AMR algorithms were also developed to improve transient engine spray simulation. It is known that inadequate spatial resolution can cause inaccuracy in spray simulation using the stochastic Lagrangian particle approach due to the over-estimated diffusion and inappropriate

liquid-gas phase coupling. Dynamic local mesh refinement, adaptive to fuel spray and vapor gradients, was developed to increase the grid resolution in the spray region. AMR was parallelized using the MPI library and various strategies were also adopted in order to improve the computational efficiency, including timestep control, reduction in search of the neighboring cells on the processor boundaries, and re-initialization of data at each adaptation. The AMR implementation was validated by comparing the predicted spray penetrations and structures. It was found that a coarse mesh using AMR could produce the same results as those using a uniformly fine mesh with substantially reduced computer time. The parallel performance using AMR varied depending on the geometry and simulation conditions. In general, the computations without valve motion or using a fine mesh could obtain better parallel performance than those with valve motion or using a coarse mesh.

1 INTRODUCTION

1.1 Background

Internal combustion engines will continue to be the main power source in the foreseeable future for transportation, off-road machinery, ships, and many other applications despite that alternative power sources are being developed. Internal combustion engines have been faced with tremendous challenges in meeting increasingly stringent emissions regulations and requirements for power density and fuel efficiency. These challenges have drawn extensive interests in exploring various ways to improve combustion efficiency and reduce pollutant emissions. Various strategies such as multiple fuel injections, low temperature combustion, homogeneous charge compression ignition (HCCI) operation, alternative fuels, and exhaust gas aftertreatment are investigated to achieve more efficient combustion and lower pollutant emissions. Both experiments and modeling are necessary tools to conduct the investigations. Numerical simulation can provide results faster and cheaper, and can give extensive information about the complex in-cylinder processes as shown in **Figure 1.1**. Numerical simulation can also be used to investigate processes that take place at time and length scales or in places that are not accessible using experimental techniques. Therefore, numerical simulation has become a necessary complement to experiments in developing advanced engine technologies. Today, the complex task of developing advanced mixture formation and combustion strategies can only be achieved with a combination of experimental and numerical studies

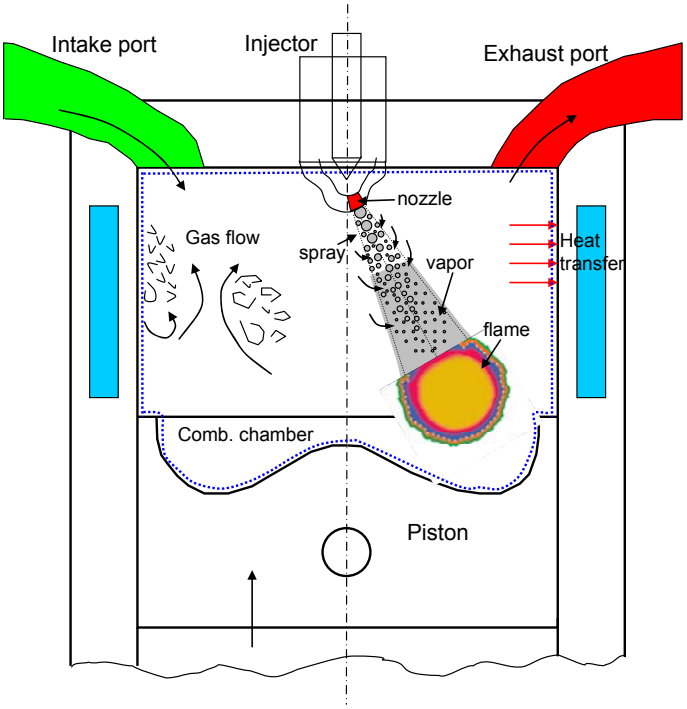

Figure 1.1. Schematic of in-cylinder processes in a diesel engine.

Three classes of models have been used to perform numerical simulation of internal combustion engines ranging from zero-dimensional thermodynamic models, one-dimensional phenomenological models to three-dimensional computational fluid dynamics (CFD) models in the order of increasing complexity. The thermodynamic model describes only the most relevant processes without considering any spatial resolution and cannot provide insight into the local flow details. The phenomenological model considers quasi-spatial resolution of the combustion chamber and uses appropriate sub-models to approximate the relevant processes such as mixture formation, ignition and combustion. This model may be used to predict the global heat release rate and overall engine performance. The CFD model solves the discretized set of Navier-Stokes equations in combination with an appropriate turbulence model, wall heat transfer models, and spray combustion models for chemically reactive flows

with sprays. This model takes into account every process of interest. For instance, the processes of fuel injection, liquid breakup and drop evaporation, collisions, and wall impingement are simulated using various submodels. These models can provide detailed information of the processes in time and space. This rich information makes the CFD model particularly suited for investigating the effects of the in-cylinder processes on engine performance. Compared to the other two simpler models, the CFD model consumes significantly more computer time and memory. It is necessary to develop high-fidelity models with high computational efficiency.

1.2 Motivation

Appropriate mixture preparation is critical for achieving efficient combustion and low emissions, especially in direct-injection engines. Mixture formation is determined by the interaction of the spray and the in-cylinder flow, which in turn is determined by the intake port and combustion chamber geometry. Accurate modeling of mixture distribution requires appropriate simulation of the flow field. Large eddy simulation (LES) turbulence modeling can offer improved simulation of the in-cylinder flow process and is a promising approach for more accurate engine simulation.

In the LES modeling, all the scales larger than the computational grid size are directly solved by a space- and time-accurate method while the effects of scales below the grid size are modeled using sub-grid models. LES requires models for sub-grid scale physical processes that occur below the grid resolution. An important example includes the chemical process of

pollutant formation. Traditionally, LES has focused only on modeling the turbulent sub-grid stresses. However, engine applications are unique in the turbulence community and require a much broader range of sub-grid models including scalar mixing, spray dynamics, drop vaporization, combustion, and emissions. For instance, sub-grid modeling of the scalar dissipation rate plays an important role in predicting mixing since the scalar dissipation is used for representing sub-grid distributions of scalar fields in the probability density function modeling and also the sink term in the scalar variance transport equation. The LES filtering also gives rise to the unclosed terms due to engine spray and combustion chemistry, which still pose modeling difficulties. Thus, research is needed to develop an adequate LES turbulence model that can be used for engine simulation.

On the other hand, the most common spray description is the Lagrangian discrete particle method based on Dukowicz's technique (Dukowicz, 1980), in which the properties of representative droplet parcels are randomly chosen from theoretical distribution functions. The continuous gaseous phase is described by an Eulerian method. Spray-gas interactions are achieved by the coupling of source terms for the exchange of mass, momentum, and energy. Numerical studies have indicated that spray simulation using the stochastic Lagrangian discrete method is sensitive to the grid resolution and grid arrangement (Abraham, 1997; Aneja and Abraham, 1998; Subramaniam and O'Rourke, 1998; Beard et al., 2000; Schmidt and Rutland, 2000; Hieber, 2001; Are et al., 2005; Tonini et al., 2008). This grid dependence can be partially attributed to the inadequate spatial resolution of the coupling between the gas and liquid phases. In a region near the injector exit, velocity and species density gradients can be strong when a high-velocity spray is injected into a slowly

moving gas. Inadequate spatial resolution of the spray in this region can result in a much higher relative velocity between the two phases and an over-estimation of diffusion (Stiesch, 2003; Baumgarten, 2006). Thus, it is often required to use a fine mesh in the region near the nozzle exit to improve spray modeling while using a coarser mesh away from the nozzle exit to save computer time.

The grid dependence has also been shown to be a result of the sub-models for spray simulations (Aneja and Abraham, 1998; Schmidt and Rutland, 2000; Hieber, 2001; Are et al., 2005). While improving the sub-models to reduce the grid dependence has attracted much attention (Hieber, 2001; Schmidt and Rutland, 2004; Are et al., 2005; Tonini et al., 2008), the improvements may still be subject to further validation and tuning of model constants for specific conditions. Another way to reduce grid dependence is to increase the local spatial resolution in the spray region. Adaptive mesh refinement (AMR) (Bell et al., 1994a; Wang and Chen, 2002; Anderson et al., 2004; Lippert et al., 2005) can be utilized to increase the spatial resolution in the spray region to improve the phase coupling and thus alleviate the mesh dependence without incurring much computer time. In particular, AMR can provide a greater flexibility of adapting to highly transient spray with adequate spatial resolution that otherwise would not be readily available if a uniform mesh is used.

1.3 Objectives

The objectives of this study are twofold. The first objective is to develop large eddy simulation (LES) to improve modeling of in-cylinder flow and combustion in diesel engines.

The second objective is to develop parallel adaptive mesh refinement algorithms to increase the spatial resolution in the spray region to improve the accuracy and computational efficiency of spray modeling.

2 LITERATURE REVIEW

2.1 Introduction

CFD models have been widely used for three-dimensional simulation of fluid flow, mixture formation, combustion, and pollutant formation in combustion systems. This chapter presents a review of the physical and chemistry models that are relevant to engine simulation. These models include those for turbulence, spray, combustion, and emissions. Additionally, numerical schemes for adaptive mesh refinement and parallel computing are also reviewed.

2.2 Turbulence Modeling

Turbulent flows in internal combustion engines are characterized by a wide range of length and time scales (Reynolds, 1980). The length scale varies from the smallest Kolmogorov scale to the largest integral scale comparable to the engine geometry. Widely varying time scales exist and are associated with different flow structures such as homogeneous flows, shear layers, boundary layers, and re-circulations (Reynolds, 1980). Depending on the resolution of the turbulence energy spectrum, turbulent modeling can be divided into three categories: Reynolds Averaged Navier-Stokes (RANS) approach, large eddy simulation (LES), and direct numerical simulation (DNS). The RANS approach only resolves the mean flow fields whereas models the turbulence energy, and it is computationally more efficient than the other two approaches. The LES approach resolves the large scales of the turbulence at the level of the computational grid size and requires sub-grid models to model the effects of smaller scales. The DNS approach resolves the smallest eddies in a flow field without

averaging or using turbulence models, and it is computationally expensive. DNS simulations have been limited to basic research applications with low Reynolds numbers and small geometric domains. The fundamentals of governing equations of RANS and LES approaches will be presented as follows. The instantaneous conservation equations for mass, species, momentum and enthalpy in a turbulent reacting flow are expressed as (Kuo, 1986)

$$\frac{\partial \rho}{\partial t} + \frac{\partial \left(\rho u_j \right)}{\partial x_j} = 0 \tag{2.1}$$

$$\frac{\partial \left(\rho Y_l \right)}{\partial t} + \frac{\partial \left(\rho u_j Y_l \right)}{\partial x_j} = -\frac{\partial \left(D_{l,j} Y_l \right)}{\partial x_j} + \dot{\omega}_l \quad \left(l = 1, N \right) \tag{2.2}$$

$$\frac{\partial \rho u_i}{\partial t} + \frac{\partial \left(\rho u_l u_j \right)}{\partial x_j} = -\frac{\partial p}{\partial x_i} + \frac{\partial \sigma_{ij}}{\partial x_j} \tag{2.3}$$

$$\frac{\partial \left(\rho h_s \right)}{\partial t} + \frac{\partial \left(\rho u_j h_s \right)}{\partial x_j} = \frac{\partial p}{\partial t} + u_j \frac{\partial p}{\partial x_j} + \frac{\partial}{\partial x_j}\left(\lambda \frac{\partial T}{\partial x_j} \right) - \frac{\partial}{\partial x_j}\left(\rho \sum_{l=1}^{N} D_{l,j} Y_l h_{s,l} \right) + \sigma_{ij} \frac{\partial u_i}{\partial x_j} + \dot{Q}_T \tag{2.4}$$

where ρ is gas density, Y_l is mass fraction for species l, u is velocity, $D_{l,j}$ is the binary mass diffusion coefficients, $\dot{\omega}_l$ is chemical reaction rate for species l, p is static pressure, σ_{ij} is the rate of stress tensor, h_s is total specific enthalpy, λ is the thermal conductivity, x is coordinate, and t is time. In Eq. (2.4), on the right hand side, the first two terms represent the material derivative of the pressure, the third and fourth terms represent heat flux due to conduction and enthalpy diffusion, respectively, the fifth term is viscous dissipation, and the last term is a source term. The source term $\dot{Q}_T$ in the energy equation accounts for the contributions from the heat release from combustion, and heat transfer between the liquid droplets and the gas phase. The heat transfer due to radiation is generally neglected in engine

modeling due to the following reasons. First, the combustion duration (e.g., 40~50 CAD) is relatively short compared to the entire engine cycle (i.e., 720 CAD). During diesel combustion at high-load conditions, luminous flame due to soot radiation generally only lasts for 20 to 30 CAD, and the effects of radiative heat transfer on total wall heat loss was not significant, particularly in part-load conditions (Wiedenhoefer and Reitz, 2003). There were only very limited studies that considered radiative heat transfer in engine simulation partly due to the complexity of the integro-differential equations associated with thermal radiation (Libby and Williams, 1980; Coelho, 2007).

RANS approach

Most turbulence model development has been based on the RANS approach. Following the basic approach of Reynolds, the instantaneous value of the turbulent flow quantity ϕ is split into a mean $\overline{\phi}$ and a fluctuating component ϕ'

$$\phi = \overline{\phi} + \phi' . \tag{2.5}$$

$\overline{\phi}$ is an ensemble-averaged quantity, e.g., $\overline{\phi} = \frac{1}{M}\sum_{i=1}^{M}\phi_i$. For statistically steady flows, it is the time-averaged and defined by

$$\overline{\phi} = \frac{1}{\Delta t}\int_{t}^{t+\Delta t}\phi(x,t)\,dt . \tag{2.6}$$

For compressible flows, mass-weighted averages or Favre averages are often introduced to avoid unclosed correlations between any quantity ϕ and density fluctuations, and the situation of unconserved mass resulting from the above Reynolds averages (Kuo, 1986). The Favre average is defined as

$$\tilde{\phi} = \frac{\overline{\rho\phi}}{\bar{\rho}}. \tag{2.7}$$

The Favre-average is used for all flow quantities except for pressure and density whose averages are obtained using the Reynolds average. Then a quantity ϕ can be expressed as its Favre average $\tilde{\phi}$ and fluctuating component ϕ'' as

$$\phi = \tilde{\phi} + \phi'' \quad \text{with} \quad \overline{\phi''} = 0 \tag{2.8}$$

Substituting these decomposition terms into the original Navier-Stokes equations yields the RANS equations as follows.

$$\frac{\partial \bar{\rho}}{\partial t} + \frac{\partial\left(\bar{\rho}\tilde{u}_j\right)}{\partial x_j} = 0 \tag{2.9}$$

$$\frac{\partial\left(\bar{\rho}\tilde{Y}_l\right)}{\partial t} + \frac{\partial\left(\bar{\rho}\tilde{u}_j\tilde{Y}_l\right)}{\partial x_j} = -\frac{\partial}{\partial x_j}\left(\overline{D_{l,j}Y_l} + \bar{\rho}\widetilde{u_j''Y_l''}\right) + \bar{\dot{\omega}}_l \quad \left(l = 1, N\right) \tag{2.10}$$

$$\frac{\partial \bar{\rho}\tilde{u}_i}{\partial t} + \frac{\partial\left(\bar{\rho}\tilde{u}_i\tilde{u}_j\right)}{\partial x_j} = -\frac{\partial \bar{p}}{\partial x_i} + \frac{\partial}{\partial x_j}\left(\bar{\sigma}_{ij} - \bar{\rho}\widetilde{u_i''u_j''}\right) \tag{2.11}$$

$$\frac{\partial\left(\bar{\rho}\tilde{h}_s\right)}{\partial t} + \frac{\partial\left(\bar{\rho}\tilde{u}_j\tilde{h}_s\right)}{\partial x_j} = \frac{\partial \bar{p}}{\partial t} + \overline{u_j\frac{\partial p}{\partial x_j}} + \frac{\partial}{\partial x_j}\left(\overline{\lambda\frac{\partial T}{\partial x_j}} - \bar{\rho}\widetilde{u_j''h_s''}\right) - \frac{\partial}{\partial x_j}\left(\overline{\rho\sum_{l=1}^{N} D_{l,j}Y_l h_{s,l}}\right) + \overline{\sigma_{ij}\frac{\partial u_i}{\partial x_j}} + \bar{\dot{Q}}_T \tag{2.12}$$

where

$$\overline{u_j\frac{\partial p}{\partial x_j}} = \tilde{u}_j\frac{\partial \bar{p}}{\partial x_j} + \overline{u_j''\frac{\partial p}{\partial x_j}} \tag{2.13}$$

Some terms in the above equations are the results of Favre-averaging and highly nonlinear and require additional closure terms. The most famous terms among them are Reynolds

stresses $\widetilde{u_i'' u_j''}$, species turbulent flux $\widetilde{u_j'' Y_l''}$ and enthalpy turbulent flux $\widetilde{u_j'' h_s''}$, and chemical reaction rates $\bar{\dot{\omega}}_l$.

The Reynolds stresses $\widetilde{u_i'' u_j''}$ must be closed by a turbulence model. Boussinesq (1877) assumed that the apparent turbulent shearing stresses might be related to the rate of mean strain through an apparent scalar turbulent viscosity (Tennekes and Lumley, 1972; Hinze, 1975; Tannehill et al., 1997). Turbulence models can fall into two categories depending on whether the Boussinesq assumption was applied. The models using this assumption are called turbulent viscosity models or first-order models. Models without using this assumption are called Reynolds stress models (RSM) or second-order closures.

Following the Boussinesq assumption, the Reynolds stresses are generally modeled using the constitutive relation for Newtonian fluids

$$\widetilde{u_i'' u_j''} = -\nu_t \tilde{S}_{ij} + \frac{2}{3}\delta_{ij} k \tag{2.14}$$

where $\nu_t = \mu_t / \bar{\rho}$ is the eddy viscosity, $\tilde{S}_{ij}$ is the rate of strain tensor,

$$\tilde{S}_{ij} = \frac{1}{2}\left(\frac{\partial \tilde{u}_i}{\partial x_j} + \frac{\partial \tilde{u}_j}{\partial x_i} \right), \tag{2.15}$$

δ_{ij} is the Kronecker delta function. k is the turbulent kinetic energy and defined as

$$k = \frac{1}{2}\widetilde{u_i'' u_i''} \tag{2.16}$$

The eddy viscosity ν_t is unknown and requires a closure. Typical approaches to close this term include algebraic or zero-equation expressions, one-equation closure, and two-equations closure.

A typical zero-equation model is the Prandtl mixing length model. In this model, the scalar eddy viscosity is linked to the velocity gradient via an algebraic expression. Prandtl and Kolmogorov (1940s) suggested that the characteristic velocity of turbulence be proportional to the square root of the turbulent kinetic energy, which leads to so-called one-equation model.

The most popular turbulence models in RANS approach are the class of two-equation models. Among them, the $k-\varepsilon$ model is the most widely used due to its simplicity and cost effectiveness. This model allows the characteristic length scale l_c to vary depending on the flow. The scalar eddy viscosity is modeled using the length scale determined from the turbulent kinetic energy and its dissipation rate (Jones and Launder, 1972) as

$$\nu_t = C_\mu \frac{k^2}{\varepsilon}. \tag{2.17}$$

The turbulent kinetic energy k and its dissipation rate ε are described by two transport equations as follows

$$\frac{\partial(\bar{\rho}k)}{\partial t} + \frac{\partial(\bar{\rho}\tilde{u}_j k)}{\partial x_j} = \frac{\partial}{\partial x_j}\left[\left(\mu + \frac{\mu_t}{\sigma_k}\right)\frac{\partial k}{\partial x_j}\right] + P_k - \bar{\rho}\varepsilon, \tag{2.18}$$

$$\frac{\partial(\bar{\rho}\varepsilon)}{\partial t} + \frac{\partial(\bar{\rho}\tilde{u}_j \varepsilon)}{\partial x_j} = \frac{\partial}{\partial x_j}\left[\left(\mu + \frac{\mu_t}{\sigma_\varepsilon}\right)\frac{\partial \varepsilon}{\partial x_j}\right] + C_{\varepsilon 1} P_k \frac{k}{\varepsilon} - C_{\varepsilon 2}\bar{\rho}\frac{\varepsilon^2}{k} \tag{2.19}$$

where P_k is the production term and is given by

$$P_k = -\bar{\rho}\widetilde{u_i'' u_j''}\frac{\partial u_i}{\partial x_j} \tag{2.20}$$

Standard values of the model constants are also used in engine calculations (Amsden et al., 1989) since these values are chosen based on analytical solutions to the model in order to meet certain experimental constraints (Durbin and Reif, 2001). The standard values are given as

$$C_\mu = 0.09; \quad \sigma_k = 1.0; \quad \sigma_\varepsilon = 1.3; \quad C_{\varepsilon 1} = 1.44; \quad C_{\varepsilon 2} = 1.92\,. \tag{2.21}$$

This model can readily provide turbulent time and length scale estimates that can be used in turbulent combustion models. Other two-equation models have been developed using various combinations of k and ε to derive alternative transport equations to replace the equations for ε. For instance, the $k-\omega$ solves the transport equation for turbulence frequency $\omega = \varepsilon / k$ in place of the dissipation rate (Wilcox, 1993). One advantage of the $k-\omega$ model over the $k-\varepsilon$ model is its treatment of the near-wall region in boundary layer flows, especially for low Reynolds number flows (Wilcox, 1993).

Turbulence models based on the turbulent viscosity hypothesis may not perform well in complex flows, i.e., flows with significant streamline curvature or mean pressure gradients. The general $k-\varepsilon$ model assumes isotropic turbulence but practical flows often exhibit strong anisotropic features. Corrections based on non-linear turbulent viscosity models have proven to be useful for predicting secondary flows. But their accuracy still needs to be verified in predicting more complex flows such as with strong mean streamline curvature and/or rapid changes in the mean velocity (Pope, 2000). More sophisticated models have also

been proposed such as the second order Reynolds stress models (RSM) (Launder, 1996). Nonetheless, the traditional two-equation $k-\varepsilon$ models are still widely used in engine applications.

LES approach

In turbulent flows, energy-containing scales (the largest scales) determine most of the flow-dependent transport properties while energy-dissipating scales (the smallest scales) exhibit more universal and isotropic characteristics (Hinze, 1975; Pope, 2000; Durbin and Reif, 2001; Fox, 2003). It is also observed that the energy-containing scales can be modeled independently of the universal energy-dissipating scales given a model for the flux of energy through the inertial range. Therefore, the objective of the large eddy simulation approach is to explicitly resolve the largest scales of the flow field whereas the effects of the smallest ones are modeled. At high enough Reynolds number, it is expected that the small scales will be flow-independent, and thus that they can be successfully modeled by an appropriate subgrid scale (SGS) model.

LES is based on the decomposition of a flow variable into resolved and unresolved (sub-grid scale) terms. For any flow variable ϕ, it can be decomposed as

$$\phi = \overline{\phi} + \phi' \tag{2.22}$$

where $\overline{\phi}$ is the filtered quantity (or resolved scale) and ϕ' is the sub-grid scale (or unresolved scale) quantity. Note that the filtered quantity $\overline{\phi}$ is different than the Reynolds averaged $\overline{\phi}$

in the RANS approach which is an ensemble averaged value. The filtered quantity $\overline{\phi}$ is defined through the use of a filtering function in spectral space or in physical space as

$$\overline{\phi}(\mathbf{x},t) = \int_V G(\mathbf{x}-\mathbf{y})\phi(\mathbf{y},t)d\mathbf{y} \tag{2.23}$$

where $G(\mathbf{x}-\mathbf{y})$ is the filter function which should be smooth, rotationally symmetric, and satisfy the normalization condition

$$\int_V G(\mathbf{y})d\mathbf{y} = 1. \tag{2.24}$$

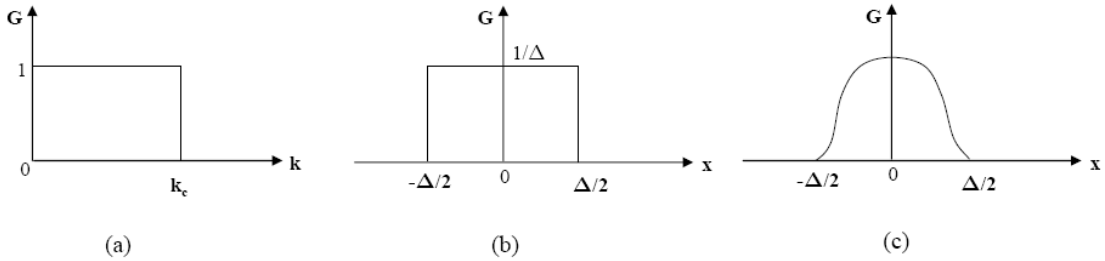

Figure 2.1. Typical filters used in LES. (a) cut-off filter in spectral space; (b) box filter in physical space; (c) Gaussian filter in physical space.

Commonly used spatial filter functions include wave number cut-off filter, 'box' filter, and Gaussian filter (Poinsot and Veynante, 2001; Berselli et al., 2006; Sagaut, 2006) as shown in **Figure 2.1**. The wave number cut-off filter is used for LES in spectral space and is defined as

$$G(k) = \begin{cases} 1 & k \le \kappa_\Delta \left(= \pi/\Delta\right), \\ 0 & \text{otherwise.} \end{cases} \tag{2.25}$$

For this filter, all wave numbers below a cut-off, κ_Δ, are resolved, while all wave numbers above the cut-off are modeled.

The 'box' filter is given by

$$G(\mathbf{x}) = \begin{cases} 1/V & |x_i| \le \Delta/2, i = 1,2,3 \\ 0 & \text{otherwise} \end{cases} \tag{2.26}$$

where Δ is the filter length and V is the volume defined by the filter length. The Gaussian filter is given by

$$G(\mathbf{x}) = \left(\frac{\lambda}{\pi\Delta^2}\right)^{3/2} \exp\left(-\frac{\lambda}{\Delta^2}|\mathbf{x}|^2\right) \tag{2.27}$$

where λ is a constant commonly taken to be 6.

For variable density ρ, a mass-weighted Favre filtering is introduced according to

$$\bar{\rho}\tilde{\phi}(\mathbf{x},t) = \int_V \rho G(\mathbf{x}-\mathbf{y})\phi(\mathbf{y},t)d\mathbf{y}\,. \tag{2.28}$$

Then, an instantaneous flow variable ϕ is decomposed into $\phi = \tilde{\phi} + \phi''$ where ϕ'' is the subgrid Favre-filtered component.

Note that the LES filtering has different properties than the RANS averaging, for instance,

$$\bar{\bar{\phi}} \neq \bar{\phi} \quad \text{and} \quad \overline{\phi'} \neq 0\,, \tag{2.29}$$

and

$$\tilde{\tilde{\phi}} \neq \tilde{\phi} \quad \text{and} \quad \widetilde{\phi''} \neq 0\,. \tag{2.30}$$

Besides, the derivation of balance equations for the filtered variables $\bar{\phi}$ or $\tilde{\phi}$ requires the exchange of filter and derivative operators. This exchange is valid only under restrictive assumptions. For instance, the filtering operation only commutes with differentiation for a uniform stationary grid (Ghosal and Moin, 1995). In other words,

$$\overline{\frac{\partial \phi}{\partial x}} = \frac{\partial \overline{\phi}}{\partial x} \tag{2.31}$$

holds only for a uniform stationary grid. In general, the uncertainties due to this operator exchange are neglected and their effects are assumed to be incorporated in the subgrid scale models.

Applying the filtering definition to the instantaneous Navier-Stokes equations for reactive flows with sprays gives the filtered balance equations as follows.

$$\frac{\partial \overline{\rho}}{\partial t} + \frac{\partial \left(\overline{\rho} \tilde{u}_j \right)}{\partial x_j} = \overline{\dot{\rho}^s} \tag{2.32}$$

$$\frac{\partial \overline{\rho} \tilde{u}_i}{\partial t} + \frac{\partial \left(\overline{\rho} \tilde{u}_i \tilde{u}_j \right)}{\partial x_j} = -\frac{\partial \overline{p}}{\partial x_i} + \frac{\partial}{\partial x_j}\left(\overline{\sigma}_{ij} - \overline{\rho} \tau_{ij} \right) + \overline{F_i^s} \tag{2.33}$$

$$\frac{\partial \left(\overline{\rho} \tilde{Y}_l \right)}{\partial t} + \frac{\partial \left(\overline{\rho} \tilde{u}_j \tilde{Y}_l \right)}{\partial x_j} = \frac{\partial}{\partial x_j}\left(\overline{D_{l,j} Y_l} - \overline{\rho} \tau_{u_j Y_l} \right) + \overline{\dot{\omega}_l^c} + \overline{\dot{\omega}_l^s} \delta_{l1} \quad \left(l = 1, N \right) \tag{2.34}$$

$$\begin{aligned} \frac{\partial \left(\overline{\rho} \tilde{h}_s \right)}{\partial t} + \frac{\partial \left(\overline{\rho} \tilde{u}_j \tilde{h}_s \right)}{\partial x_j} = {} & \frac{\partial \overline{p}}{\partial t} + \overline{u_j \frac{\partial p}{\partial x_j}} + \frac{\partial}{\partial x_j}\left(\overline{\lambda \frac{\partial T}{\partial x_j}} - \overline{\rho} \tau_{u_j h_s} \right) - \frac{\partial}{\partial x_j}\left(\overline{\rho \sum_{l=1}^{N} D_{l,j} Y_l h_{s,l}} \right) + \\ & \overline{\sigma_{ij} \frac{\partial u_i}{\partial x_j}} + \overline{\dot{Q}^c} + \overline{\dot{Q}^s} \end{aligned} \tag{2.35}$$

where $\overline{\sigma}_{ij}$ is the viscous stress term and is approximated as

$$\overline{\sigma}_{ij} \cong \tilde{\sigma}_{ij} = \mu \left(\frac{\partial \tilde{u}_i}{\partial x_j} + \frac{\partial \tilde{u}_j}{\partial x_i} \right) - \frac{2}{3} \mu \frac{\partial \tilde{u}_k}{\partial x_k} \delta_{ij} \,. \tag{2.36}$$

where μ is the effective viscosity. $\overline{F_i^s}$ is the filtered rate of momentum gain per unit volume due to spray and requires approximation. τ_{ij}, $\tau_{u_j Y_l}$ and $\tau_{u_j h_s}$ are the sub-grid scale stress tensor and sub-grid scale scalar fluxes, and are defined as follows

$$\tau_{ij} = \left(\widetilde{u_i u_j} - \tilde{u}_i \tilde{u}_j\right), \tag{2.37}$$

$$\tau_{u_j Y_l} = \left(\widetilde{u_j Y_l} - \tilde{u}_j \tilde{Y}_l\right), \tag{2.38}$$

and

$$\tau_{u_j h_s} = \left(\widetilde{u_j h_s} - \tilde{u}_j \tilde{h}_s\right). \tag{2.39}$$

The filtering operation gives rise to a number of sub-grid scale terms that are unclosed. One can simply ignore the sub-grid scale terms. For instance, one can ignore the sub-grid stress tensor but rely on appropriate numerics to introduce the additional dissipation to account for the unresolved field. But this approach is very difficult to analyze and therefore it is difficult to choose the appropriate numerical scheme (Ghosal, 1998). More appropriate approach is to directly model the sub-grid stress tensor in the momentum equation.

The filtered laminar diffusion fluxes for species and enthalpy may be either neglected or modeled through a simple gradient assumption and uniform diffusivity as

$$\overline{D_{l,j} Y_l} = -\overline{\rho D_{l,j} \frac{\partial Y_l}{\partial x_j}} \approx -\bar{\rho} \bar{D}_{l,j} \frac{\partial \tilde{Y}_l}{\partial x_j} \approx -\bar{\rho} \bar{D} \frac{\partial \tilde{Y}_l}{\partial x_j} \tag{2.40}$$

$$\overline{\lambda \frac{\partial T}{\partial x_j}} = \bar{\lambda} \frac{\partial \tilde{T}}{\partial x_j} \tag{2.41}$$

Other filtered non-linear terms also need models for the closures. For instance, unresolved Reynolds stresses $\left(\widetilde{u_i u_j} - \tilde{u}_i \tilde{u}_j\right)$ require subgrid scale turbulence models, and unresolved fluxes $\left(\widetilde{u_j Y_l} - \tilde{u}_j \tilde{Y}_l\right)$ and $\left(\widetilde{u_j h_s} - \tilde{u}_j \tilde{h}_s\right)$ require subgrid scale scalar models. The following will present various models that have been proposed to close these unresolved terms.

The sub-grid scale stress models can be classified into two major categories: constant coefficient models and dynamic models. The constant coefficient models generally require *a priori* specification of the model coefficient based on flow conditions and/or grid resolution. Commonly-used constant coefficients models include the Smagorinsky model (Smagorinsky, 1963), the scale similarity (Bardina et al., 1980; Bardina et al., 1983), the mixed model (Bardina et al., 1983), and the gradient model (Yeo, 1987). The dynamic models calculate the model coefficient based on the resolved field instead of using a constant value. Examples of this type include dynamic Smagorinsky model (Germano et al., 1991) and one-equation non-viscosity structure model (Pomraning and Rutland, 2002).

Constant coefficient models

The Smagorinsky model assumes that the anisotropic part of the sub-grid stress tensor is a scalar multiple of the filtered rate of strain tensor. The sub-grid scale stress tensor is then given by

$$\tau_{ij} - \frac{1}{3}\delta_{ij}\tau_{ll} = -\nu_t \tilde{S}_{ij} \tag{2.42}$$

where ν_t is the eddy viscosity and defined as

$$\nu_t = 2C_s\Delta^2\left|\tilde{S}\right|, \tag{2.43}$$

where Δ is the filter width, and $\tilde{S}_{ij}$ is the filtered rate of strain tensor

$$\tilde{S}_{ij} = \frac{1}{2}\left(\frac{\partial\tilde{u}_i}{\partial x_j} + \frac{\partial\tilde{u}_j}{\partial x_i}\right), \tag{2.44}$$

and $\left|\tilde{S}\right|$ is the magnitude of the filtered rate of strain tensor given by

$$\left|\tilde{S}\right| = \left(2\tilde{S}_{ij}\tilde{S}_{ij}\right)^{1/2}. \tag{2.45}$$

The parameter C_s is a user-specified coefficient that may depend on flow configuration and grid resolution. The Smagorinsky model has the following drawbacks. First, the assumption based on a molecular transport analogy cannot be justified. In fact, the real sub-grid stresses do not align with the filtered rate of strain and the correlations between them are low (Liu et al., 1994). Second, it is very difficult to specify an optimal value for the constant C_s for complex turbulent flows under different simulation conditions. Third, the model is purely dissipative, i.e., energy only flows from the resolved scale to the sub-grid scale. This characteristic may be helpful to numerical stability but neglect an important physics – reverse energy cascade or backscatter in which the energy is transferred from the sub-grid to the resolved scales (Piomelli et al., 1991). A good model should be able to account for the backscatter of energy.

Bardina (1980 and 1983) proposed the scale similarity model that addresses the backscatter of energy flows. The sub-grid scale stresses can be approximated from the resolved field (Yeo, 1987) based on the assumption that the sub-grid stresses are similar to the smallest

resolved stresses. The scale-similarity model is shown to correlates reasonably well with the sub-grid scale stresses. However, it does not ensure an overall positive transfer of energy to the sub-grid scales (Bardina et al., 1983). It is often coupled to the Smagorinsky model to derive a mixed model to address the insufficient energy dissipation of the scale similarity model (Bardina et al., 1983). As with the Smagorinsky model, the mixed model also needs to specify the model constant C_s.

The gradient model (Bedford and Yeo, 1993) relates the sub-grid stress tensor to the gradient of velocity. The gradient model correlates well with the actual sub-grid stress tensor due to the reason that this model is the first term in a series expansion for the exact sub-grid stress tensor (Pomraning, 2000). However, this model may result in a negative viscosity (Leonard, 1997) which can cause the model to become unstable.

Dynamic models

Since the model coefficient C_s in Eq. (2.43) usually depends on the flow and grid resolution, it will be more appropriate to directly calculate it instead of using a universal constant. As a result, dynamic subgrid models were developed based on the work by Germano et al. (1991). This dynamic approach is based on an algebraic identity between the subgrid scale stresses at two different filtered levels and the resolved turbulent stresses. Two filtering operations are performed to formulate a dynamic model. In addition to the 'grid' filtering operation, indicated by an overbar $\bar{}$, that leads to the filtered LES governing equations, a second

filtering called ‘test’ filtering (indicated by an arc $\widehat{\ }$) is performed on the resolved field. The ‘test’ filtering is defined in a similar manner as the ‘grid’ filtering operation as

$$\widehat{\phi}(\mathbf{x}) = \int_V G_T(\mathbf{x}-\mathbf{y})\phi(\mathbf{y})d\mathbf{y}\,, \tag{2.46}$$

where, for the ‘box’ filter, the function G_T becomes

$$G_T(\mathbf{x}) = \begin{cases} 1/\widehat{V} & |x_i| \le \widehat{\Delta}/2, i = 1,2,3 \\ 0 & \text{otherwise.} \end{cases} \tag{2.47}$$

$\widehat{V}$ is the ‘test’ filter volume. $\widehat{\Delta}$ is the ‘test’ level filter length which is usually twice the ‘grid’ level filter length Δ (Germano et al., 1991). Based on this definition, a stress tensor at the ‘test’ level can be defined by

$$T_{ij} = \left(\widehat{\widetilde{u_i u_j}} - \widehat{\tilde{u}}_i \widehat{\tilde{u}}_j\right) \tag{2.48}$$

Applying the ‘test’ filtering on the subgrid scale stress τ_{ij} gives

$$\widehat{\tau_{ij}} = \left(\widehat{\widetilde{u_i u_j}} - \widehat{\tilde{u}_i \tilde{u}_j}\right). \tag{2.49}$$

Further, the Leonard stress term L_{ij} is defined as

$$L_{ij} = \left(\widehat{\tilde{u}_i \tilde{u}_j} - \widehat{\tilde{u}}_i \widehat{\tilde{u}}_j\right). \tag{2.50}$$

The elements of L_{ij} can be calculated from the resolved velocity field. This is accomplished by invoking the ‘test’ filtering on the resolved field with a filter size typically twice the grid filter. Then, the ‘grid’ level stress tensor and the ‘test’ level stress tensor are related by the Germano identity (Germano et al., 1991)

$$L_{ij} = T_{ij} - \widehat{\tau_{ij}}\,. \tag{2.51}$$

This identity can be used to derive a dynamic Smagorinsky model that calculates the coefficient C_s in Eq. (2.43) as a function of time and space (Germano et al., 1991; Moin et al., 1991; Lilly, 1992). Assuming the same functional form to parametrize both T_{ij} and τ_{ij}, the 'test' level stress tensor can be approximated as

$$T_{ij} - \frac{1}{3}\delta_{ij}T_{ll} = -2C_s\widehat{\Delta}^2\left|\widehat{\tilde{S}}\right|\widehat{\tilde{S}}_{ij}\,. \tag{2.52}$$

Then, the Germano identity yields the following form

$$L_{ij} - \frac{1}{3}\delta_{ij}L_{kk} = -2C_sM_{ij}\,, \tag{2.53}$$

where

$$M_{ij} = \widehat{\Delta}^2\left|\widehat{\tilde{S}}\right|\widehat{\tilde{S}}_{ij} - \Delta^2\widehat{\left|\tilde{S}\right|\tilde{S}_{ij}}\,. \tag{2.54}$$

Germano et al. (1991) multiplies $\tilde{S}_{ij}$ on both sides of Eq. (2.53) to obtain a dynamic coefficient as

$$C_s = \frac{1}{2}\left(\frac{L_{ij}\tilde{S}_{ij}}{M_{mn}\tilde{S}_{mn}}\right). \tag{2.55}$$

Lilly (1992) applies a least square approach to obtain an improved coefficient given by

$$C_s = \frac{1}{2}\left(\frac{L_{ij}M_{ij}}{M_{mn}M_{mn}}\right). \tag{2.56}$$

The dynamic coefficients C_s may be positive or negative. A negative coefficient can lead to numerical instability that is usually addressed with additional averaging either in homogeneous spatial directions (Germano et al., 1991) or in time (Meneveau et al., 1996). For numerical stability, Piomelli and Liu (1995) arbitrarily set the negative coefficients to

zero thus eliminating all of the effects of 'backscatter'. The results were more accurate and more computationally efficient than a planar averaged model (Piomelli and Liu, 1995). For complex flows with no homogeneous directions, Meneveau et al. (1996) proposed a Lagrangian dynamic model that is derived by minimizing the dynamic Smagorinsky model error along flow pathlines in a Lagrangian frame of reference.

To address the numerical instability associated with the reverse energy flow from the sub-grid to the resolved scales, a transport equation for the sub-grid scale kinetic energy can be used to enforce a budget on the energy flow between the resolved and the sub-grid scales. The sub-grid kinetic energy k is defined as

$$k = \frac{1}{2}\left(\widetilde{u_i u_i} - \tilde{u}_i \tilde{u}_i\right) \tag{2.57}$$

This quantity cannot directly be calculated from the resolved velocity field and must be modeled. A transport equation for k can be derived by following the filtered momentum equation as (Yoshizawa and Horiuti, 1985; Menon et al., 1996; Warsi, 2006)

$$\frac{\partial k}{\partial t} + \frac{\partial \tilde{u}_j k}{\partial x_j} = \frac{\partial}{\partial x_j}\left(\frac{\nu_t}{\sigma_k}\frac{\partial k}{\partial x_j}\right) - \tau_{ij}\tilde{S}_{ij} - \varepsilon \tag{2.58}$$

where the terms on the right-hand side of Eq. (2.58) represent diffusion, production, and dissipation of the subgrid kinetic energy k, respectively. The sub-grid eddy viscosity ν_t and the sub-grid kinetic energy dissipation rate ε are modeled based on the sub-grid kinetic energy and the grid size as

$$\nu_t = C_k k^{1/2} \Delta \tag{2.59}$$

$$\varepsilon = C_\varepsilon \frac{k^{3/2}}{\Delta} \tag{2.60}$$

$$\Delta = V^{1/3} \tag{2.61}$$

where C_k, C_ε and σ_k are model constants with the values of 0.05, 1.0 and 1.0, respectively (Yoshizawa and Horiuti, 1985), Δ is the filter width, and V is the volume of a computational cell. This method is believed to be able to account for the non-equilibrium effect between production and dissipation at the sub-grid level to improve the model accuracy for high Reynolds number flows using relatively coarse grids (Menon et al., 1996). The reason is that sub-grid information and a kinetic energy budget are available for the formulation of sub-grid scale models, resulting in improved modeling of the effects of the sub-grid on the resolved scales. However, Menon et al. (1996) reported that the current model for the dissipation rate ε did not perform well. Thus, it is important to improve its modeling when the transport equation is solved for k.

Using this transport equation, a non-viscosity model, called the dynamic structure model (Pomraning and Rutland, 2002), was developed to estimate the stress tensor directly with

$$\tau_{ij} = \frac{2k}{L_{kk}} L_{ij} \tag{2.62}$$

where the Leonard stress tensor L_{ij} is rescaled by both its trace L_{kk} and the trace τ_{kk} of τ_{ij} $\left(\tau_{kk} \equiv 2k\right)$. This model was shown to provide a better scaling between the real stresses and the modeled terms than the viscosity-based models such as dynamic Smagorinsky models. The resolved and subgrid kinetic energies were shown to agree well with a direct numerical simulation of decaying isotropic turbulence (Pomraning and Rutland, 2002).

Meanwhile, similar modeling approach can be extended to scalar transport modeling (Chumakov and Rutland, 2004).

2.3 Spray Modeling

Engine sprays are typically composed of a very large number of droplets, and each of them has its own properties and is subject to very complex interactions with flows. Due to limited computational resources, it is not practical to account for each individual droplet in the simulation. Two major strategies that have been formulated to describe sprays in CFD simulations are Eulerian and Lagrangian formulations. The Eulerian formulation treats both sprays and the gas phase as continuous fields (Spalding, 1981; Drew, 1983). For poly-dispersed droplets, a number of separate fields can be used to represent different classes of droplet sizes. The spray formulations proposed by Sinnamon et al. (1980), Hallmann et al. (1995), Divis and Macek (2004), and Divis (2005) are examples of the Eulerian spray formulation. The Eulerian formulation works best in situations where the resolution scales are much larger than the average droplet spacing (Sirignano, 1986). Moreover, this formulation suffers from numerical diffusion of particle density, especially in the vicinity of the injector on coarse grids (Dukowicz, 1980; Loth, 2000).

Another strategy of spray modeling is the Lagrangian formulation based on a discrete-particle model introduced by Dukowicz (1980), also known as the stochastic particle model or discrete droplet model. The spray is represented by collective computational parcels with each parcel consisting of a number of droplets that are assumed to have identical properties

such as position, radius, density, velocity, and temperature. Each parcel is tracked in the Lagrangian frame of reference. The coupling between the spray and gas phases are achieved by exchanging source terms for mass, momentum, energy, and turbulence. Various sub-models are developed to account for the effects of droplet breakup, collision, turbulent dispersion, vaporization, and wall interaction. The properties of the representative parcels are randomly chosen from empirical or theoretical distribution functions. An adequate statistical representation of realistic sprays may be obtained when a sufficiently large number of parcels are used (Watkins, 1987). In addition, the Lagrangian formulation assumes large void fraction and thus is suitable for dilute sprays but has drawbacks in modeling dense sprays (Amsden et al., 1989). To address the dense spray near the injector exit, extended Lagrangian formulations (Stalsberg-Zarling et al., 2004; Gavaises and Tonini, 2006) or the Eulerian dense spray coupled with the Lagrangian dilute spray (Wang and Peters, 1997; Blokkeel et al., 2003; Lebas et al., 2005) is also developed. The Lagrangian approach is the most common spray description in engine simulation and is also used in this study. The following will review various spray sub-models used to simulate the engine spray processes.

Breakup models

As the spray enters the domain and interacts with the surrounding gas, it will experience the so-called atomization process in which the spray breaks up into small droplets. Atomization can be divided into two main processes: primary breakup and secondary breakup. The primary breakup occurs near the injector at high Weber numbers and is determined by not only the gas-liquid interaction but also the phenomena inside the nozzle such as cavitation

and turbulence. The secondary breakup occurs downstream of the spray and is mainly due to aerodynamic effects.

Primary breakup

The purpose of a primary breakup model is to determine the starting conditions of the drops that are created at the nozzle exit.

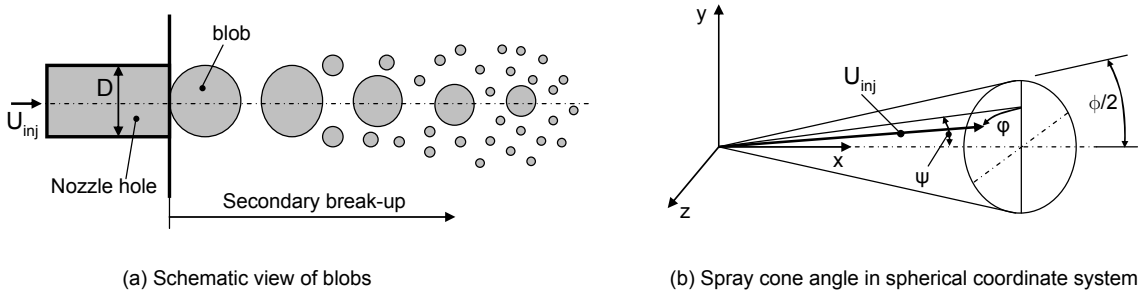

(a) Schematic view of blobs (b) Spray cone angle in spherical coordinate system

Figure 2.2. Blob-method of primary breakup.

Blob method

A simple but popular model for defining the starting conditions of a spray is the so-called "blob method" (Reitz, 1987; Reitz and Diwakar, 1987). This method assumes that the initial fuel jet breakup and drop breakup near the nozzle exit are indistinguishable processes, and that a detailed simulation can be replaced by the injection of big spherical drops with a uniform size. These drops are then subject to secondary breakup as shown in **Figure 2.2** (a). The size of the blobs is equal to the nozzle diameter. The number of drops injected per unit time is determined from the mass flow rate. The velocity components of the blobs are determined using the spray cone angle ϕ. The direction of the drop velocity inside the 3D

spray cone is randomly chosen by using two random numbers to predict the azimuthal angle φ and the polar angle ψ in the spherical coordinate system as shown in **Figure 2.2** (b).

In real engine sprays, particularly high-pressure diesel injection, cavitations often occur inside the nozzle affecting the actual flow area and injection velocity. The above blob method can be improved by calculating effective velocity and exit area resulting from cavitation (Kong et al., 1999; Kuensberg et al., 1999). Applying momentum and mass conservations between point 1 and point 2, as shown in **Figure 2.3**, gives the effective injection velocity by

$$u_{eff} = \frac{A_{hole}}{\dot{m}_{inj}}\left(p_{vap} - p_2\right) + \frac{\dot{m}_{inj}}{\rho_l A_{hole} C_c} \tag{2.63}$$

where p_{vap} is the vapor pressure and C_c is the coefficient determined according to (Nurick, 1976). The effective flow area A_{eff} and blob diameter D_{eff} are calculated as

$$A_{eff} = \frac{\dot{m}_{inj}}{u_{eff}\rho_l} \quad \text{and} \quad \mathrm{D}_{eff} = \left(\frac{4A_{eff}}{\pi}\right)^{1/2}. \tag{2.64}$$

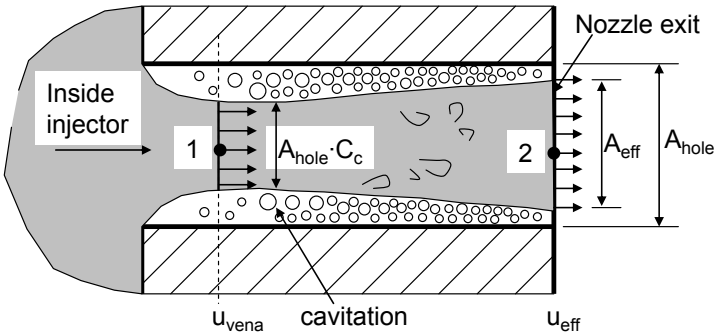

Figure 2.3. 1-D approximation of internal nozzle flow with cavitation.

The blob method is simple in terms of the conceptual understanding and code implementation. However, it does not provide detailed information about the influence of the phenomena inside the nozzle. This method also does not consider the promotion of primary breakup by turbulence and by implosions of cavitation bubbles inside the liquid jet.

Turbulence-induced breakup

This model is based on the phenomenological model developed by Huh and Gosman (1991) for predicting the primary spray angle of solid-cone diesel sprays. It assumes that the turbulence force within the liquid emerging from the nozzle can create initial surface perturbations that grow exponentially due to aerodynamic forces to form new droplets. The turbulent length scale determines the wavelength of the most unstable surface wave. The turbulent kinetic energy at the nozzle exit is determined based on mass, momentum, and energy balances. Huh and Gosman (1991) also assumed that the spray expands with a radial velocity. The spray angle can be determined by combining the radial velocity and axial velocity. The direction of the resulting velocity of the primary blob inside the spray cone is randomly chosen as described for the blob method. The model also assumes the injection of spherical blobs with the diameter equal to the nozzle hole diameter. The final velocity components are determined using the average turbulent kinetic energy and its dissipation rate at the nozzle exit.

The model determines the jet breakup based on a characteristic length scale L_A and time scale τ_A. The length scale L_A is assumed to be proportional to the turbulence length scale

and the time scale τ_A is a linear combination of the turbulence time scale and the wave growth time scale. The wave growth time scale is determined by applying the Kelvin-Helmholtz instability theory to an infinite plane. The turbulence length scale and time scale are determined from turbulence modeling. The breakup rate of the primary blob is proportional to the atomization length and time scale by

$$\frac{d}{dt}\left(d_{drop}\right) = k_1 \frac{L_A}{\tau_A} \tag{2.65}$$

where $k_1 = 0.05$ and d_{drop} is the diameter of the new drops. Both L_A and τ_A depend on time since the internal turbulence of parent drops decays with time as they travel downstream.

Cavitation-induced breakup

The caviation-induced model was developed by Arcoumanis et al. (1997) for solid-cone diesel sprays to model the primary breakup by accounting for cavitation, turbulence, and aerodynamic effects. This model assumes that the liquid jet emerging from the nozzle exit breaks up due to the collapsing cavitation bubbles. A 1-D submodel was used to estimate the nozzle exit data such as the effective hole area A_{eff}, injection velocity U_{inj}, and turbulent kinetic energy k and its dissipation rate in order to link the nozzle flow to the spray characteristics. The initial droplet diameter is assumed equal to the effective hole diameter. The first breakup of these blobs is modeled using the Kelvin-Helmholtz mechanism for aerodynamic-induced breakup, the model of Huh and Gosman (1991) for turbulence-induced breakup, and a phenomenological model for cavitation-induced breakup. This model also assumes that the cavitation bubbles either burst on the jet surface or collapse before reaching

it due to the smaller pressure compared to the ambient pressure. The minimum of the characteristic time scales between the two cases is used to determine breakup (Arcoumanis et al., 1997).

In the case of bubble collapse, the cavitation bubbles are lumped into a single big "effective" bubble having the same area as the total area of all the actual bubbles. The radius of this artificial bubble is used to estimate the collapse time τ_{coll} from the Rayleigh theory of bubble dynamics (Brennen, 1995). In the case of bubble bursting, the "effective" bubble is placed in the center of the liquid and then moves radially to the liquid surface with a turbulent velocity $u_{turb} = \sqrt{2k/3}$, resulting in a burst time τ_{burst}. The characteristic atomization time scale is taken as $\tau_A = \min\left(\tau_{coll}, \tau_{burst}\right)$. The atomization length scale is given by a correlation based on the nozzle hole size and cavitation bubble size. The breakup force acting on the jet surface at the time of collapsing or bursting of a cavitation bubble can then be estimated from dimensional analysis. The breakup force is used together with the surface tension force to determine the primary breakup. The exact size of the new droplets is sampled from a chosen distribution function.

Cavitation and turbulence-induced breakup

Nishimura and Assanis (2000) developed a cavitation and turbulence-induced primary breakup model for solid-cone diesel sprays that considers cavitation bubble collapse energy, turbulent kinetic energy, and aerodynamic forces. The model injects discrete cylindrical ligaments which have a diameter *D* and a volume equal to that of a sphere with the same

diameter as seen in **Figure 2.4**. The bubbles collapse and energy is released, resulting in an increase of turbulent kinetic energy k_{col} . Assuming isotropic turbulence, the turbulent velocity inside the liquid cylinder can be determined as

$$u_{turb} = \sqrt{\frac{2\left(k_{col} + k_{nozz}\right)}{3}} \tag{2.66}$$

where k_{nozz} is the turbulent kinetic energy at the nozzle exit. This turbulent velocity is used to determine the deformation force F_{turb} . The liquid cylinder breaks up if the sum of F_{turb} and the aerodynamic drag force no longer competes with the surface tension force.

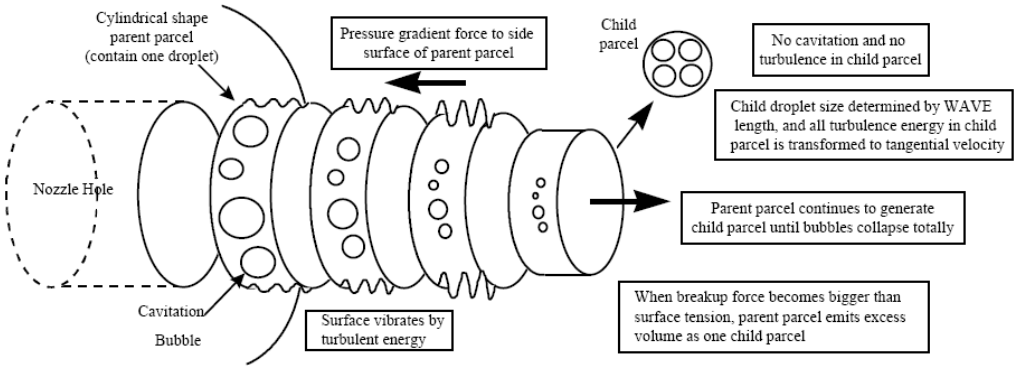

Figure 2.4. Primary breakup model of Nishimura and Assanis (2000).

Other authors also developed similar models for solid-cone diesel sprays based on different mechanisms. For instance, the model by Von Berg (2002) releases droplets from a coherent core. The sizes and velocity components of the droplets are calculated based on local turbulent scales and breakup rates on the core surface. Baumgarten et al. (2002) has developed a detailed cavitation and turbulence-induced model that is based on energy and

force balances and predicts the initial spray conditions needed to simulate further secondary breakup (Baumgarten, 2006).

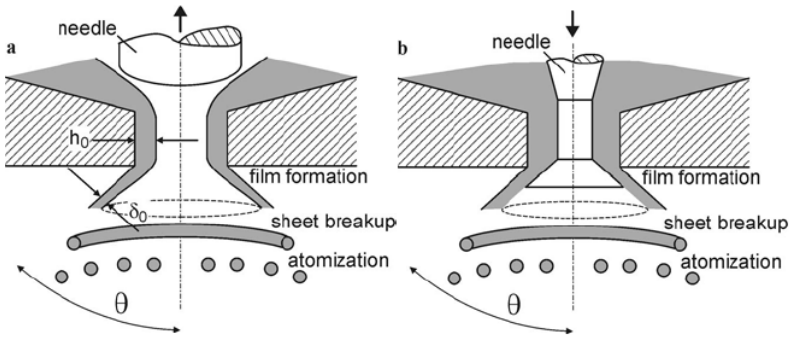

Figure 2.5. (a) Inwardly opening pressure-swirl atomizer, (b) outwardly opening pressure-swirl atomizer (Baumgarten, 2006).

Sheet atomization model for hollow-cone sprays

In direct-injection spark ignition engines, hollow-cone sprays are usually generated to maximize dispersion of the liquid phase at moderate injection pressures. Hollow-cone sprays are typically characterized by small droplet diameters, effective fuel-air mixing, reduced penetration, and thus high atomization efficiency. A model developed by Schmidt et al. (1999), usually referred to as the Linearized Instability Sheet Atomization (LISA), is often used to describe the primary breakup of hollow-cone sprays. In this model, a zero-dimensional approach is used to represent the internal injector flow and to determine the velocity at the nozzle hole exit. In the region near the exit, the transition from the injector flow to the fully developed spray is modeled by a three-step mechanism: film formation, sheet breakup, and disintegration into droplets (Senecal et al., 1999), as can be seen in **Figure 2.5**. More information about this model and the modeling of hollow-cone sprays can be found in (Schmidt et al., 1999; Senecal et al., 1999).

Secondary breakup

Secondary breakup is the breakup of the current existing droplets into smaller ones due to the aerodynamic forces that are induced by the relative velocity u_{rel} between the droplet and surrounding gas. Secondary breakup is believed to be controlled by a balance of two forces acting on the droplet that lead to opposite effects. The aerodynamic forces results in an unstable growth of waves on the droplet surface that leads to the disintegration. The surface tension force on the other hand tends to maintain the spherical droplet and counteracts the deformation force. The ratio of aerodynamic forces and surface tension force is a non-dimensional parameter, the gas phase Weber number We_g

$$We_g = \frac{\rho_g u_{rel}^2 d_d}{\sigma}. \tag{2.67}$$

Depending on the Weber number, different regimes and mechanisms of droplet breakup can exist. The following several paragraphs present models used to simulate the breakup process in sprays.

Phenomenological models

Arcoumanis et al. (1997) divided droplet breakup into seven different regimes based on the Weber number. Using phenomenological relationships the breakup times is estimated as

$$t_{br} = \tau_{break} \frac{d_d}{u_{rel}} \sqrt{\frac{\rho_l}{\rho_g}} \tag{2.68}$$

where the dimensionless breakup time τ_{break} is given in **Table 2.1**. If the breakup time is greater than the life time of the droplet, the breakup occurs. The product droplet sizes are

sampled from distribution functions. The Sauter mean diameter (SMD) of the droplets is estimated using phenomenological relations based on the Weber number, drop diameter, drop viscosity, relative velocity, and densities of the drop and gas. In the case of stripping breakup, small product droplets are stripped from the parent droplets, and their mass is subtracted from their parent drops.

Table 2.1. Breakup regimes and breakup times of droplets (Arcoumanis et al., 1997).

Breakup regime	Breakup time τ_{break}	Weber number
Vibrational	$\tau_{break} = 0.25\pi\left[\frac{\sigma}{\rho_l d^3} - 6.25\frac{\mu_l}{\rho_l d^2}\right]^{-0.5}$	$We_g \le 12$
Bag	$\tau_{break} = 6\left(We_g - 12\right)^{-0.25}$	$12 < We_g \le 18$
Bag-and-steamen	$\tau_{break} = 2.45\left(We_g - 12\right)^{0.25}$	$18 < We_g \le 45$
Chaotic	$\tau_{break} = 14.1\left(We_g - 12\right)^{-0.25}$	$45 < We_g \le 100$
Sheet stripping	$\tau_{break} = 14.1\left(We_g - 12\right)^{-0.25}$	$100 < We_g \le 350$
Wave crest stripping	$\tau_{break} = 0.766\left(We_g - 12\right)^{0.25}$	$350 < We_g \le 1000$
Catastrophic	$\tau_{break} = 0.766\left(We_g - 12\right)^{0.25}$	$1000 < We_g \le 2760$
	5.5	$2760 < We_g$

Taylor Analogy Breakup (TAB) Model

The TAB model developed by O'Rourke and Amsden (1987) is based on an analogy between an oscillating and distorting drop that penetrates through surrounding gas with a relative velocity u_{rel} and a forced oscillating spring-mass system. The aerodynamic drag acts as the external force, the surface tension as the restoring force, the liquid viscosity as the damping

force. Using this analogy, the equation for the acceleration of the droplet distortion parameter y is

$$\ddot{y} + C_d \frac{\mu_l}{\rho_l r^2} \dot{y} + C_k \frac{\sigma}{\rho_l r^3} y = \frac{C_F}{C_b} \frac{\rho_g u_{rel}^2}{\rho_l r^2} \tag{2.69}$$

where y is the normalized displacement of the droplet's equator from its equilibrium position. C_d, C_k, C_b, and C_F are model constants. r is the droplet radius in spherical shape. ρ_g and ρ_l are the gas and liquid densities, and σ is the surface tension. The size of the product droplets is estimated using an energy balance. For each breakup event, the radius of the product drops is chosen randomly from a χ-squared distribution. The number of the product drops can then be determined using mass conservation.

The TAB model is one of the original drop breakup models and is often used to predict gasoline drop breakup. This model can underpredict the droplet size of diesel sprays (Liu and Reitz, 1993; Tanner, 1997) and underestimate the spray penetration (Park et al., 2002). An enhanced TAB model (ETAB) was proposed by Tanner (1997) that accounts for the initial oscillation in addition to the modified product drop sizes. The deformation velocity is also modified to increase the lifetime of the blobs and to allow a more realistic representation of the dense spray near the nozzle exit (Baumgarten, 2006). Ibrahim (1993) also extended the TAB model by considering the extensional flow that causes the drop to become an oblate spheroid. A different breakup criterion was formulated and the product droplet size was estimated using the same method as in the TAB model.

Kelvin Helmholtz (KH) Breakup Model

The KH model is based on a first order linear analysis of a Kelvin-Helmholtz instability growing on the surface of a cylindrical liquid jet that is penetrating into a stationary gas. These surface waves grow due to the aerodynamic force resulting from the relative velocity between the liquid and gas as shown in **Figure 2.6**. It is assumed that the wave with the highest growth rate is the most unstable surface wave and will cause breakup to form new droplets. The growth rate Ω of this wave can be determined from the numerical solution to a dispersion function of a perturbation (Reitz and Bracco, 1986) according to

$$\Omega\left[\frac{\rho_l r_0^3}{\sigma}\right]^{0.5} = 2\left(\frac{4}{3\pi}\right)^6\left(\frac{1}{y_{break}}\right)^5 = \frac{0.34+0.38\ We_g^{1.5}}{(1+Z)(1+1.4\ T^{0.6})}, \tag{2.70}$$

and the corresponding wavelength Λ,

$$\frac{\Lambda}{r_0} = 9.02\frac{(1+0.45\ Z^{0.5})(1+0.4\ T^{0.7})}{(1+0.87\ We_g^{1.67})^{0.6}}, \tag{2.71}$$

where *We*, *Z* and *T* are the Weber, Ohnesorg and Taylor number, respectively, and are defined as

$$We_g = \frac{\rho_g r_0 u_{rel}^2}{\sigma}, Z = \frac{\mu_l}{\sqrt{\rho_l r_0 \sigma}}, T = Z\sqrt{We_g}\ . \tag{2.72}$$

r_0 is the radius of the undisturbed jet. The radius of the new droplets is assumed to be proportional to the wavelength Λ as

$$r_{new} = B_0\Lambda\ , \tag{2.73}$$

where $B_0 = 0.61$ is a constant. In contrast to the complete breakup of the parent drop in the TAB model, the parent drop continuously loses mass while penetrating into the gas. The

radius shrinks at a rate that depends on the difference between the current droplet radius r and the child droplet radius r_{new} and on the characteristic time

$$\frac{dr}{dt} = -\frac{r - r_{new}}{\tau_{bu}}, \qquad \tau_{bu} = 3.788\, B_1 \frac{r}{\Lambda\Omega}. \tag{2.74}$$

where τ_{bu} is the breakup time scale and B_1 is an adjustable constant to account for the influence of the internal nozzle flow on the spray breakup.

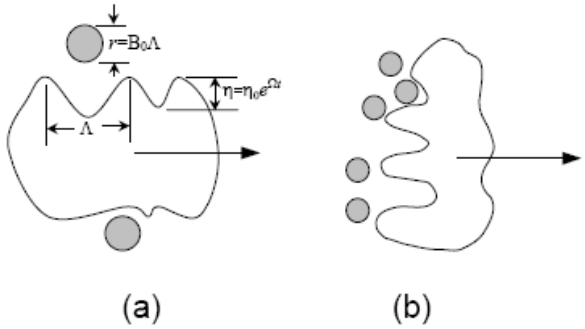

Figure 2.6. Schematic illustration of drop breakup mechanisms (a) KH-type; (b) RT-type (Kong et al., 1999).

The KH model creates a group of drops that demonstrate a bimodal distribution of drop sizes with a small number of big parent drops and an increasing number of small child droplets. Although stripping breakup is one of the most important breakup mechanisms for high-pressure injection, experiments have shown (Hwang et al., 1996) that the sudden disintegration of a complete drop into droplets with diameter much bigger than the KH-child droplets is also important. For this reason, the KH model is usually combined with the Rayleigh-Taylor model that will be described next.

Rayleigh Taylor (RT) Breakup Model

The RT model is based on the work of Taylor, as cited by Batchelor (1963), about the instability of the interface between two fluids of different densities with acceleration being normal to this interface. For drop and gas moving with a relative velocity u_{rel}, the drop deceleration due to drag forces can be viewed as an acceleration of the drop in the opposite direction (airflow direction). The Taylor's theory indicates that the interface can be unstable if the acceleration is directed into the gas. Thus, unstable waves can grow on the back side of the drop, as seen in **Figure 2.6** (b). From the aerodynamic drag force, the acceleration of the drop can be simplified to

$$a = \frac{3}{8} c_D \frac{\rho_g u_{rel}^2}{\rho_l r}. \tag{2.75}$$

Assuming linearized disturbance growth rates and negligible liquid viscosity, the growth rate Ω and the corresponding wavelength Λ of the fastest growing wave are:

$$\Omega = \sqrt{\frac{2a}{3}} \left[\frac{a\rho_l}{3\sigma} \right]^{1/4}, \tag{2.76}$$

and

$$\Lambda = C_3 \; 2\pi \sqrt{\frac{3\sigma}{a\rho_l}}. \tag{2.77}$$

The breakup occurs only if $\Lambda < d_{drop}$. The breakup time $t_{bu} = \Omega^{-1}$ is the reciprocal of the frequency of the fastest growing wave. At $t = t_{bu}$ the drop breaks up completely into smaller drops with the radius $d_{new} = \Lambda$ and the number of new drops is obtained based on the mass conservation (Patterson and Reitz, 1998). C3 is an adjustable constant to control the

effective wavelength by accounting for unknown effects such as the initial disturbance at the nozzle exit.

Drag-deceleration (RT model) and shear flow (KH model) induced instability phenomena have been observed simultaneously in the droplet breakup process (Hwang et al., 1996). Hence, the RT model is always used in combination with a second breakup model, usually the KH model. In addition, combined models have been widely used because no single breakup model can describe all relevant classes of breakup processes and regimes accurately. The combined KH-RT breakup model uses the KH model near the nozzle exit and uses the RT model beyond the breakup length L_b to avoid a too fast reduction of the drop size near the nozzle exit (Kong et al., 1999), as shown in **Figure 2.7**.

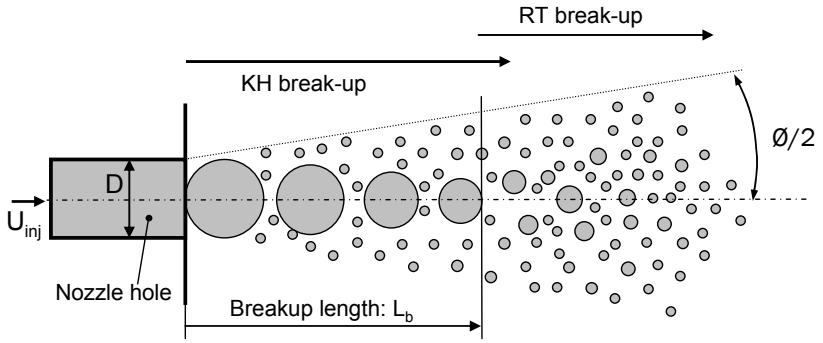

Figure 2.7. Combined blob-KH/RT model (Kong et al., 1999).

Collision and coalescence

Droplet collision plays an important role in influencing spray dynamics, particularly in the dense spray region where the probability of collision is high. The result of a collision event depends on the impact energy, the ratio of droplet sizes, and ambient conditions including

gas density, gas viscosity, and the fuel-air ratio (Baumgarten, 2006). Collision can result in coalescence, pure reflection, or breakup. As a result of collision, the droplet velocity, trajectory, and size will be changed.

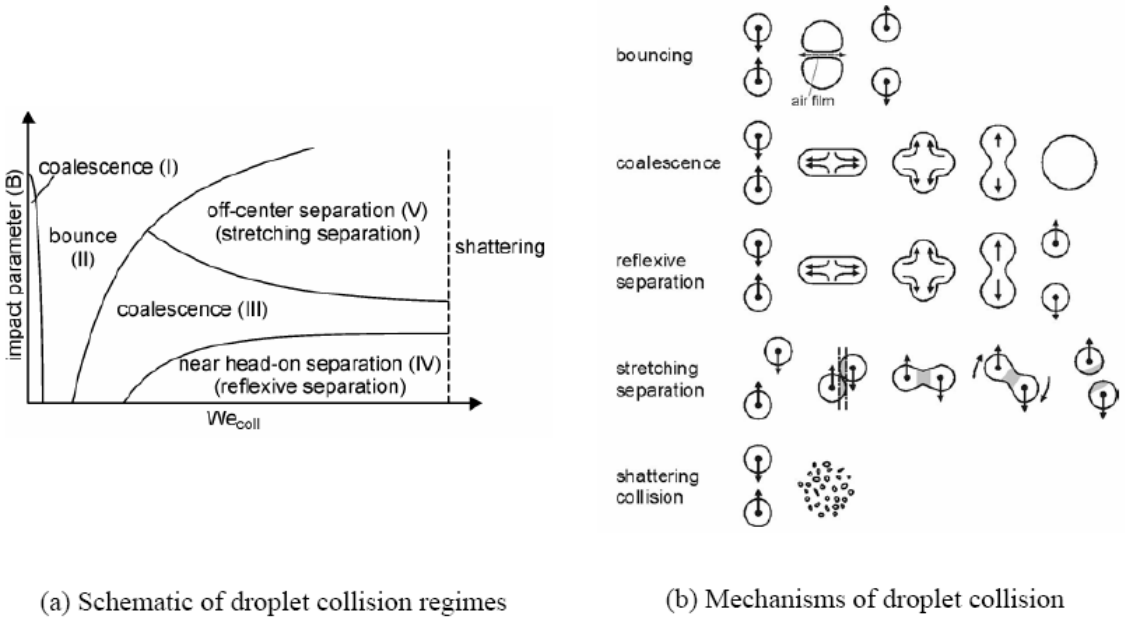

(a) Schematic of droplet collision regimes (b) Mechanisms of droplet collision

Figure 2.8. Regimes and mechanisms of droplet collision (Baumgarten, 2006).

The collision phenomenon can be characterized by using four dimensionless parameters: the Reynolds number, the Weber number, the drop diameter ratio, and the impact parameter. The possible outcomes of a collision event include bouncing, coalescence, reflective separation, stretching separation, and shattering, as shown in **Figure 2.8**. Most of the practical collision models do not consider all of the above phenomena due in part to the fact that it is impossible to directly evaluate a collision model by comparison with available experimental data. The standard collision model used in most spray simulations is the model by O'Rourke and Bracco (1980), which considers only two outcomes: coalescence and

stretching separation (grazing collision). This model follows the approach of Brazier-Smith et at. (1972) and uses an energy balance to predict whether the two colliding drops separate again after coalescence to re-form the original drops or combine to form a larger drop. Tennison et al. (1998) enhanced this model by taking into account reflective separation. Georjon and Reitz (1999) proposed a drop-shattering collision model by extending the stretching separation regime.

The O'Rourke model is often implemented by using the statistical approach for enhanced efficiency. The implementation of the O'Rourke model using the statistical approach is inherently grid dependent based on three factors. First, droplets can only collide within the same computational cells. Second, the collision frequency depends on the size of grid cells. Third, the implementation uses the magnitude of the relative velocities without considering the orientation of the velocities. These factors have been shown to cause several artifacts that were observed in engine spray simulations (Schmidt and Rutland, 2000; Hieber, 2001; Nordin, 2001; Are et al., 2005). Advanced numerical schemes such as adaptive mesh refinement can be used to alleviate such grid dependence as will be discussed later.

Vaporization models

The vaporization of liquid fuel influences ignition, combustion, and formation of pollutants. The vaporization process involves heat transfer and mass transfer that will affect temperature, velocity, and vapor concentration in the gas phase. The standard modeling approach is to use a single component vaporization model, e.g., tetradecane for diesel fuel and iso-octane for gasoline. The rate of the drop temperature change is described as

$$\frac{4\pi r^3}{3}\rho_d c_l \frac{dT_d}{dt} = 4\pi r^2 Q_d + \rho_d 4\pi r^2 \frac{dr}{dt} L\left(T_d\right) \tag{2.78}$$

where c_l is the specific heat of the liquid, r is the radius of the drop, $L\left(T_d\right)$ is the latent heat of vaporization, and Q_d is the rate of heat transfer to drop surface per unit area by conduction and is obtained by using the Ranz-Marshall correlation (Faeth, 1977)

$$Q_d = K_g\left(\hat{T}\right)\frac{T_g - T_d}{2r} Nu_d, K_g\left(\hat{T}\right) = \frac{K_1 \hat{T}^{3/2}}{\hat{T} + K_2}. \tag{2.79}$$

The film temperature $\hat{T}$, the thermal conductivity $K_g\left(\hat{T}\right)$, and the Nusselt number Nu_d are related to other fundamental properties and the Spalding's mass transfer number of the drop (Faeth, 1977). K_1 and K_2 are constants.

More sophisticated vaporization models consider the effect of multicomponents in the fuel. These models include "discrete component" and "continuous component" approaches (Sazhin, 2006). The first approach uses distinct full components to compose the drop properties (Torres et al., 2003). The second approach uses a continuous thermodynamics approach to describe the multicomponent effects of fuels (Tamin and Hallett, 1995). Multicomponent vaporization models have the potential to describe the vaporization process more accurately under a low temperature environment in which light components vaporize earlier and influence ignition more significantly (Zhang and Kong, 2009).

Turbulence dispersion models

Turbulence affects not only the gas phase flow but also the motion of droplets. A portion of turbulent kinetic energy is used to disperse the droplets and the droplet-turbulence interactions need be considered in spray modeling. The behavior of droplets in the flow field can be characterized by a non-dimensional parameter called the Stokes number St

$$St = \frac{\tau_r}{\tau_e} \tag{2.80}$$

where τ_r and τ_e are the aerodynamic response time and the eddy life time, respectively. The aerodynamic response time τ_r indicates the responsiveness of a droplet to a change in gas velocity and the eddy life time τ_e is an eddy breakup time equal to k/ε. For small Stokes number, the droplets react to the flow very quickly and will follow the flow field very well. For large Stokes number, the droplets react to the flow change slowly and the droplets can barely follow the flow field.

In the Lagrangian-Eulerian approach, a droplet generally evolves on the aerodynamic response time

$$\frac{d\mathbf{u}_\mathbf{d}}{dt} = \frac{\mathbf{u}_\mathbf{g} - \mathbf{u}_\mathbf{d}}{\tau_r} \tag{2.81}$$

where $\mathbf{u}_\mathbf{g}$ is the instantaneous gas velocity. A droplet interacts with a wide range of turbulence length and time scales. Pai and Subramaniam (2006) found that a model evolving droplets over the response time using a linear drag law will predict an anomalous increase in the liquid phase turbulent kinetic energy for decaying turbulent flow laden with droplets. Pai and Subramaniam (2006) proposed that the fluctuating droplet velocity relaxes to the local

modeled fluctuating gas phase velocity on a multiscale interaction time scale. Numerical tests on a zero-gravity, constant-density, decaying homogeneous turbulent flow laden with sub-Kolmogorov-size droplets show that the improved model predicts correct trends of the turbulent kinetic energy for both phases.

Wall interaction models

Spray-wall interactions can influence mixture distribution, combustion, and emissions. The possible outcomes include stick, rebound with or without breakup, wall jet, spread, splashing, and wall film formation (Kong, 2007). Many factors can influence the outcomes of the spray-wall interactions, such as the incident drop velocity, incidence angle, liquid density, surface tension, and wall temperature and wettability. These factors can be combined to form several important dimensionless parameters: Weber, Reynolds, and Ohnesorge numbers. The Weber number is the most important parameter and its definition for the drop impingement represents the ratio of the droplet's normal inertia to its surface tension as

$$We_l = \frac{\rho_l u_n^2 d}{\sigma} \tag{2.82}$$

where u_n is the drop's velocity component normal to the surface, ρ_l is the liquid density, σ is the surface tension, and d is the drop diameter. Different impingement criteria can be formulated based on the drop Weber number.

Naber and Reitz (1988) developed an impingement model that considers the stick, rebound and spread regimes based on Weber number. This model was improved later by correcting the normal drop velocity in the rebound regime. Bai and Gosman (1995) developed a model

that considers the splash regime. This model also combines the stick and spread regimes as adhesion regime for a dry wall. Other detailed wall-impingement models have been developed by O'Rourke and Amsden (2000), Lee and Ryou (2001), and Stanton and Rutland (1996). In these models, the splash regime is treated differently than that by Bai and Gosman (1995).

2.4 Combustion Modeling

The objective of the combustion modeling is to close the mean reaction rate $\overline{\dot{\omega}_l}$ in Eq. (2.10) in the RANS approach or the filtered reaction rate $\overline{\dot{\omega}_l^c}$ in (2.34) in the LES approach. Since the reaction rate is usually highly nonlinear, the mean or filtered reaction rate cannot be simply expressed as a function of the mean quantities of the flow field and the species. Thus, appropriate models need to be developed to address unclosed terms resulting from RANS averaging or LES filtering. The model development is strongly dependent on the relative magnitude of characteristic chemical time scales τ_c and turbulent time scales τ_t since the interactions of chemistry and turbulence occur in a wide range of time scales in an engine combustion. The relative magnitude of the time scales can be divided into cases: slow chemistry (chemical time scales much larger than turbulent time scales), finite rate chemistry, and fast chemistry (chemical time scales much smaller than Kolmogorov time scale τ_η) (Williams, 1985; Peters, 2000; Pope, 2000; Poinsot and Veynante, 2001; Fox, 2003). A dimensionless parameter called the Damkohler number $D_a = \tau_t / \tau_c$ can be used to represent

the above relations. The Damkohler number along with other dimensionless parameters such as Reynolds number can be used to define different combustion regimes.

Combustion requires that fuel and air be mixed at the molecular level. Depending on how well the fuel-air mixture is prepared before the occurrence of combustion, engine combustions can be divided into three categories: premixed combustion (i.e., conventional gasoline engines), non-premixed combustion (i.e., conventional diesel engines), and partially premixed combustion.

Closure models in RANS approach

For premixed flames, the simplest approach is to directly use the mean local values of density and species to represent the mean Arrhenius reaction rates by neglecting the turbulence effects. The approach is relevant only in the case of slow chemistry. If turbulence plays a rate-limiting role, then the so-called eddy breakup model (Spalding, 1977; Peters, 2000) can be used to represent the mean reaction rate as

$$\overline{\dot{\omega}_\theta} = C_e \overline{\rho} \frac{\varepsilon}{k} \tilde{\theta}\left(1-\tilde{\theta}\right) \tag{2.83}$$

where θ is a progress variable ($\theta = 0$: fresh gases and $\theta = 1$: burnt gases) and $\tilde{\theta}$ is its mean and solved from a transport equation, k and ε are the turbulent kinetic energy and its dissipation rate, and C_e is a constant. This model is simple but useful in many applications. However, it does not include effects of chemical kinetics and it tends to overestimate the reaction rate, especially in highly strained regions. There are also other more complicated

models that require solving a number of transport equations such as the probability density function (PDF) models (Pope, 2000; Fox, 2003).

For non-premixed flames, mixing of fuel and air is important and generally limits the chemical reactions. Non-premixed flames also do not exhibit well-defined characteristic scales. These factors make it more difficult to define combustion regimes (Poinsot and Veynante, 2001; Fox, 2003). Since the overall reaction rate is limited by both the chemistry and the molecular diffusion of species toward the flame front, the model needs to consider both chemistry and turbulent effects. Two popular models of this type are the flamelet model and the eddy dissipation concept model. In the flamelet model, the instantaneous reaction rates for species can be expressed as a function of the scalar dissipation rate χ and the mixture fraction z (Peters, 1984; Peters, 2000; Kong et al., 2007b) only

$$\dot{\omega}_l = -\frac{1}{2}\rho\chi\frac{\partial^2 Y_l}{\partial z^2} \tag{2.84}$$

where Y_l is the mass fraction for species l. Flow influence is completely determined by the scalar dissipation rate χ, which is defined as $\chi = 2D\nabla C \bullet \nabla C$ where C is a conserved scalar and D is the scalar diffusivity. Note that the scalar dissipation rate χ is different than the turbulent dissipation rate ε that is a turbulent flow property and equal to the energy transfer rate from the large eddies to the smaller eddies. χ is an important quantity in a turbulent non-premixed combustion to describe a mixing rate. Chemical effects are incorporated through the flame structure in mixture fraction space. The flamelet model (Peters, 2000) expresses the mean reaction rate using a PDF formulation according to

$$\overline{\dot{\omega}_l} = \int_0^1 \int_0^\infty \dot{\omega}_l \left(z, \chi_{st}\right) f\left(z\right) f\left(\chi_{st}\right) dz d\chi_{st} . \tag{2.85}$$

$f\left(z\right)$ presumes to be β-functions and χ_{st} is often assumed to follow a log-normal distribution. The laminar reaction rate $\dot{\omega}_l \left(z, \chi_{st}\right)$ needs to be calculated and stored in a library before a combustion simulation is performed.

The eddy dissipation concept model (Magnussen and Hjertager, 1977; Magnussen, 1981) is an extension of the eddy breakup model to non-premixed combustion. The mean fuel burning rate is estimated from the following expression

$$\overline{\dot{\omega}_F} \approx C_m \overline{\rho} \frac{\varepsilon}{k} \min\left(\tilde{Y}_F, \frac{\tilde{Y}_O}{s}, \beta \frac{\tilde{Y}_P}{\left(1+s\right)} \right). \tag{2.86}$$

C_m and β are model constants. $\tilde{Y}_F$, $\tilde{Y}_O$, and $\tilde{Y}_P$ are the mean mass fractions of fuel, oxidizer, and products, respectively. s is the reaction coefficient for the fuel. The eddy dissipation concept was further used to formulate a species conversion rate based on the characteristic time in the reacting flow (Kong et al., 1995). The characteristic-time model considers the influence of both laminar chemistry and turbulent mixing in determining the overall reaction rate.

Closure models in LES approach

For premixed flames, the LES approach encounters a difficulty in resolving a very thin flame front which is entirely on the subgrid scale (Pitsch, 2006). This was addressed by using an artificially thickened flame (Colin et al., 2000), or a flame front tracking technique, i.e., level-set method (G-equation) (Pitsch, 2005), or filtering with a Gaussian filter larger than

the mesh size (Boger et al., 1998). A simple approach is to extend RANS models to LES. For instance, the eddy breakup model can be rewritten as

$$\overline{\dot{\omega}_\theta} = C_{Le}\overline{\rho}\frac{1}{\tau_{t,SGS}}\tilde{\theta}\left(1-\tilde{\theta}\right) \tag{2.87}$$

where C_{Le} is a constant, θ is a progress variable and $\tilde{\theta}$ is its resolved mean, and $\tau_{t,SGS}$ is a subgrid turbulent time scale

$$\tau_{t,SGS} \approx \frac{\Delta}{k_{SGS}^{1/2}} \tag{2.88}$$

where Δ is the filter size and k_{SGS} is the subgrid turbulent kinetic energy.

For non-premixed flames, the PDF concept can be extended from RANS to LES for both infinitely fast chemistry and finite rate chemistry. In the infinitely fast chemistry, the reaction rates are governed by the mixing. The filtered reaction rates depend only on the mixture fraction z

$$\overline{\dot{\omega}_l}\left(\mathbf{x},t\right) = \int_0^1 \dot{\omega}_l\left(z\right) f\left(z,\mathbf{x},t\right) dz \tag{2.89}$$

where $f\left(z,\mathbf{x},t\right)$ is the subgrid scale PDF that may be either presumed or obtained by solving a transport equation. In the finite rate chemistry, the species mass fraction depends on both the mixture fraction and its scalar dissipation rate (Cook and Riley, 1998; Pitsch, 2006).

2.5 Adaptive Grid Methods

Adaptive mesh refinement (AMR) was initially developed to improve solution accuracy when solving partial differential equations (Berger, 1982; Berger and Oliger, 1984). AMR

has then been extended for use in solving various types of equations for a wide variety of engineering applications (Bell et al., 1994b; Pember et al., 1995; Berger and LeVeque, 1998; Jasak and Gosman, 2000b; Wang and Chen, 2002; Anderson et al., 2004). The purpose of using AMR was to simulate complex processes more accurately while controlling computational cost. In general, there are three major adaptive methods: h-refinement, p-refinement, and r-refinement (Jasak and Gosman, 2000a). The h-refinement adds grid points in regions of high spatial activity and is popular in finite volume solvers due to its simplicity without the need for grid redistribution. The p-refinement adjusts the local order of approximation in appropriate regions of the domain and is popular in finite element method. The r-refinement method does not change total grid points but redistributes the grid to minimize approximation error.

AMR was also applied to improve engine spray simulation. Lippert et al. (2005) incorporated local refinement algorithms into an in-house solver using the isotropic cell-splitting approach for hexahedral elements. The criterion for controlling refinement and coarsening was the sum of fuel vapor mass and droplet mass in each cell, normalized by the total injected mass. A global error control method was also formulated to determine whether the solution was good enough. To further alleviate the grid dependence of spray modeling, an improved coupling of both the gas-to-liquid and liquid-to-gas parameters was also performed. Numerical tests showed the effectiveness of AMR coupled with the improved phase coupling technique in removing grid artifacts associated with spray modeling.

Bauman (2001) implemented a spray model into a CFD code that employed AMR. The goal was to address the problem of insufficient solution resolution when a mesh with fixed cell size was used in order to achieve reasonable run times in high-pressure spray simulations. Tonini (2008) employed an adaptive local grid refinement methodology combined with a calculation procedure that distributed the mass, momentum and energy exchange between the liquid and gas phases. The adaptation could be performed on various unstructured meshes such as tetrahedron, hexahedron, pyramid, and prism. The grid refinement of up to three levels was tested. The numerical results showed that the proposed methodology offered significant improvements in dense spray simulation compared to the standard Lagrangian method.

2.6 Parallel Computing

Multidimensional engine modeling can be computationally intensive, especially when detailed combustion models or advanced turbulence models are used. Serial computation can be impractical for engineering application. High performance parallel computing using multiple processors can greatly reduce clock time and benefit product development for industry. Rapid advances of computer technologies and development in parallel algorithms have enabled researchers to use massive parallel computation for complex problems.

There are two major parallel programming algorithms: shared-memory method and message-passing method. The shared-memory method treats the total memory of the computer as equally accessible to each processor but the access may be coupled by different bandwidth

and latency mechanism. For optimal performance, parallel algorithms must consider non-uniform memory access. Programming in shared memory can be done in a number of ways, some based on threads, others on processes. The thread-based method has some advantages. Synchronization and context switches among threads are faster than among processes. Creating additional thread of execution is usually faster than creating another process. Many thread-based libraries are available among which OpenMP is the most popular. In the message-passing method, each processor has its own memory which is accessible only to that processor. Processors can interact only by passing messages. The most common form of this method is the Message Passing Interface (MPI). MPI provides a mature, capable, and efficient programming method for parallel computation. It is highly portable and also the most common method for parallel computing.

There are numerous applications of parallel computation for engine simulation. Yasar et al. (1995) developed a parallel version of KIVA-3 coupled with the use of a block-wise decomposition scheme to ensure an efficient load balancing and low communication/computation ratio. Filippone et al. (2002) parallelized KIVA-3 using BLAS library based on the MPI method. Aytekin (1999) implemented KIVA-3 on a distributed-memory machine based on one-dimensional domain decomposition using the MPI library for large eddy simulation. Zolver et al. (2003) developed an OpenMP-based parallel solver in the code KIFP for diesel engine simulation using unstructured meshes and reached a speed-up of three on four processors. The most recent advance in the KIVA code development is the parallel version of KIVA-4 using the MPI library (Torres and Trujillo, 2006). In this parallel version, hydrodynamic calculations, spray, combustion, and piston movement are all

parallelized. Domain decomposition of an arbitrary unstructured mesh can be performed automatically based on a graphic method by using a package called METIS (Karypis and Kumar, 1998a). Dynamic domain re-partitioning during the course of a computation was also implemented to further enhance parallel performance by addressing the dynamic change of active cells due to the port deactivation and piston movement.

2.7 KIVA Code

Among various engine simulation codes, the KIVA code is the most widely used code in the research community. KIVA is used as a base CFD code based on which various physical and chemistry models are developed. The first version, KIVA, was released in 1985 which was capable of computing transient compressible flows with fuel sprays and combustion in relatively simple geometries (Amsden et al., 1985a; Amsden et al., 1985b). A later improvement is KIVA-II (Amsden et al., 1989) that included implicit temporal differencing, more accurate advection with an improved upwinding scheme, and a $k-\varepsilon$ turbulence model. KIVA-3 (Amsden, 1993) added the capability of using a block-structured mesh in which multiple blocks of cells could be patched together to construct a more complex engine mesh. The code was enhanced by an improved snapping procedure to remove or add layers of cells during piston movement. KIVA-3V (Amsden, 1997) added algorithms to simulate moving valves and also included a liquid wall film model. Various advanced sub-models for sprays, turbulence, and combustion were developed and added to this version for engine analysis and design by a significant number of institutions.

KIVA-4 (Torres and Trujillo, 2006), the latest version of the KIVA code, represents a fundamental change in the numerics in order to accommodate unstructured meshes. The unstructured meshes can include various cell types such as hexahedra, tetrahedral, prisms, and pyramids. Another important improvement is that KIVA-4 was parallelized using MPI. Additionally, a collocated version of KIVA-4 was also available for further development of advanced numerical schemes such as local mesh refinement.

This study made use of different versions of the KIVA code to develop advanced models and numerical algorithms. Because KIVA-3V is well established and validated, this version was used as the base code for the development of an LES turbulence model. On the other hand, due to its flexibility in handling unstructured mesh, the collocated KIVA-4 was used to develop the adaptive mesh refinement algorithms for more efficient and accurate spray simulation.

3 DIESEL ENGINE COMBUSTION MODELING

3.1 Introduction

This chapter describes the major models that were implemented into KIVA-3V (Amsden, 1997) for diesel spray combustion simulation in the context of LES. The previously developed combustion model based on detailed chemical kinetics (Kong et al., 2007b) will also be described for the completeness of this thesis. This chapter will be arranged as follows. First, subgrid models will be presented for the modeling of gas-liquid two-phase flows in the context of LES, followed by the description of combustion and emissions models. Then, model validations will be performed in two cylindrical chambers by comparing simulation results against experimental data. Finally, the present model will be used to simulate diesel combustion in a heavy-duty diesel engine using the updated KIVA-3V that consisted of LES turbulence, KH-RT spray breakup, and detailed chemistry models.

3.2 LES Turbulence Models

LES has traditionally focused on the modeling of sub-grid scale stress tensor. Various types of models have been developed and results were satisfactory compared against experimental data. For turbulent reacting flows with sprays, however, the model development and validation seem to be far less satisfactory due in part to the lack of experimental data. One of the goals of this chapter is to use the LES models to simulate diesel spray combustion.

The compressible LES equations and common closure models are already presented in Chapter 2. Specific models used for this study are further discussed. Note that the filter width is the local grid size. A box filter is used since it is suitable for finite volume method that is used in the present code. It is also assumed that the filtering operation commutes with differentiation, i.e., $\overline{\partial\phi}/\partial t = \partial\bar{\phi}/\partial t$, $\overline{\partial\phi}/\partial x = \partial\bar{\phi}/\partial x$, although this may not hold in a non-uniform mesh (Pomraning and Rutland, 2002).

The filtered terms that require special attention for closure models in reactive flows include the sub-grid scale stress tensor τ_{ij} , sub-grid scale scalar fluxes $\tau_{u_j Y_l}$ and $\tau_{u_j T}$, the subgrid particle-gas interactions $\tau_{F_{si}u_i}$, the filtered rate of momentum gain per unit volume due to spray $\overline{F_i^s}$, and the filtered chemical source term $\bar{\omega}_l^c$.

The subgrid stress tensor τ_{ij} is directly estimated by using the one-equation non-viscosity dynamic structure model (Pomraning and Rutland, 2002), which rescales the Leonard stress tensor L_{ij} with both its trace L_{kk} and the sub-grid scale kinetic energy k

$$\tau_{ij} = \frac{2k}{L_{kk}} L_{ij} . \tag{3.1}$$

The sub-grid scale kinetic energy k is solved from a transport equation that is derived from the filtered momentum equation as

$$\frac{\partial k}{\partial t} + \frac{\partial \tilde{u}_j k}{\partial x_j} = \frac{\partial}{\partial x_j}\left(\nu_t \frac{\partial k}{\partial x_j} \right) - \tau_{ij}\tilde{S}_{ij} - \varepsilon + \tau_{F_{si}u_i} \tag{3.2}$$

where ν_t and ε are modeled from Eq. (2.59) to Eq. (2.60) in Chapter 2. $\tau_{F_{si}u_i}$ is a new unclosed term due to sub-grid gas-droplet interactions and is defined by

$$\tau_{F_{si}u_i} = \overline{u_i F_i^s} - \tilde{u}_i \overline{F_i^s} . \tag{3.3}$$

Adopting the similar modeling approach to the source term used in the $k-\varepsilon$ equations in the RANS approach, this term is modeled by the dot product of aerodynamic drag acting on a particle and turbulent fluctuation as follows (Menon and Pannala, 1997; Banerjee et al., 2009)

$$\tau_{F_{si}u_i} \approx -u_i^{"} \overline{F_i^s} \tag{3.4}$$

where $u_i^{"}$ is the sub-grid i velocity component which cannot be directly resolved and must be modeled. In this study, an approximate deconvolution (Shotorban and Mashayek, 2005) is used to reconstruct the instantaneous velocity from the resolved velocity field by using the truncated Van Cittert series expansion as follows

$$u_i^* = \sum_{n=0}^{N} \left(1-G\right)^n * \tilde{u}_i = \tilde{u}_i + \left(\tilde{u}_i - \tilde{\tilde{u}}_i\right) + \left(\tilde{u}_i - 2\tilde{\tilde{u}}_i + \tilde{\tilde{\tilde{u}}}_i\right) + \ldots \tag{3.5}$$

where u_i^* is the modeled instantaneous velocity component, $\tilde{u}_i, \tilde{\tilde{u}}_i, \tilde{\tilde{\tilde{u}}}_i$ are the filtered values corresponding to the grid level, the second filter level, and the third filter level, respectively. G is the filter kernel. Taking a 2nd order approximation from the above series expansion, the modeled fluctuating component $u_i^{"}$ can then be obtained from Eq. (3.5) as

$$u_i^{"} = u_i^* - \tilde{u}_i = \left(\tilde{u}_i - \tilde{\tilde{u}}_i\right) + \left(\tilde{u}_i - 2\tilde{\tilde{u}}_i + \tilde{\tilde{\tilde{u}}}_i\right) \tag{3.6}$$

The filtered rate of momentum gain per unit volume due to spray $\overline{F_i^s}$ is approximated by using the resolved quantities as in RANS approach (Amsden et al., 1989).

For chemical species, the sub-grid scalar flux $\tau_{u_j Y_l}$ is approximated by the gradient model as

$$\tau_{u_j Y_l} = -\frac{\nu_t}{Sc}\frac{\partial \tilde{Y}_l}{\partial x_j} \tag{3.7}$$

where Y_l is the mass fraction of species l, Sc is the turbulent Schmidt number with a value of 0.68 (Pomraning and Rutland, 2002). However, to be consistent with the non-viscosity model concept used in closing the sub-grid stress tensor, a model that scales with the Leonard-like term should usually be used to close the above sub-grid scalar flux.

The chemical source term $\bar{\omega}_l^c$ and the spray source term $\bar{\omega}_l^s$ are assumed to be equal to the resolved scales. The filtered energy equation is expressed in terms of the resolved temperature as

$$\frac{\partial \bar{\rho} c_v \tilde{T}}{\partial t} + \frac{\partial \bar{\rho}\, c_v \tilde{u}_j \tilde{T}}{\partial x_j} = -\overline{p\frac{\partial u_j}{\partial x_j}} - \frac{\partial \overline{q_j}}{\partial x_j} - \frac{\partial \bar{\rho}\tau_{u_j T}}{\partial x_j} + \overline{\sigma_{ij}\frac{\partial u_i}{\partial x_j}} + \overline{\frac{\partial}{\partial x_j}\left(\rho D \sum_l h_l \frac{\partial Y_l}{\partial x_j}\right)} + \overline{\dot{Q}^c} + \overline{\dot{Q}^s} \tag{3.8}$$

where $\overline{\dot{Q}^c}$ and $\overline{\dot{Q}^s}$ are source terms due to chemical reaction and spray, respectively, and are modeled by the resolved scales. $\overline{q_j}$ is the molecular heat flux and is approximated by neglecting the sub-grid scale of thermal conductivity. c_v is the total specific heat of the mixture at constant volume. For low to moderate Mach number flow typical of engine in-cylinder flows, the first and fourth terms are approximated as follows (Moin et al., 1991; Vreman et al., 1994)

$$\overline{p\frac{\partial u_j}{\partial x_j}} \cong \bar{p}\frac{\partial \tilde{u}_j}{\partial x_j} \tag{3.9}$$

$$\overline{\sigma_{ij}\frac{\partial u_i}{\partial x_j}} \cong \tilde{\sigma}_{ij}\frac{\partial \tilde{u}_i}{\partial x_j}. \tag{3.10}$$

Similarly, the fifth term is approximated by neglecting the sub-grid scale effect as

$$\overline{\frac{\partial}{\partial x_j}\left(\rho D\sum_l h_l\frac{\partial Y_l}{\partial x_j}\right)} = \frac{\partial}{\partial x_j}\left(\overline{\rho} D\sum_l \tilde{h}_l\frac{\partial \tilde{Y}_l}{\partial x_j}\right). \tag{3.11}$$

The sub-grid heat flux term τ_{u_jT} is defined as

$$\tau_{u_jT} = c_v\left(\widetilde{u_jT} - \tilde{u}_j\tilde{T}\right) \tag{3.12}$$

and is modeled by the gradient method analogous to the sub-grid scalar flux $\tau_{u_jY_m}$ as

$$\tau_{u_jT} = -\frac{c_p\nu_t}{\mathrm{Pr}_t}\frac{\partial\tilde{T}}{\partial x_j} \tag{3.13}$$

where Pr_t is the turbulent Prandtl number with the value of 0.9 (Amsden et al., 1989). c_p is the total specific heat of the mixture at constant pressure. The calculations of c_p and c_v are taken as the summations of mass-weighted value of each individual species (Amsden et al., 1989).

As discussed in Chapter 2, spray modeling has been shown to be dependent on the grid resolution due to a number of reasons. One of the reasons is that the representative gas phase flow quantities at the particle location cannot be directly solved due to the use of finite grid points. To improve the gas-to-liquid momentum exchange, the gas phase velocity at the particle location is taken as a weighted value of the velocity of each node of the cell containing the particle by using an interpolation scheme (Nordin, 2001) as

$$\mathbf{u}_{g,p} = \sum_{n=1}^{8} w_n \mathbf{u}_{g,n} \tag{3.14}$$

where $\mathbf{u}_{g,p}$ is the gas phase velocity at the particle location, $\mathbf{u}_{g,n}$ is the nodal gas phase velocity, and w_n is the weight associated with the distance between each node and the particle by

$$w_n = \frac{l_{n,p}^{-2}}{\sum_{i=1}^{8} l_{i,p}^{-2}} \tag{3.15}$$

where $l_{i,p}$ indicates the distance between the node i and the particle p.

3.3 Combustion and Emissions Models

Engine combustion can involve hundreds of species and thousands of reactions with a wide spectrum of chemical time scales. Different combustion modes can also have different critical events. For instance, ignition and mixing are significant processes for diesel combustion whereas flame propagation is important for gasoline combustion. This section will describe the chemical kinetics used to simulate diesel spray ignition, combustion, and emissions formation.

In the current combustion model, the sub-grid scale turbulence-chemistry interactions are not considered and the mean reaction rate is assumed to be controlled mainly by the kinetics. Nonetheless, turbulence influences chemical reactions through species transport and mixing at the grid level. The chemical reactions are directly solved at each computational time step.

The rate of change of mass fraction for a species l is given by treating each computational cell as a chemical reactor (Kong et al., 2007b)

$$\frac{dY_l}{dt} = \frac{\dot{\omega}_l W_l}{\rho} \tag{3.16}$$

where Y_l is the mass fraction of species l, $\dot{\omega}_l$ is the concentration production rate, W_l is the molecular weight of species l, and ρ is the total density. Assuming a constant cell volume, the energy equation can be written as

$$\rho c_v \frac{dT}{dt} + \sum_{l=1}^{L} e_l \dot{\omega}_l W_l = 0 \tag{3.17}$$

where c_v is the specific heat of the mixture at constant volume, T is the cell temperature, and e_l is the specific internal energy of species l. In the context of LES, ρ, T, and Y_l are the resolved quantities.

Diesel fuel is a mixture composed of approximately 200 to 300 hydrocarbon species. A comprehensive reaction mechanism for practical diesel fuel is not available. In this study, a skeletal reaction mechanism for n-heptane oxidation was used to simulate diesel fuel chemistry due to their similar ignition characteristics and cetane numbers (Patel et al., 2004). The resulting mechanism retained the main features of the detailed mechanism and included reactions of polycyclic aromatic hydrocarbons. Additionally, a reduced NO mechanism was obtained by using the same reduction methodology based on the Gas Research Institute (GRI) NO mechanism (Smith et al., 2000). The resulting NO mechanism contained only four additional species (N, NO, NO_2, N_2O) and nine reactions that describe the formation of nitric oxides.

The NO mechanism was incorporated into the mechanism for n-heptane oxidation to form a skeletal reaction mechanism for the diesel fuel chemistry used in this study. As a result, the reaction mechanism for fuel oxidation and NO_x emissions consisted of 34 species and 74 reactions (Kong et al., 2007b). The CHEMKIN chemistry solver was implemented into KIVA in order to use the above reaction mechanism for diesel combustion simulation.

The capability to predict the engine-out soot emissions is important for a CFD model, and the predicted engine-out soot can also provide the boundary condition for after-treatment modeling. A phenomenological soot model (Han et al., 1996) was used to predict soot emissions in this study. Two competing processes, soot formation and soot oxidation, were combined to determine the rate of change of soot mass as

$$\frac{dM_s}{dt} = \frac{dM_{sf}}{dt} - \frac{dM_{so}}{dt} \tag{3.18}$$

where M_s , M_{sf} , M_{so} are the masses of the soot, soot formation, and soot oxidation, respectively. The formation rate uses an Arrhenius expression and the oxidation rate is based on a carbon oxidation model, described respectively as

$$\frac{dM_{sf}}{dt} = A_{sf} M_{C_2H_2} P^n \exp\left(-\frac{E_{sf}}{RT}\right) \tag{3.19}$$

$$\frac{dM_{so}}{dt} = \frac{6Mw_c}{\rho_s D_s} M_s R_{Total} \tag{3.20}$$

where $M_{C_2H_2}$, Mw_c , P , T , R_{Total} , R are acetylene mass, soot molecular weight, pressure, temperature, surface mass oxidation rate, and the universal gas constant, respectively. ρ_s

and D_s are soot density and average particle diameter. The soot formation rate uses acetylene (C_2H_2) as the inception species in Eq. (3.19) since acetylene is the most relevant species pertaining to soot formation in the present reaction mechanism (Kong et al., 2007a). The soot oxidation rate is determined by the Nagle-Strickland-Constable model that considers carbon oxidation by two reaction pathways whose rates depend on the surface chemistry of two different reactive sites (Han et al., 1996). Model constants are $A_{sf} = 150$, $E_{sf} = 52,335$ Joule$\cdot mol^{-1}$, $\rho_s = 2\ g \cdot cm^{-3}$, and $D_s = 2.5 \times 10^{-6} cm$. In the present calculation, acetylene was assumed to form soot particles which, in turn, were converted to CO, CO_2 and H_2 as a result of oxidation. Again, in the context of LES, the above equations used the resolved quantities.

3.4 Spray Combustion Modeling

Diesel spray simulations were performed in two constant-volume chambers to validate the LES models. First, a non-evaporating diesel spray was simulated using both the RANS and LES approaches. Then, diesel spray combustion in a combustion chamber was simulated using both LES and RANS approaches to demonstrate the capability of LES. Note that spray sub-models developed in the context of the RANS approach were retained in LES simulations except that all the RANS-based scales were replaced by the LES-based scales. For instance, the turbulent kinetic energy was replaced by the subgrid scale kinetic energy, and the turbulent dissipation rate was replaced by the subgrid kinetic energy dissipation rate.

Among the sub-models, the fuel spray atomization was simulated by modelling the growth of unstable surface waves on the liquid surface that will result in drop breakup (Patterson and Reitz, 1998; Kong et al., 1999). In the combustion case, combustion chemistry was simulated by using a skeletal n-heptane mechanism for fuel oxidation and NO_x emissions that consisted of 34 species and 74 reactions. The phenomenological soot model discussed in the previous section was used to predict soot emissions. Other sub-models included those for spray/wall interaction, wall heat transfer, and piston-ring crevice flow. Before the development of a good wall model for LES, the present approach used the RANS-based wall function, i.e., the turbulent law-of-the-wall conditions and fixed temperature walls. This was also to prevent the use of very fine mesh in the near-wall region. Thus, the present practice belongs to a hybrid RANS/LES approach, as often referred to Very Large Eddy Simulation (VLES) (Pope, 2000).

Non-evaporative spray in a constant chamber

A non-evaporating diesel spray in a constant-volume chamber was simulated using the LES approach to validate the LES models. Predicted spray structure and liquid penetration will be compared with experimental data (Dan et al., 1997; Hori et al., 2006). The LES results will also be compared with RANS results in terms of liquid penetration, spray structure, velocity vector, and vortex structure. It should be noted that instantaneous LES results should be ensemble- or time-averaged to compare to ensemble-averaged experimental results. However, due to the significant time required for the averaging, the instantaneous LES results were used for comparison. In the RANS approach, RNG $k-\varepsilon$ model was used whereas in the LES approach, the subgrid kinetic energy was solved from the transport equation. Spray was

injected at the center of the top surface along the chamber axis. All simulations had the same computational duration, i.e., started from zero and ended at 4 ms. **Table 3.1** lists the simulation conditions.

Table 3.1. Simulation conditions for a non-evaporative spray.

Fuel	n-$C_{13}H_{28}$
Injection duration	1.8 ms
Injection profile	Top-hat
Injection orifice diameter	200 μm
Orifice pressure drop	77 MPa
Fuel mass	0.012 g
Fuel temperature	300 K
Ambient temperature	300 K
Ambient pressure	1.5 MPa
Ambient density	17.3 kg/m^3
Ambient gas	N_2
Number of computational parcels	2000
Bore (cm) × stroke (cm)	3.0 × 10.0
Cell division number (radial × azimuthal × axial)	8×60×50, 15×60×100, 30×60×200
Spray models	All improved sub-models excluding evaporation model
Turbulence model	LES subgrid models and RNG - $k-\varepsilon$

To test the effect of grid resolution on simulation results, three different mesh sizes were used, as shown in **Figure 3.1**, which corresponded to the division numbers of 8×60×50, 15×60×100, and 30×60×200 in radial, azimuthal and axial directions, or approximately an averaged radial cell size of 2 mm, 1 mm, and 0.5 mm, respectively. Meanwhile, all meshes were created as cylindrical meshes since this type of mesh has been shown to be able to reduce the grid dependence of spray simulation due to a better resolution in the azimuthal direction (Hieber, 2001; Baumgarten, 2006).

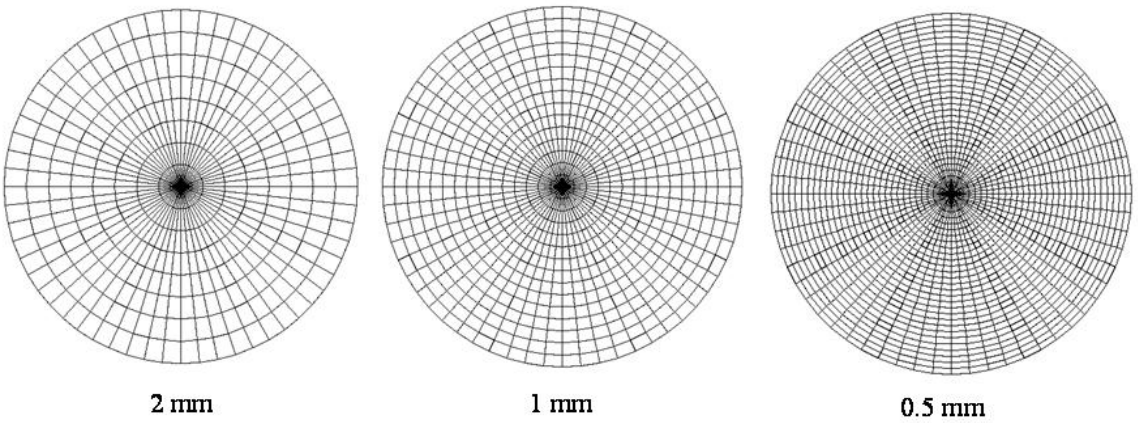

Figure 3.1. Three mesh sizes used in non-evaporative spray simulations in a constant volume chamber (top view, injector is located at the center).

No-slip boundary was enforced for velocity, and fixed temperature was enforced for wall temperature. For other scalars, zero fluxes were enforced at the wall boundaries. Initial gas velocity was set to zero, and initial temperature and pressure were set to the values as in the experiments. For the RANS approach, initial k was set to the given input value and initial ε was calculated from k and the given integral length scale (Amsden et al., 1989). For the subgrid kinetic energy in LES, its initial value was given a negligibly small value (Chumakov, 2005).

Figure 3.2 shows the history of the liquid penetration using different mesh sizes in the LES simulations. Note that the liquid penetration is defined as the axial distance from the nozzle orifice to the location that corresponds to 95% of integrated fuel mass of total injected fuel from the orifice. It is seen that the predicted liquid penetrations agree better with experimental data as the mesh size is reduced due mainly to the fact that LES can resolve

more flow structures for the finer mesh. The liquid penetrations using the finest mesh (0.5 mm) match very well with experimental data (Dan et al., 1997; Hori et al., 2006). It is also seen that spray penetration is still dependent on the grid resolution although an interpolation method was used to obtain a weighted gas velocity at the particle location in order to reduce this dependence. Further improvements to the liquid-to-gas coupling terms and the drop collision model may be needed in order to eliminate this grid dependence. **Figure 3.3** shows the liquid penetrations using different mesh sizes in the RANS simulations. The simulated penetrations also match quite well with experimental data for the finest grid size (0.5 mm). However, LES predicted overall better penetrations than RANS in the entire history due to the fact that LES can resolve large turbulent eddies and only need to model subgrid eddies, whereas RANS needs to model all turbulent eddies.

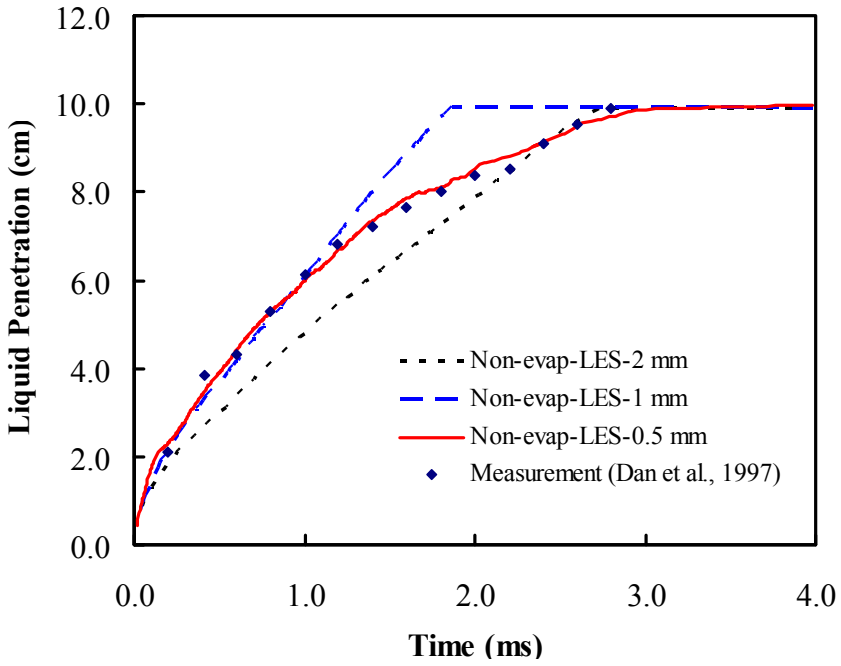

Figure 3.2. Spray liquid penetrations using different grid sizes in LES simulations.

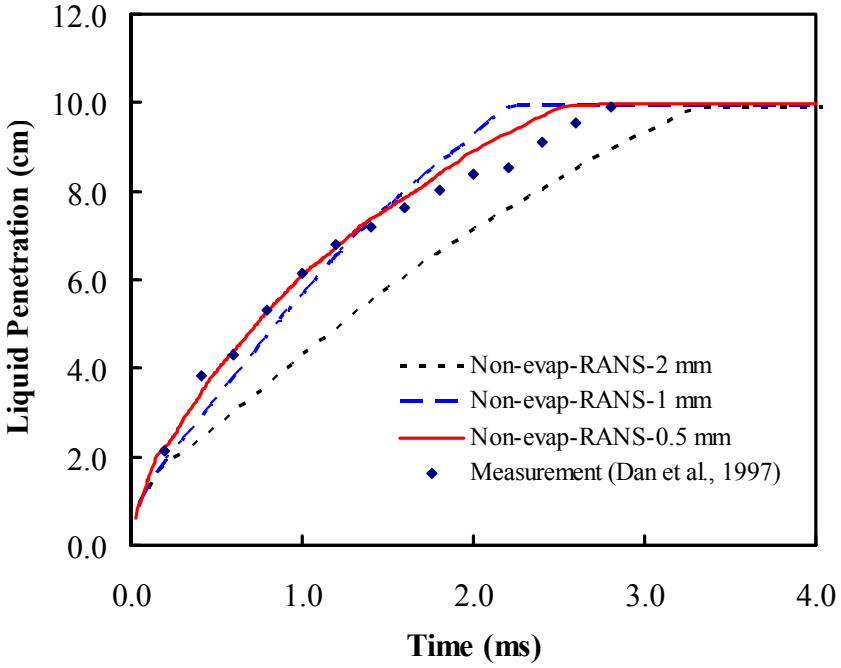

Figure 3.3. Spray liquid penetrations using different grid sizes in RANS simulations.

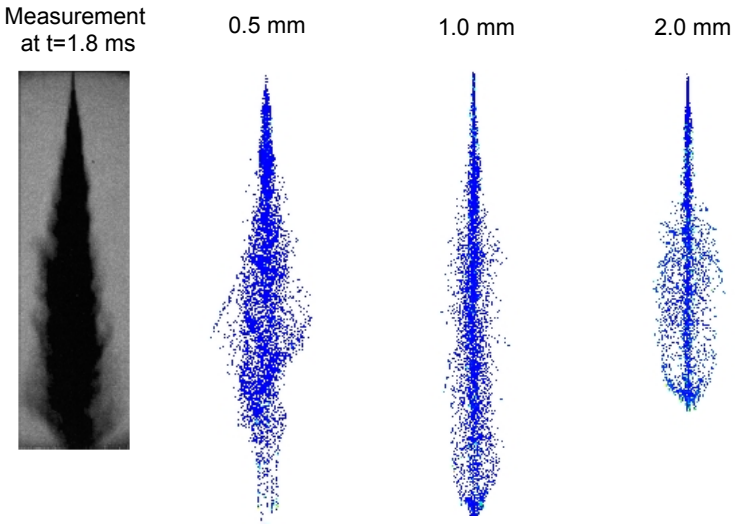

Figure 3.4. Spray structure using different grid sizes in LES simulations at 1.8 ms (measurement by Dan et al., 1997).

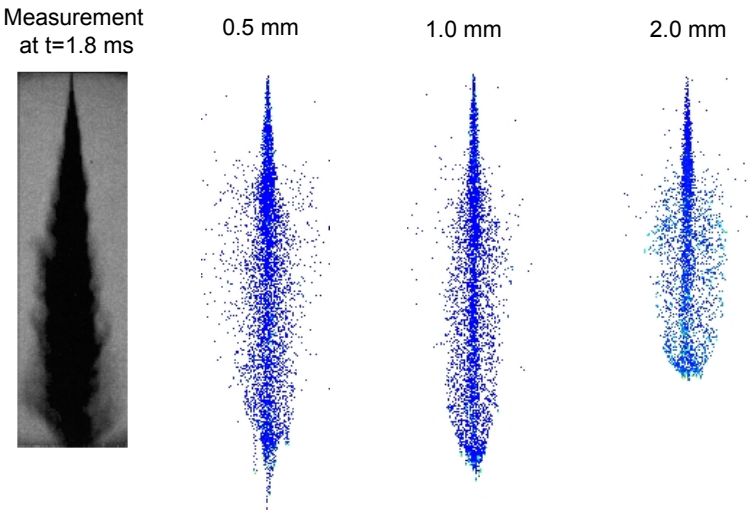

Figure 3.5. Spray structure using different grid sizes in RANS simulations at 1.8 ms (measurement by Dan et al., 1997).

Figure 3.4 and **Figure 3.5** show spray structures using different mesh sizes in the LES and RANS simulations, respectively. As the grid size was reduced, LES predicted a more realistic spray structure than RANS by comparing the predicted drop distributions with the experimental image. In particular, the LES approach using the finest mesh could predict the dynamic structure that was not observed in the RANS results. For the finest mesh, both LES and RANS predicted some overly dispersed particles at the leading edge of the spray. The differences of the spray structure between LES and RANS can also be seen from the gas velocity vector on a central cutplane (**Figure 3.6**) and the 3-D vortex structure (**Figure 3.7**). The vortex structure was visualized by using a positive value of the second invariant $\left(Q = -\frac{1}{2}\frac{\partial u_i}{\partial x_j}\frac{\partial u_j}{\partial x_i} \right)$ of the velocity gradient tensor, the so-called $Q-$criterion, which can be used to indicate resolved coherent structures (Hunt et al., 1988; Dubief and Delcayre, 2000;

Fujimoto et al., 2009). Alternatively, Q indicates a relative movement between rotation and deformation (Dubief and Delcayre, 2000) and can be defined as

$$Q = \frac{1}{2}\left(\Omega_{ij}\Omega_{ij} - S_{ij}S_{ij}\right) \tag{3.21}$$

where Ω_{ij} and S_{ij} are the vorticity tensor and the rate of strain tensor, respectively, and defined as follows

$$\Omega_{ij} = \frac{1}{2}\left(\frac{\partial u_i}{\partial x_j} - \frac{\partial u_j}{\partial x_i}\right), S_{ij} = \frac{1}{2}\left(\frac{\partial u_i}{\partial x_j} + \frac{\partial u_j}{\partial x_i}\right). \tag{3.22}$$

Thus, a positive value of Q represents vortex. The critical value of Q, which gives the highest level of vorticity fluctuations, is determined based on the characteristic parameters as (Domingo et al., 2006)

$$Q_c = \frac{\overline{V}_{inj}}{2d_{nozzle}} \tag{3.23}$$

where $\overline{V}_{inj}$ is the average injection velocity, and d_{nozzle} is the nozzle diameter. **Figure 3.7** shows an iso-surface of Q corresponding to its critical value of $Q_c = 10^6$ for both RANS and LES simulations. The LES result shows a clear 3-D coherent vortex tubes which are not equally observed in the RANS result due to the nature of its statistical average and entirely modeled turbulence. Although the coherent vortex structure can be predicted by the current LES approach, the evolution of this structure may have been suppressed because the current convective calculation using the quasi-second order upwind scheme may result in numerical diffusion (Hori et al., 2008). Low numerical diffusion scheme may be needed for the convection calculation in LES simulation (Fujimoto et al., 2009).

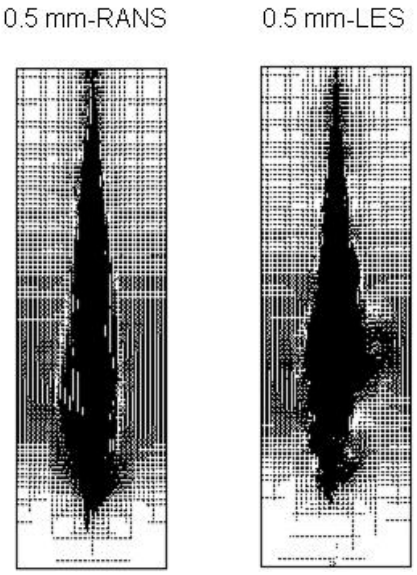

Figure 3.6. Velocity vector on a central cutplane (y=0) in both RANS and LES simulations at 1.8 ms.

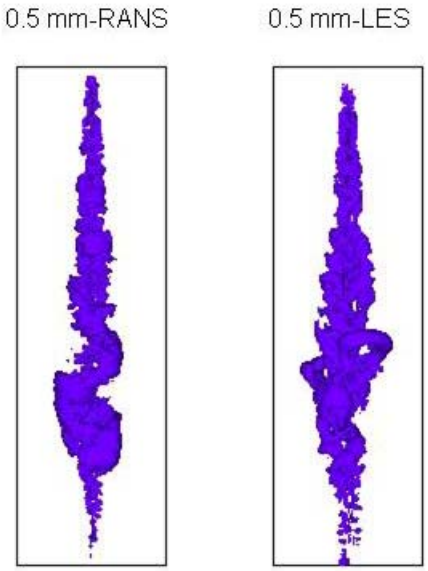

Figure 3.7. Vortex structure plotted as an iso-surface of the critical value Q_c of 1.0e+6 in both RANS and LES simulations at 1.8 ms.

Diesel spray combustion in a constant-volume chamber

The purpose of the present modeling was to demonstrate the capability of LES to predict the dynamic flame structure and soot distribution in a diesel combustion flame. The flame structure of diesel spray in a constant-volume combustion chamber was studied in Sandia National Laboratory using laser diagnostics (Pickett and Siebers, 2004; Siebers and Pickett, 2004). The details of the flame structure have provided new insights into the combustion and emission formation processes in diesel sprays and provided data for model validation (Kong et al., 2003; Tao et al., 2004). For instance, a diesel flame consists of a diffusion zone at the fuel jet periphery, where NO_x is formed, and a fuel rich reaction zone in the center of fuel spray, where the majority of soot is formed (Kong et al., 2007a). Additionally, the flame lift-off length will determine the time available for fuel-air mixing prior to ignition and entering the reacting zone and thus will affect the sooting tendency of the diesel fuel jet. The numerical simulation of the diesel flame using the RANS approach coupled with detailed chemistry gave satisfactory results in global quantities such as the lift-off length, mean cylinder pressure, heat release rate, and soot and NO_x emissions (Kong et al., 2007a). However, due to its statistical nature, the RANS approach was not able to predict the dynamic flame structure which can be important to the prediction of the soot and NO_x distributions. This study was to test the capability of the current LES approach to simulate a diesel flame when coupled with detailed chemistry and a phenomenological soot model.

Experimental data of the Sandia diesel combustion chamber were used to validate the current LES models. The baseline experimental conditions were list in **Table 3.2**. The computational domain was 6.3 cm in diameter and 10.0 cm in height. The computations used

a cylindrical mesh with an average grid size of 2 mm in both radial and axial directions. The spray was injected from the top surface and directed downward along the cylinder axis. Spray dynamics were modeled by the improved sub-models as discussed previously. Combustion chemistry was simulated by using a skeletal n-heptane mechanism for fuel oxidation and NO_x emissions that consisted of 34 species and 74 reactions, while soot emissions was modeled using a phenomenological model. Similar boundary and initial conditions to the non-evaporative spray case were applied. RANS simulations using the RNG $k-\varepsilon$ turbulence model were also performed for comparison.

Table 3.2. Experimental conditions for model validation.

Fuel	#2 diesel
Injection system	Common-rail
Injection profile	Top-hat
Injection orifice diameter	100 μm
Orifice pressure drop	138 MPa
Discharge coefficient	0.8
Fuel temperature	436 K
Ambient temperature	1000 K
Ambient pressure	4.18 MPa
Ambient density	14.8 kg/m^3
O_2 concentration	21%

Figure 3.8 shows the comparison of soot distributions on a central cutplane among RANS, experimental, and LES results. **Figure 3.9** shows the comparison of soot iso-surfaces at different times. The experimental images were obtained from planar laser induced incandescence (PLII) that indicated the soot mass along the laser path (Pickett and Siebers, 2004). It can be seen that LES predicted both the dynamic structure and lift-off length closer to the experiment than those by RANS which mostly predicted an axisymmetric soot

distribution. The different soot distributions predicted by LES and RANS indicated the differences in local flow parameters predicted by the two approaches. These local flow parameters were directly linked to the local equivalence ratio which was largely determined by the turbulent mixing. The LES can resolve more flow structures and thus more dynamic soot structures can be seen in the LES results. However, LES seems to over-predict the fuel vapor penetration resulting in an over-extended reaction zone. Further improvements in LES for predicting evaporating sprays are required.

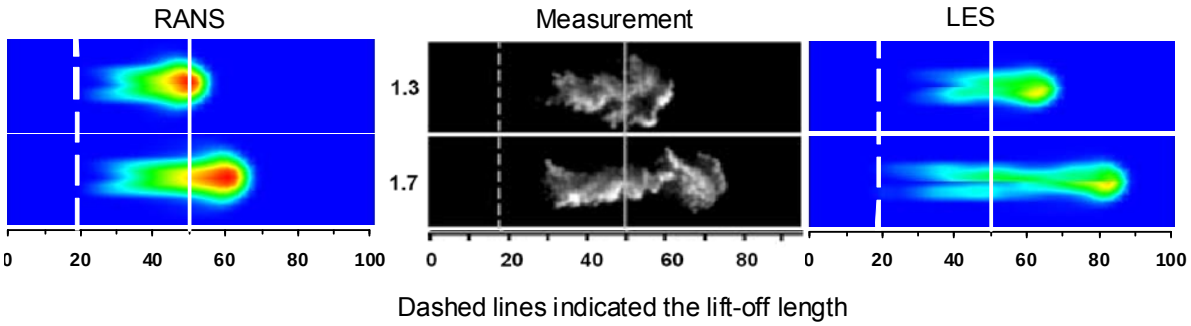

Figure 3.8. Comparison of soot distributions at 1.3 and 1.7 ms after start of injection for d_{nozzle}=100 μm, T_{amb}=1000 K, ΔP_{amb}=138 MPa, ρ_{amb}=14.8 kg/m^3 (measurement by Pickett and Siebers, 2004).

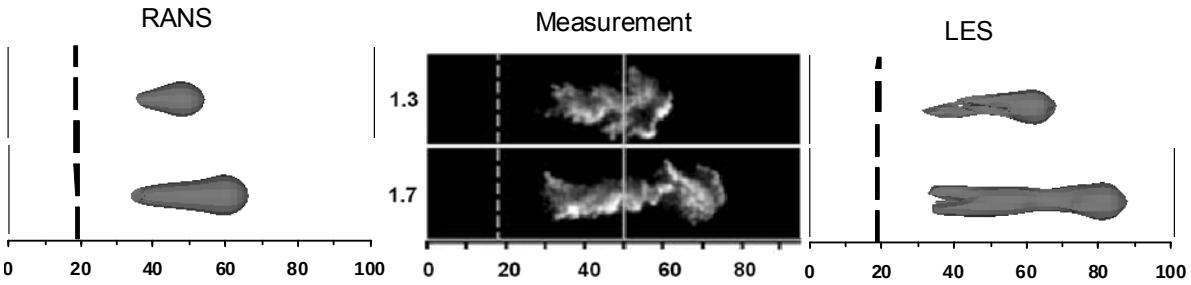

Figure 3.9. Comparison of soot iso-surface predicted by RANS and LES and the experimental PLII images (Pickett and Siebers, 2004) for d_{nozzle}=100 μm, T_{amb}=1000 K, ΔP_{amb}=138 MPa, ρ_{amb}=14.8 kg/m^3.

To further demonstrate the distinct flame structures predicted by the LES and RANS approach, **Figure 3.10** shows the comparison of temperature at different times. Although no experimental data were available for comparison, a similar conclusion as in the soot analysis can be drawn that LES predicted a more dynamic, and likely more realistic, reaction zone structure. Additionally, LES predicted thinner diffusion flame which is consistent with experimental observation of NO_x distribution (Dec, 1997) since thermal NO is very sensitive to temperature above 1900 K (Law, 2006).

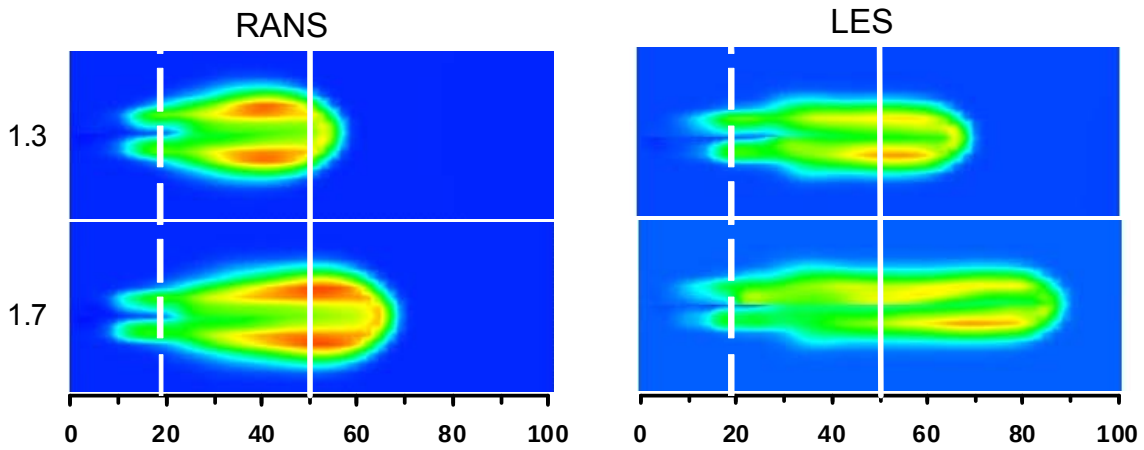

Figure 3.10. Comparison of predicted temperature distributions using RANS and LES for d_{nozzle}=100 μm, T_{amb}=1000 K, ΔP_{amb}=138 MPa, ρ_{amb}=14.8 kg/m^3.

3.5 Diesel Engine Simulation

The present model was also applied to simulate the in-cylinder spray combustion process in a diesel engine. As in the spray simulations in the previous section, the fuel spray atomization was simulated by modelling the growth of unstable surface waves on the liquid surface that will result in drop breakup (Patterson and Reitz, 1998; Kong et al., 1999). Combustion

chemistry was simulated by using a skeletal n-heptane mechanism for fuel oxidation and NO_x emissions that consisted of 34 species and 74 reactions. The phenomenological soot model (Han et al., 1996) was used to predict soot emissions. Other sub-models included spray/wall interactions, wall heat transfer, and crevice flows. The turbulent law-of-the-wall conditions and fixed temperature walls were enforced near solid walls.

Table 3.3. Engine specifications and operating conditions.

Engine model	Caterpillar 3401 SCOTE
Bore × stroke	137.2 mm × 165.1 mm
Compression ratio	16.1:1
Displacement	2.44 Liters
Connecting rod length	261.6 mm
Squish height	1.57 mm
Combustion chamber geometry	In-piston Mexican hat with sharp edged crater
Piston	Articulated
Charge mixture motion	Quiescent
Injector	HEUI
Maximum injection pressure	190 MPa
Number of nozzle holes	6
Nozzle hole diameter	0.214 mm
Included spray angle	145˚
Injection rate shape	Rising
Experimental conditions for model validations (Klingbeil et al., 2003)	
Case group	SOI (ATDC)
A (8% EGR)	-20, -15, -10, -5, 0, +5
B (27% EGR)	-20, -15, -10, -5, 0, +5
C (40% EGR)	-20, -15, -10, -5, 0, +5

The specifications of the engine are listed in **Table 3.3** (Li and Kong, 2008). The engine operating conditions were optimized to achieve low NO_x and particulate emissions by varying the start-of-injection (SOI) timing and exhaust gas recirculation (EGR). The experimental results indicated that low emissions could be achieved by optimizing the

operating conditions to allow an optimal time interval between the end of fuel injection and the start of combustion. This is to allow a longer mixing time for a more homogeneous mixture. In this study, the cylinder pressure history and exhaust soot and NO_x emissions were used for model validations.

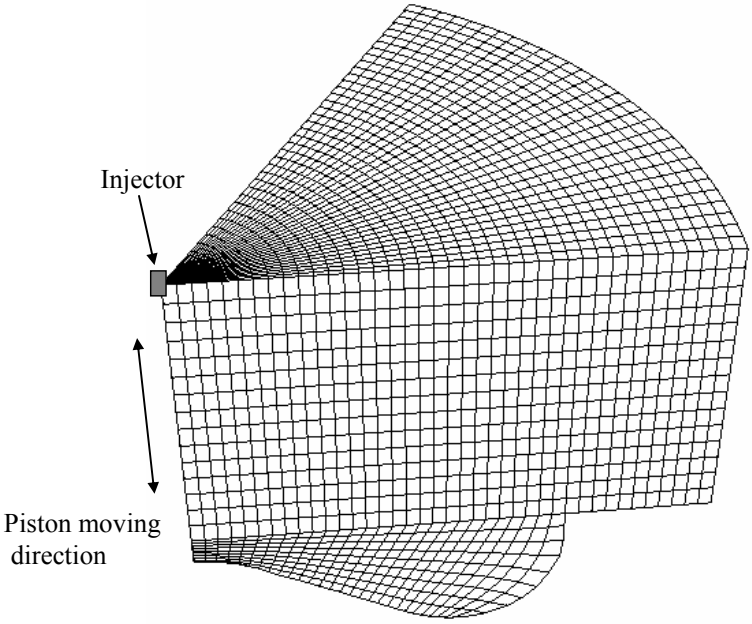

Figure 3.11. Computational mesh (a 60° sector mesh).

The computation used a 60-degree sector mesh that included a full spray plume since the injector had six nozzle holes that were uniformly oriented in the circumferential direction. The injector was located at the top of the domain as shown in **Figure 3.11**. The average grid size was approximately 2 mm and the number of computational cells was approximately 20,000 at bottom-dead-center. The cylindrical mesh was finer near the injector for fuel spray simulations. The present mesh resolution was considered to be adequate for engine modeling and has been used in RANS simulations in previous studies (Kong et al., 2007b; Kong et al.,

2007a). A mesh sensitivity study of using the present LES model also showed that the predicted global properties, i.e. cylinder pressures, match well between a standard mesh and a fine mesh with four times of the standard mesh number (Jhavar and Rutland, 2006). The current mesh was adequate for the present engineering application since the model will be validated by comparing the global parameters such as cylinder pressures and soot and NO_x emissions.

Simulations started from intake valve closure (IVC) with a swirl ratio of 1.0 and a uniform mixture of air and EGR was specified. Wall temperature boundary conditions used 433 K for the cylinder wall, 523 K for the cylinder head and 553 K for the piston surface. Computations ended at exhaust valve open (EVO) when predicted soot and NO_x emissions were compared with engine exhaust measurements.

Operating conditions listed in **Table 3.3** were simulated with the same set of model constants and kinetics parameters. In general, the model performed well in predicting combustion for the range of conditions studied. **Figure 3.12** shows the comparisons in cylinder pressure histories and heat release rate data for 8% EGR cases. The present model predicted correct ignition timing and combustion phasing. Note that similar levels of agreement between measurements and predictions were also obtained for the other cases (not shown here for brevity). A large portion of premixed burn was observed under the present engine conditions, as also predicted by the model. Although the present mesh is not as fine as those usually used in LES modeling, the possible non-equilibrium effects (i.e. the filter cutoff is in the inertial

range) are reasonably accounted for by the use of the transport equation for the sub-grid kinetic energy.

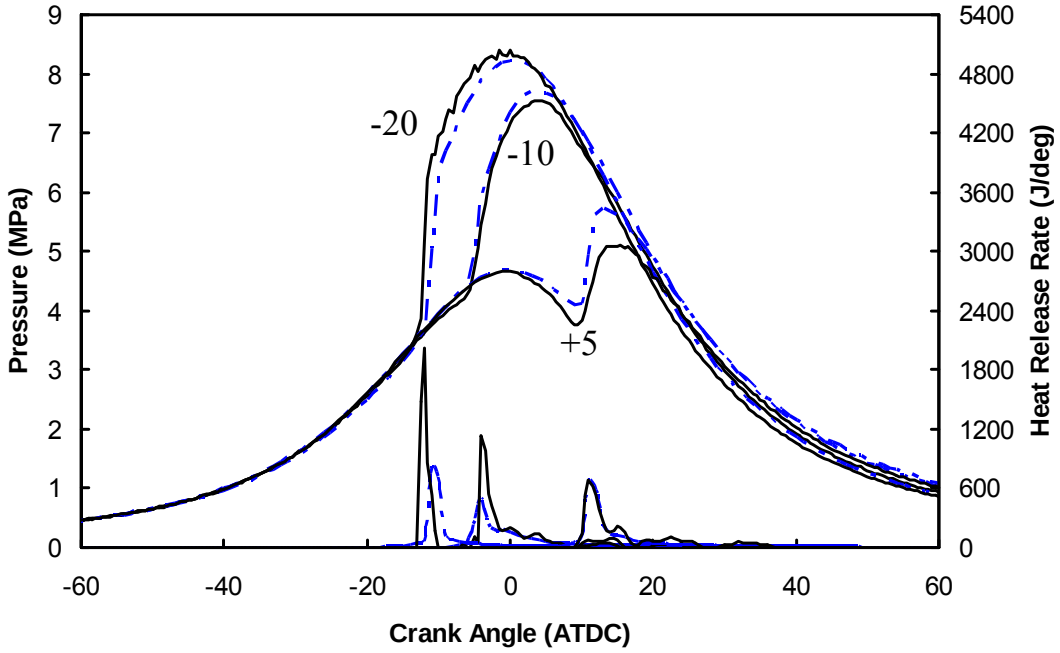

Figure 3.12. Comparisons of measured (solid lines) (Klingbeil et al., 2003) and predicted (dashed) cylinder pressure and heat release rate data for SOI = –20, –10 and +5, both with 8% EGR.

Soot and NO_x are two major pollutants of diesel engines and are difficult to be predicted accurately over a wide range of operating conditions. Predictions of soot and NO_x emissions strongly depend upon the model accuracy in predicting both the overall combustion and the local mixture conditions. **Figure 3.13** shows the history of the in-cylinder soot and NO_x mass compared with the engine-out exhaust measurements. It is seen that NO_x chemistry freezes during expansion due to decreasing gas temperature. The history of soot mass indicates that soot is formed continuously at the beginning and a large amount of soot is oxidized later in the engine cycle.

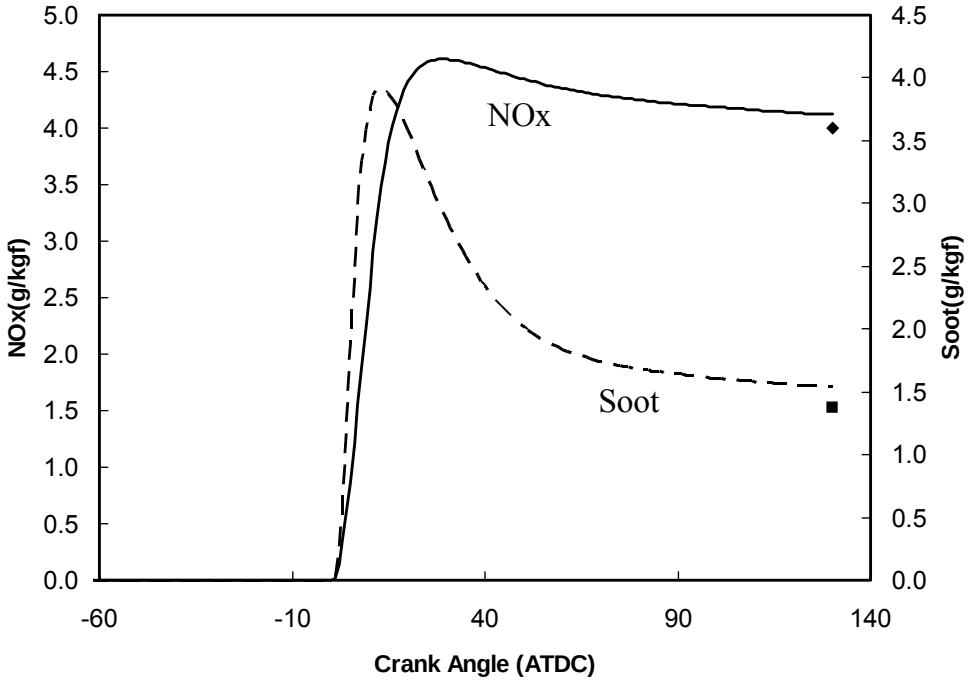

Figure 3.13. Evolutions of predicted in-cylinder soot and NOx emissions compared with engine exhaust measurements (solid symbols) (Klingbeil et al., 2003) for SOI = –5 ATDC, 40% EGR.

Figure 3.14 to **Figure 3.16** show comparisons of predicted and measured soot and NO_x emissions. The trend and magnitude of NO_x emissions are well predicted, indicating that the chemical kinetics used in this study is adequate for the present conditions including the low temperature combustion regimes at high EGR levels. It is known that NO_x formation is characterized by slow chemistry and sensitive to local temperatures. Model results indicate that the instantaneous local species concentrations are reasonably modeled by the present LES approach without considering the sub-grid scale effect of chemical reactions.

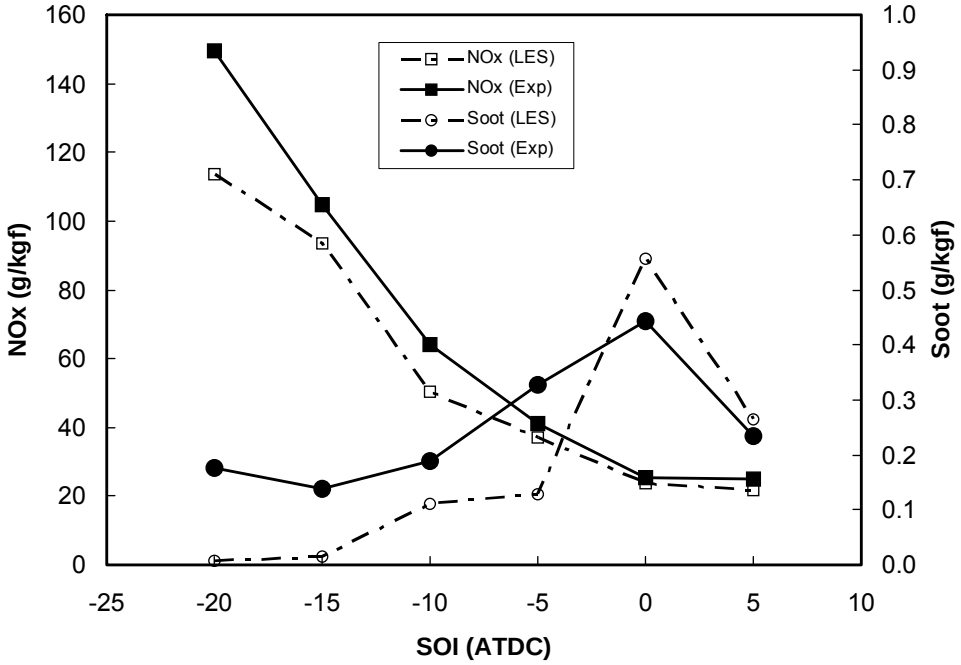

Figure 3.14. Comparisons of measured (Klingbeil et al., 2003) and predicted soot and NOx emissions for 8% EGR cases.

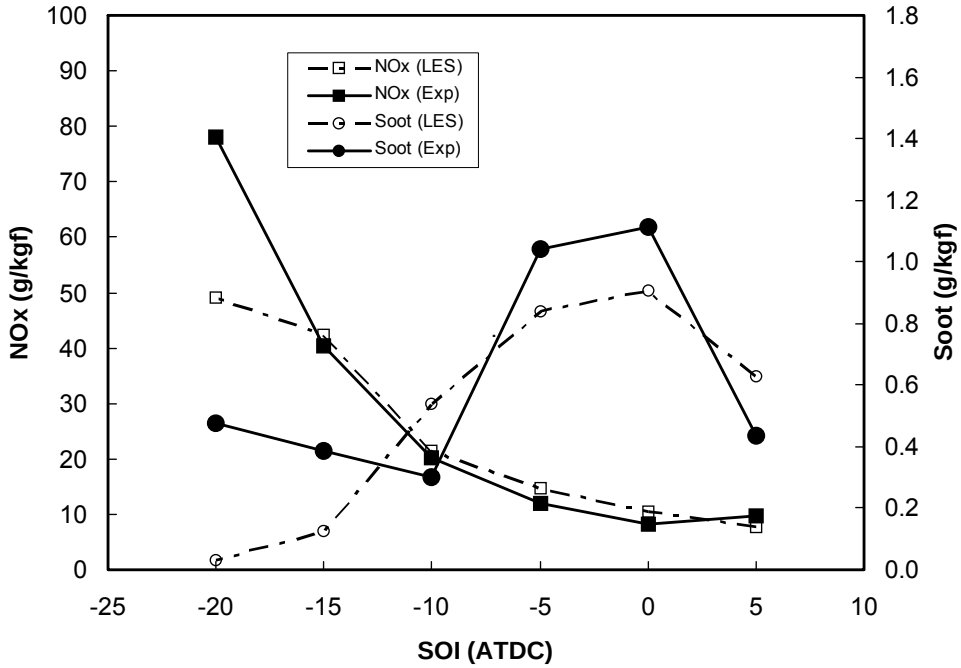

Figure 3.15. Comparisons of measured (Klingbeil et al., 2003) and predicted soot and NOx emissions for 27% EGR cases.

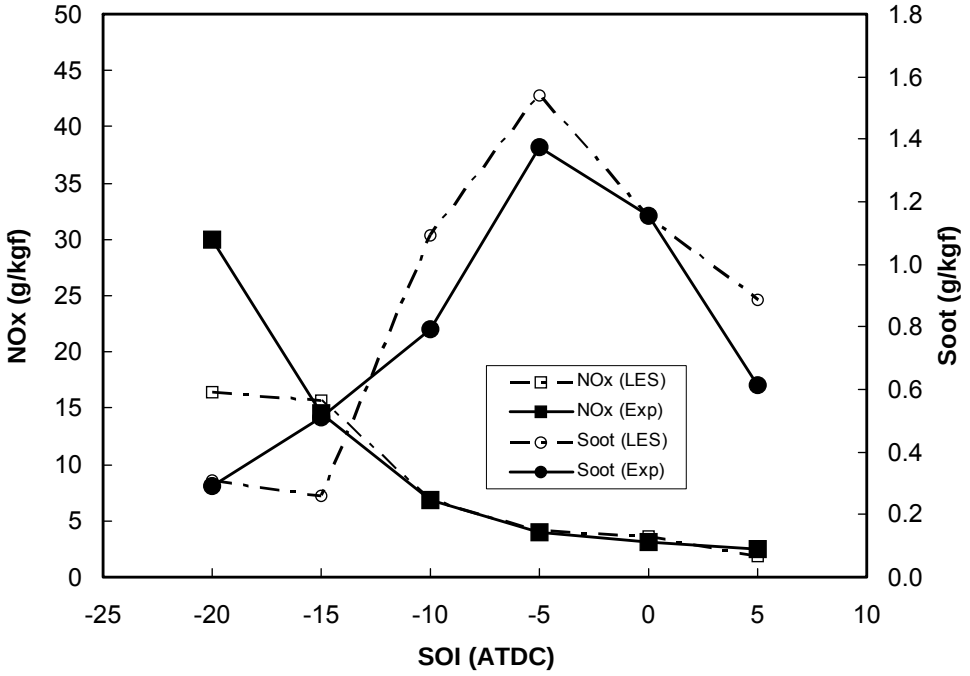

Figure 3.16. Comparisons of measured (Klingbeil et al., 2003) and predicted soot and NOx emissions for 40% EGR cases.

The trends of soot emissions with respect to SOI and EGR are predicted reasonably well except for the early injection cases for 27% EGR. In general, early fuel injection (e.g. –20 ATDC) will result in high combustion temperatures that enhance soot oxidation and lower exhaust soot emissions. As the injection timing is retarded toward top-dead-centre (TDC), soot emissions increases due to poor oxidation. As the injection timing is further retarded passing TDC, in-cylinder gas temperature decreases noticeably, resulting in significantly lower soot formation rates and final soot emissions. The model is able to predict the peak of soot emissions occurring at SOI near TDC for various EGR levels.

It is of interest to demonstrate the unsteadiness of in-cylinder flows predicted by the present LES approach and compare the flow structure with that predicted by the RANS models.

Figure 3.17 shows the fuel spray and temperature distributions for SOI = –20 ATDC with 8% EGR. It is seen that the LES model is able to predict the unsteady flow structure during the engine process. Differences in CO mass fraction distributions predicted by both LES and RANS are also observed, as shown in **Figure 3.18**. It can be seen that LES models can indeed capture more detailed flow structures and can be further developed into a tool to address variations due to subtle changes in engine operating conditions as well as cycle-to-cycle variations.

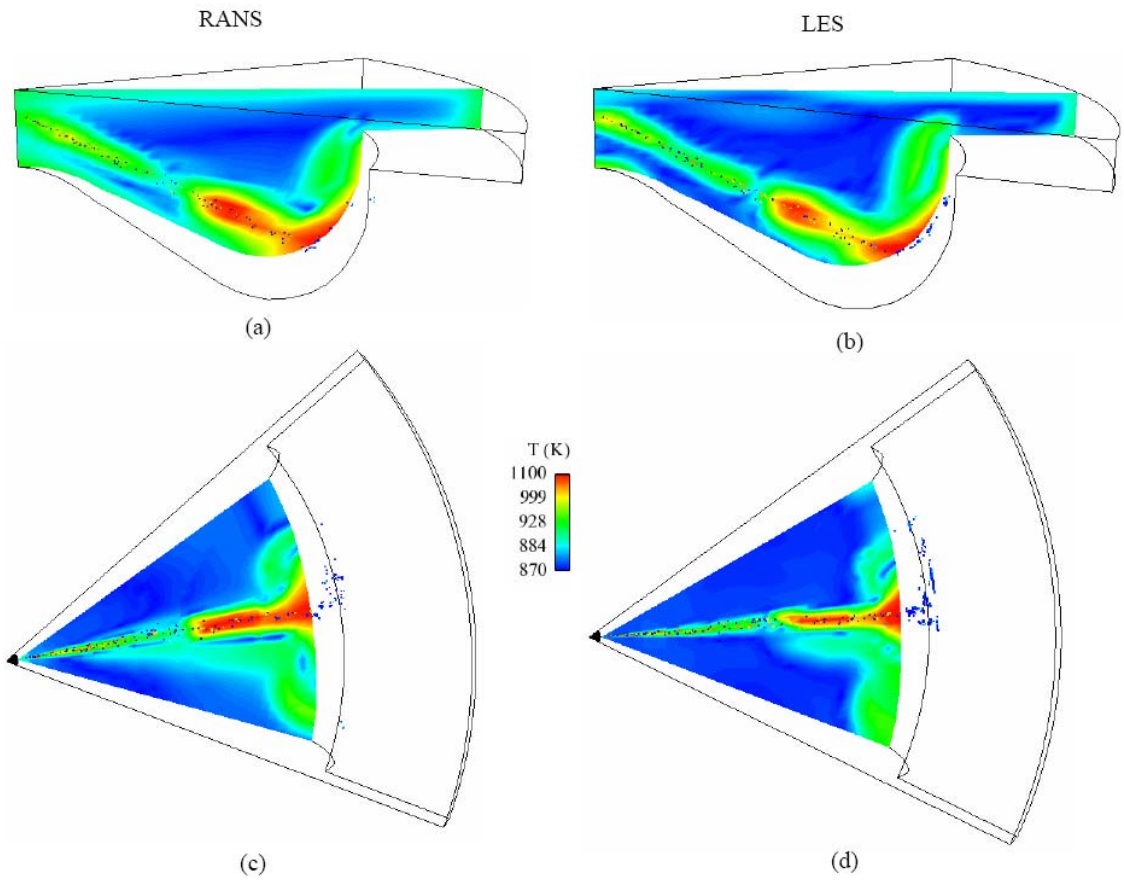

Figure 3.17. Spray and temperature distributions on cross sections through spray at –14 ATDC for SOI = –20 ATDC with 8% EGR.

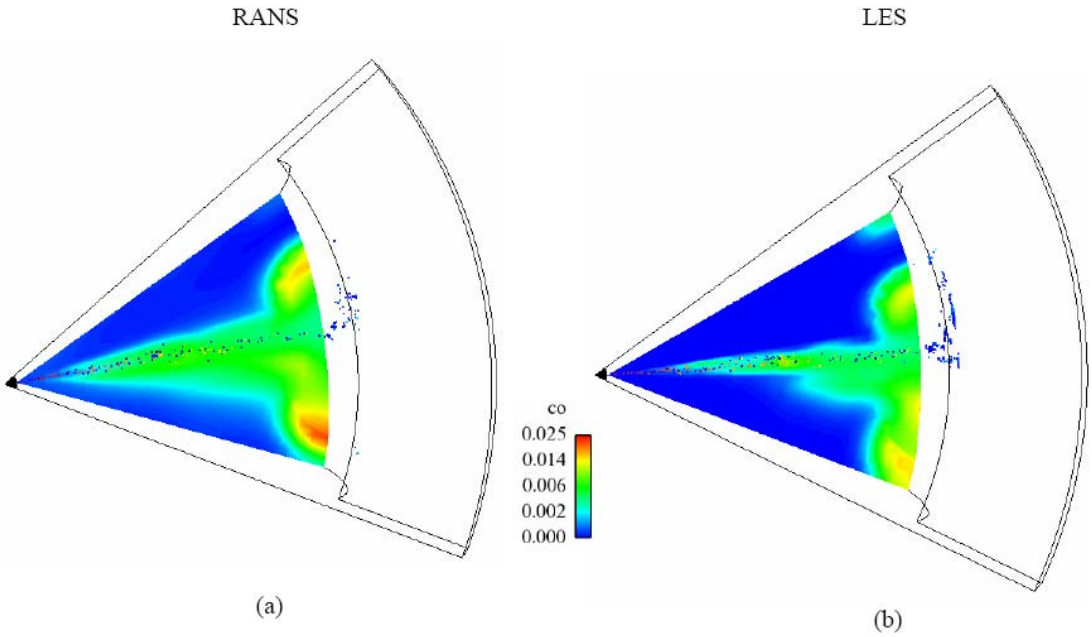

Figure 3.18. Distributions of CO mass fraction on a cross section through spray at –14 ATDC for SOI = –20 ATDC with 8% EGR.

The present models performed well in predicting the overall performance of the engine including the cylinder pressure history, heat release rate data, and soot and NO_x emissions trends with respect to injection timing and EGR levels. The present LES approach could also predict the unsteadiness and more detailed flow structures as compared to RANS models. Thus, the LES models can be further developed into an advanced engine simulation tool to address issues such as cycle-to-cycle variations and to capture performance variations due to the subtle change in engine operating conditions or geometrical designs.

4 GASOLINE SPRAY MODELING USING ADAPTIVE MESH REFINEMENT

4.1 Introduction

This chapter describes the development and implementation of parallel adaptive mesh refinement into KIVA-4 for gasoline spray modeling due to the capability of KIVA-4 to handle unstructured meshes. Adaptive mesh refinement (AMR) can be used to increase the grid resolution in the spray region to improve the spray simulation. This chapter will be arranged as follows. First, a procedure of performing local grid refinement and coarsening is presented, followed by the discussion of the modifications of hydrodynamic calculations to accommodate AMR in KIVA-4. Second, the issues of implementing parallel AMR into KIVA-4 and our strategies for addressing these issues are described. Third, both serial and parallel AMR will be validated by performing gasoline simulations on three different engine geometries. Finally, the AMR calculations in real engine geometries will be demonstrated.

4.2 Adaptive Mesh Refinement

It is known that the discrete Lagrangian particle method used in KIVA is grid dependent. Adaptive mesh refinement (AMR) was implemented into KIVA-4 to increase spatial resolution in the spray region to improve spray simulation. The standard KIVA-4 adopts a "staggered" approach for solving momentum equations. To simplify numerical schemes and the implementation procedure for AMR, this study adopted a "collocated" approach in which velocity was solved at the cell center for the momentum equations and used for the gas-liquid

coupling terms. A pressure correction method proposed by Rhie and Chow (Tsui and Pan, 2006) was used to address unphysical pressure oscillations due to the collocation of pressure and velocity (Ferziger and Peric, 2002). The current implementation determines data structure and numerical methods for AMR based on the features of the KIVA-4 solver. For instance, new child cells are attached to the existing cells. Cell edges from the higher-level cells are attached to the lower-level cells at the coarse-fine interface to calculate edge-centered values since the edge-looping algorithm is used to calculate diffusive fluxes, as will be described in the calculation of diffusive fluxes.

The current adaptation increases the grid density by splitting a cell into eight child cells. This method provides flexibilities in the mesh construction and is consistent with the characteristics of the finite volume solver with the arbitrarily unstructured mesh (Jasak and Gosman, 2000a). The adaptation starts with an initial coarse mesh (level 0) and creates new grids with higher levels (level l) continuously as the computation progresses. Meanwhile, the refined grids will be coarsened to the lower level grids if the fine grid is not needed in order to reduce the computational cost.

In this study, the adaptation is performed on a hexahedral mesh that is commonly used in engine simulations. The adaptation criteria are based on normalized fuel mass and fuel vapor gradients as will be described shortly. If a cell meets the criteria, it is tagged and will be divided into eight child cells as shown in **Figure 4.1** (a). If all the child cells of a parent cell meet the coarsening criteria, all the child cells of the parent cell are de-activated and the parent cell is restored. The detailed procedures are described as follows.

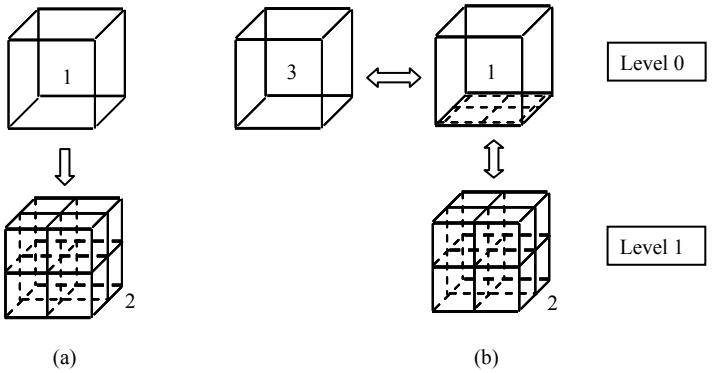

Figure 4.1. Schematic of local mesh refinement: (a) a parent cell is divided into eight child cells; (b) conventional face interface (1-3) and coarse-fine interface (1-2).

The refinement involves grid creation, connectivity setup, and property update. The procedure consists of the following steps.

(1) Insert new vertices on each edge, face, and cell by interpolation to create new sub-edges, sub-faces, and sub-cells;

(2) Establish relationship between the parent cell (level-$(l-1)$) and its direct child cells (level-l);

(3) Deactivate the parent cell, and update the connectivity;

(4) Re-associate spray particles from the parent cell to the corresponding child cells based on the shortest distance between a particle and the center locations of the child cells;

(5) Determine the cell-centered properties of the child cells using the linear variation with local conservation.

For instance, a generic variable Q_c defined on the cell center of a child cell can be obtained by the linear variation of the function within the parent cell as

$$Q_c = Q_p + \left(\boldsymbol{x_c} - \boldsymbol{x_p}\right)\bullet\left(\nabla Q\right)_p \tag{4.1}$$

where Q_p is the value at the parent cell, $\boldsymbol{x}_c, \boldsymbol{x}_p$ are the cell-center locations of the child cell and parent cell, respectively. $(\nabla Q)_p$ is the gradient evaluated on the parent cell using the least-squares method.

If all the child cells of a parent cell meet the coarsening criteria, all these child cells are de-activated and the parent cell is restored. The coarsening procedure consists of the following steps.

(1) Update the connectivity data;

(2) Re-associate spray particles in the child cells to their parent cell;

(3) Determine the properties of the parent cell from the child cells by volume average or mass average satisfying conservation laws.

The adaptation criterion uses a combination of "normalized fuel mass" and "vapor mass fraction gradients." The normalized fuel mass is the ratio of total mass (m_{l+v}) of liquid and vapor in a cell to total injected fuel mass (m_{inj}) as

$$r_m = \frac{m_{l+v}}{m_{inj}}. \tag{4.2}$$

Because a majority of the injected fuel is still in liquid form, this criterion can ensure the proper adaptation in the region near the injector nozzle. The vapor gradients are also chosen in order to provide adequate grid resolution outside the spray periphery where the vapor gradients are high. First derivatives (Wang and Chen, 2002) are used to calculate the indicator from the vapor gradients as,

$$\tau_{c,j} = \left| \left(\nabla Q \right)_{c,j} \right| \Delta l_j \tag{4.3}$$

where $\left(\nabla Q \right)_{c,j}$ is the cell-centered gradient component of the variable Q with respect to j coordinate and Δl_j is the cell size in j direction. Note that the repeated index does not imply Eisenstein summation. The following conditions are used for the grid adaptation.

- If $\tau_{c,j} > \alpha\tau$ in any coordinate direction j, or $r_m > r_{crit}$, cell c is flagged to be refined.
- If $\tau_{c,j} \le \beta\tau$ in all coordinate directions and $r_m \le r_{crit}$ for all the cells refined from the same parent cell, the related child cells will be coarsened.

α and β are the control parameters and in this study were taken to be 1.0 and 0.2 by preliminary tests, respectively, and $r_{crit} = 1.0 \times 10^{-5}$ was the critical value, which was found to be adequate. τ is the standard deviation calculated as

$$\tau = \left(\frac{1}{3N} \sum_{j=1}^{3} \sum_{c=1}^{N} \tau_{c,j}^2 \right)^{1/2} \tag{4.4}$$

where N is the total number of the active cells. In addition, the difference in the refinement levels at the cell interface is limited to one to ensure a smooth transition of AMR.

Engine simulations usually need to deal with moving boundaries such as moving pistons and valves. In the KIVA code, inner grid points are rezoned to preserve grid quality after each Lagrangian movement of the moving boundaries. The rezoning of general unstructured meshes can be accomplished by solving the Laplace equation. To avoid the difficulty of rezoning "hanging" nodes in the locally refined region, only the initial mesh (level 0) is

rezoned. The new locations of the refined cells can be determined by linear interpolation of the locations of the updated initial mesh.

The local refinement introduces the coarse-fine cell interface that complicates the numerical schemes for flux calculation. Fluxing schemes in the KIVA code must be modified to preserve the robustness and accuracy of the solver. The governing equations of the gas phase have been described in Chapter 2. For convenient reference, the same set of the governing equations is given here in integral forms with $k-\varepsilon$ turbulence model. The equations for conservation of mass for species m are

$$\frac{D}{Dt}\int_V \rho_m dV = \int_s \left[\rho D_c \nabla(\frac{\rho_m}{\rho}) \right] \bullet d\mathbf{A} + \int_V \dot{\rho}_m^c dV + \int_V \dot{\rho}_m^s \delta_{ml} dV \qquad (4.5)$$

where ρ_m, ρ are the density of species m and the total density, respectively, $\dot{\rho}_m^c, \dot{\rho}_m^s$ are the chemical and spray source terms, respectively, D_c is the gas diffusion coefficient, and δ_{ml} is the Dirac delta function in which subscript l corresponds to a liquid fuel in a multicomponent fuel injection. The equations for conservation of mass and momentum are

$$\frac{D}{Dt}\int_V \rho dV = \int_V \dot{\rho}^s dV \qquad (4.6)$$

and

$$\frac{D}{Dt}\int_V \rho \mathbf{u} dV = -\int_s \left[\frac{1}{a^2} p + A_0 \frac{2}{3} \rho k \right] d\mathbf{A} + \int_s \boldsymbol{\sigma} \bullet d\mathbf{A} + \int_V \mathbf{F}^s dV + \int_V \rho \mathbf{g} dV \qquad (4.7)$$

where $\mathbf{u}$ is the velocity vector, a is a pressure gradient scaling parameter for low Mach flow, p is the pressure, k is the turbulent kinetic energy, A_0 is a switch for turbulent or laminar

flow, $\boldsymbol{\sigma}$ is the viscous stress tensor, $\mathbf{F}^s$ is the spray momentum contribution to the gas phase, and $\mathbf{g}$ is the gravity vector. The energy equation is based on the specific internal energy as

$$\frac{D}{Dt}\int_V \rho I dV = \int_V -p\nabla\bullet\mathbf{u}dV + \int_V (1-A_0)\boldsymbol{\sigma}:\nabla\mathbf{u}dV + \int_s \left[K\nabla T + \rho D_c \sum_m h_m \nabla(\frac{\rho_m}{\rho}) \right]\bullet d\mathbf{A} + \int_V A_0 \rho\varepsilon dV + \int_V \dot{Q}^c dV + \int_V \dot{Q}^s dV \quad (4.8)$$

where I is the specific internal energy, K is the thermal conductivity, T is the temperature, h_m is the specific enthalpy, ε is the turbulent dissipation rate, and $\dot{Q}^c, \dot{Q}^s$ are the energy source terms from chemical reactions and spray, respectively. Turbulence is modeled by the $k-\varepsilon$ turbulence equations

$$\frac{D}{Dt}\int_V \rho k dV = -\int_V \frac{2}{3}\rho k\nabla\bullet\mathbf{u}dV + \int_V \boldsymbol{\sigma}:\nabla\mathbf{u}dV + \int_s \left[(\frac{\mu}{\mathrm{Pr}_k})\nabla k \right]\bullet d\mathbf{A} - \int_V \rho\varepsilon dV + \int_V \dot{W}^s dV \text{ , } (4.9)$$

$$\frac{D}{Dt}\int_V \rho\varepsilon dV = -\int_V C_{t1}\rho\varepsilon\nabla\bullet\mathbf{u}dV + \int_s \left[(\frac{\mu}{\mathrm{Pr}_\varepsilon})\nabla\varepsilon \right]\bullet d\mathbf{A} + \int_V \frac{\varepsilon}{k}\left[C_{t2}\boldsymbol{\sigma}:\nabla\mathbf{u} - c_{\varepsilon 2}\rho\varepsilon + c_s\dot{W}^s \right]dV \quad (4.10)$$

where μ is the viscosity coefficient, Pr_k and Pr_ε are the Prandtl numbers, $\dot{W}^s$ accounts for the rate of work done by turbulent eddies to disperse spray droplets, $c_\varepsilon, c_{\varepsilon 2}$ are the model constants, and C_{t1} and C_{t2} take on different forms for the standard $k-\varepsilon$ or the RNG (Renormalization Group) $k-\varepsilon$ models (Amsden et al., 1989; Torres and Trujillo, 2006).

Due to the use of AMR, the calculation of diffusive fluxes needs to be modified from its original algorithm to account for the coarse-fine mesh interface introduced by AMR. Terms bearing a format of $\int_s \nabla Q\bullet d\mathbf{A}$ in the gas phase equations are approximated by using the mid-point quadrature rule,

$$\int_s \nabla Q \bullet d\mathbf{A} \approx \sum_f (\nabla Q)_f \bullet \mathbf{A}_f \tag{4.11}$$

where subscript f represents a cell face. For a conventional face f in **Figure 4.2** (a), the term $(\nabla Q)_f \bullet \mathbf{A}_f$ is approximated by

$$(\nabla Q)_f \bullet \mathbf{A}_f = a_{c,cn}(Q_c - Q_{cn}) + a_{1,2}(Q_1 - Q_2) + a_{4,3}(Q_4 - Q_3) \tag{4.12}$$

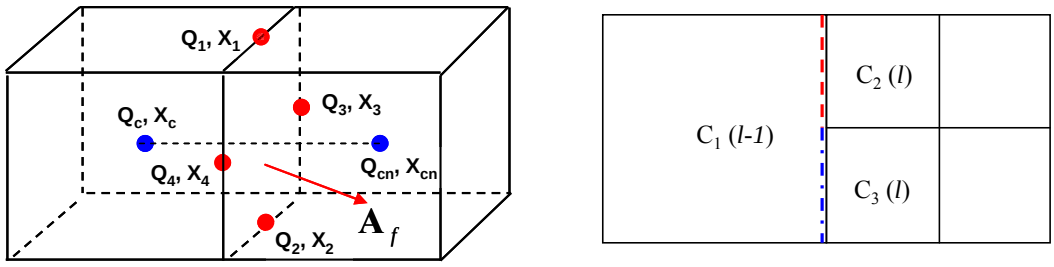

(a) Conventional interface (3-D)

(b) Coarse-fine interface (2-D)

Figure 4.2. Geometric arrangement of the gradient calculation at an interface f.

where Q_c, Q_{cn} are the cell-centered values of cell c and cell cn, Q_1, Q_2, Q_3, Q_4 are the edge-centered values of edges 1, 2, 3 and 4. The edge-centered values are obtained by averaging the cell-centered values of all cells that share the edge. $a_{c,cn}$, $a_{1,2}$, and $a_{4,3}$ are the geometric coefficients and determined by solving a system of 3×3 equation

$$a_{c,cn}(\mathbf{x}_c - \mathbf{x}_{cn}) + a_{1,2}(\mathbf{x}_1 - \mathbf{x}_2) + a_{4,3}(\mathbf{x}_4 - \mathbf{x}_3) = \mathbf{A}_f \tag{4.13}$$

where $\mathbf{x}_c, \mathbf{x}_{cn}$ are the cell centers on either side of the face f, $\mathbf{x}_1, \mathbf{x}_2, \mathbf{x}_3, \mathbf{x}_4$ are the edge centers of four edges bounding the face f, and $\mathbf{A}_f$ is the face area vector equal to $\mathbf{A}_f = A\hat{\mathbf{n}}$ where $\hat{\mathbf{n}}$ is the outward unit normal vector and A is the area of the face. At the coarse-fine interface, Eq. (4.11) is applied to the l-level child cells (cells c_2, c_3 in **Figure 4.2** (b)). When

calculating the edge-centered values Q_i (i.e., the dashed red edge in the cell c_2), the contribution from the $(l-1)$-level cell (i.e., the cell c_1) across the interface is achieved by attaching the edge to the $(l-1)$-level cell which is carried out in the refinement process. The term $\nabla Q \bullet \mathbf{A}$ for the face of the $(l-1)$-level cell becomes

$$(\nabla Q \bullet \mathbf{A})_{l-1} \approx -\sum_h (\nabla Q \bullet \mathbf{A})_{h,l} \tag{4.14}$$

where $(\nabla Q \bullet \mathbf{A})_{h,l}$ is the value for one of the l-level cells.

The viscous stress tensor term $\int_s \boldsymbol{\sigma} \bullet dA$ in the momentum equations is approximated by summing over all the cell faces

$$\int_s \boldsymbol{\sigma} \bullet dA \approx \sum_f \boldsymbol{\sigma}_f \bullet \mathbf{A}_f \tag{4.15}$$

where $\boldsymbol{\sigma}_f$ is the viscous stress tensor,

$$\boldsymbol{\sigma}_f = \mu_t \left[\nabla \mathbf{u} + (\nabla \mathbf{u})^T \right] - \tfrac{2}{3} \mu_t \nabla \bullet \mathbf{u} \mathbf{I} \tag{4.16}$$

with μ_t is the viscosity coefficient, superscript T indicates tensor transpose, and $\mathbf{I}$ is the unit tensor. One must find the value of $\boldsymbol{\sigma}_f$ and thus the velocity gradients $(\nabla u)_f$ at each cell face. For a velocity component u and a face f in **Figure 4.2** (a), the gradients ∇u satisfies the following condition

$$\mathbf{X} (\nabla u)^T = \boldsymbol{\Delta} \mathbf{u} \tag{4.17}$$

where the matrix $\mathbf{X}$ is defined by

$$\mathbf{X} = \begin{pmatrix} x_{ccn} & y_{ccn} & z_{ccn} \\ x_{12} & y_{12} & z_{12} \\ x_{43} & y_{43} & z_{43} \end{pmatrix}, \tag{4.18}$$

and the right-hand side vector $\mathbf{\Delta u}$ has

$$\mathbf{\Delta u} = \begin{pmatrix} u_c - u_{cn} \\ u_1 - u_2 \\ u_4 - u_3 \end{pmatrix}. \tag{4.19}$$

Then the components of the gradients ∇u in each coordinate direction can be determined as follows,

$$\begin{aligned} (\nabla u)_x &= \mathbf{i} \bullet \nabla u = \left(\mathbf{i} \bullet \mathbf{X}^{-1}\right) \mathbf{\Delta u} \\ (\nabla u)_y &= \mathbf{j} \bullet \nabla u = \left(\mathbf{j} \bullet \mathbf{X}^{-1}\right) \mathbf{\Delta u} \\ (\nabla u)_z &= \mathbf{k} \bullet \nabla u = \left(\mathbf{k} \bullet \mathbf{X}^{-1}\right) \mathbf{\Delta u} \end{aligned} \tag{4.20}$$

where $\mathbf{i}, \mathbf{j}, \mathbf{k}$ are the unit vectors in $x, y,$ and z coordinate directions, respectively. The terms $\mathbf{i} \bullet \mathbf{X}^{-1}$, $\mathbf{j} \bullet \mathbf{X}^{-1}$ and $\mathbf{k} \bullet \mathbf{X}^{-1}$ correspond to the 1st, 2nd and 3rd row of the matrix $\mathbf{X}^{-1}$, respectively, and can readily be obtained from Eq. (4.13). The gradients of other velocity components are calculated in a similar way. Then, the viscous diffusion term $\boldsymbol{\sigma}_f \bullet \mathbf{A}_f$ for the face of a l-level cell can be determined at the interface. For the face of the $(l-1)$-level cell across the interface, this term is obtained by summing the terms for all the l-level cells as

$$\left(\boldsymbol{\sigma}_f \bullet \mathbf{A}_f\right)_{l-1} \approx -\sum_h \left(\boldsymbol{\sigma}_f \bullet \mathbf{A}_f\right)_{h,l} \tag{4.21}$$

where h represents a l-level cell at the interface.

One also needs to calculate the viscous dissipation of the mean flow kinetic energy $\int_V \boldsymbol{\sigma} : \nabla \mathbf{u}\, dV$ since both tensors $\boldsymbol{\sigma}$ and $\nabla \mathbf{u}$ are evaluated at the cell center instead of the cell faces. Let u be a component of velocity $\mathbf{u}$. Then ∇u at the cell center is approximated as a cellwise constant using the divergence theorem as

$$\nabla u \approx \frac{1}{V}\int_V \nabla u dV = \frac{1}{V}\int_S u d\mathbf{A} \approx \frac{1}{V}\sum_f u_f \mathbf{A}_f \approx \frac{1}{V}\sum_f \tfrac{1}{2}\left(u_{c,l} + u_{c,l-1}\right)\mathbf{A}_f \qquad (4.22)$$

where u_f is the face center velocity, and $u_{c,l}$, $u_{c,l-1}$ are the cell-centered values at the levels l and $(l-1)$, respectively. At the coarse-fine interface, for an l-level cell, u_f is simply approximated by the average of the cell-center values $u_{c,l}$ and $u_{c,l-1}$. For the $(l-1)$-level cell across the interface, $u_{c,l}$ is the average of the cell-centered values of all the l-level cells sharing the interface. After the gradient terms are determined at the cell center, $\boldsymbol{\sigma}$ can be determined accordingly.

The collocation of pressure and velocity can cause parasitic pressure oscillations due to velocity-pressure decoupling (Ferziger and Peric, 2002). To reduce the oscillations, the Rhie-Chow pressure correction method (Tsui and Pan, 2006) is used when computing the face volume change for the pressure solution in the Lagrangian phase. Using this technique, the face volume change $(\mathbf{u}\bullet\mathbf{A})_f$ is modified by pressure gradients according to the following expression:

$$(\mathbf{u}\bullet\mathbf{A})_f^L = (\mathbf{u}\bullet\mathbf{A})_f^{L_o} - \frac{\Delta t}{\frac{1}{2}(\rho_c + \rho_{cn})}\left\{(\nabla p)_f - \tfrac{1}{2}\left[(\nabla p)_c + (\nabla p)_{cn}\right]\right\}\bullet\mathbf{A}_f \qquad (4.23)$$

where $(\mathbf{u}\bullet\mathbf{A})_f^{L_o}$ is calculated from the original face volume change equation that is derived from the momentum balance for control volume centered around the face f (Amsden et al., 1989; Torres and Trujillo, 2006). $(\nabla p)_c, (\nabla p)_{cn}$ are the cell pressure gradients and are calculated using the divergence theorem

$$\nabla p \approx \frac{1}{V}\int_V \nabla p dV = \frac{1}{V}\int_S p d\mathbf{A} \approx \frac{1}{V}\sum_f p_f \mathbf{A}_f \approx \frac{1}{V}\sum_f \tfrac{1}{2}\left(p_{c,l} + p_{cn,l-1}\right)\mathbf{A}_f \qquad (4.24)$$

where $p_{c,l}$ and $p_{cn,l-1}$ are the cell-centered velocities. $(\nabla p)_f$ is the pressure gradient at the cell face and is determined by using the method in Eq. (4.12). $p_{c,l}$ and $p_{cn,l-1}$ are determined in the same way as $u_{c,l}$, and $u_{c,l-1}$ in Eq. (4.22). The face volume change for the $(l-1)$-level cell across the interface is then summed over all the l-level cells on the other side of the interface as

$$\left(u\bullet\mathbf{A}\right)_{f_{l-1}}^{L} \approx -\sum_h \left(u\bullet\mathbf{A}\right)_{h,f_l}^{L} . \qquad (4.25)$$

The term $(\mathbf{u}\bullet\mathbf{A})_f^L$ is used to calculate the Lagrangian cell volume V^L that appears in the pressure iteration as

$$V^L = V^n + \Delta t \sum_f (\mathbf{u}\bullet\mathbf{A})_f^L \qquad (4.26)$$

where V^n is the cell volume at previous time step n and Δt is the main computational time step. The term $(\mathbf{u}\bullet\mathbf{A})_f^L$ will also be used to calculate convective face volume change when the face moves from the Lagrangian position to the final position corresponding to the new time step.

The calculation of convective fluxes also needs to consider the presence of the coarse-fine interface. In the transient engine simulation, after the mesh moves with the fluid in the Lagrangian phase, the mesh is rezoned to the new location which leads to the convective transport of the flow fields due to the relative movement of the mesh to the frozen fluid. The convective fluxes in the Eulerian phase are explicitly subcycled within the main computational time step to save computer time. The number of subcycles is determined by $n_{sc} = \Delta t / \Delta t_c$ where Δt is the main computational time step, Δt_c is the convective time step which satisfies the Courant condition and will be determined later. At each subcycle v, the face volume change δV_f associated with the cell face f is calculated by considering the total face volume change from the Lagrangian position to the final position after rezoning as

$$\delta V_{f_l} = \delta V_{f_l}^{n+1,n} \frac{\Delta t_c}{\Delta t} - \Delta t_c \left(\mathbf{u} \bullet \mathbf{A} \right)_{f_l}^{L} \tag{4.27}$$

where $\delta V_{f_l}^{n+1,n}$ is the total volume change of the face f of the l-level cell from the location at time n to the final location at time $n+1$. The $\delta V_{f_{l-1}}$ for the $(l-1)$-level cell at the interface is obtained by taking the negative of the sum of δV_{f_l} for the corresponding l-level cells. If δV_f is positive, the face movement leads to the cell volume expansion. If it is negative, the face movement leads to the cell volume compression.

The flux through a conventional face f into a cell c as shown in **Figure 4.3** (a) is calculated by

$$\left(\rho q V \right)_c^v = \left(\rho q V \right)_c^{v-1} + \left(\rho q \right)_f^{v-1} \delta V_{f_l} \tag{4.28}$$

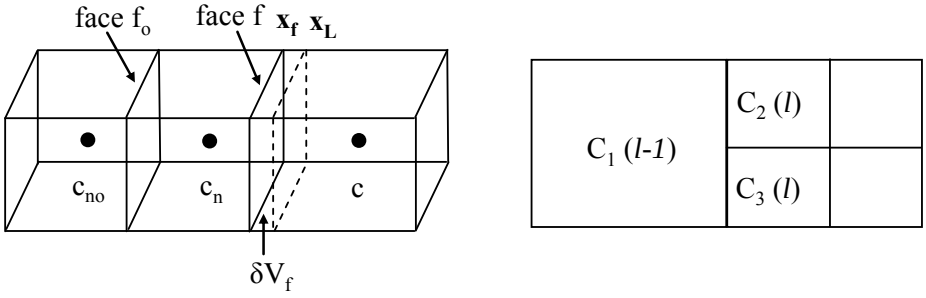

(a) Conventional interface (3-D) (b) Coarse-fine interface (2-D)

Figure 4.3. Computational stencil for gradient calculation.

where ρ is the density, V is the cell volume, and q represents the cell-centered quantity being evaluated such as velocity components, and specific internal energy. The quantity $(\rho q)_f$ at each subcycle is determined by using a quasi-second-order upwind (QSOU) scheme

$$(\rho q)_f = (\rho q)_{c_n} + \frac{d(\rho q)}{ds}\left|\mathbf{x}_f - \mathbf{x}_{c_n}\right|\left(1 - \frac{|\delta V_f|}{V_{c_n}}\right) \tag{4.29}$$

where $\frac{d(\rho q)}{ds}$ is the slopes in each cell computed by using a strong monotone upwind scheme modified from Van Leer's upwind scheme (Van Leer, 1979) as

$$\frac{d(\rho q)}{ds} = \text{sign}\left((\rho q)_c - (\rho q)_{c_n}\right)\min\left(\frac{\left|(\rho q)_c - (\rho q)_{c_n}\right|}{\left|\mathbf{x}_c - \mathbf{x}_{c_n}\right|}, \frac{\left|(\rho q)_{c_n} - (\rho q)_{c_{no}}\right|}{\left|\mathbf{x}_{c_n} - \mathbf{x}_{c_{no}}\right|}\right) \tag{4.30}$$

where $\mathbf{x}_c, \mathbf{x}_{c_n}, \mathbf{x}_{c_{no}}$ represent the cell-centered locations at the new time level while $\mathbf{x}_f$ is the face center. $\mathbf{x}_L$ is the Lagrangian position of the face. $\frac{d(\rho q)}{ds}$ is zero if $(\rho q)_c - (\rho q)_{c_n}$ and $(\rho q)_{c_n} - (\rho q)_{c_{no}}$ have different signs. For $\frac{d(\rho q)}{ds}$ of the $(l-1)$-level cell (i.e., c_1 in **Figure**

4.3 (b)), $(\rho q)_{c_n}$ and $\mathbf{x}_{c_n}$ are the average values of all the l-level cells (i.e., c_2 and c_3) on the other side. Only the faces from the l-level cells will be looped over to avoid a duplicate flux, and $\frac{d(\rho q)}{ds}$ will be determined for every face based on its associated volume change δV_f. Eq. (4.28) is then applied to the l-level cells. The flux for the $(l-1)$-level cell is given by

$$(\rho q V)^{\nu}_{f_{l-1}} = (\rho q V)^{\nu-1}_{f_{l-1}} - \sum_h (\rho q)^{\nu-1}_{f_{h,l}} \delta V_{f_{h,l}} \tag{4.31}$$

where $\sum_h$ means summation over all the l-level cells at the interface.

The new time step Δt^{n+1} is the minimum among an array of time step constraints (Amsden et al., 1989). Two constraints need to be re-evaluated on the refined cells resulting from AMR due to the coarse-fine interface and cell size change. First, the time step must be restricted to limit the cell distortion due to mesh movement in the Lagrangian phase. This constraint is enforced by a time step

$$\Delta t^n_{rst} = \min_c \frac{f_{rst}}{\frac{1}{3}|S_{ii}| + 2\sqrt{\frac{1}{9}\left[(S_{ii})^2 - 3\left(\varepsilon_{1ij}S_{2i}S_{3j} + \varepsilon_{i2j}S_{1i}S_{3j} + \varepsilon_{ij3}S_{1i}S_{2j}\right)\right]}}. \tag{4.32}$$

where f_{rst} is $1/\sqrt{3}$, S_{ij} is the rate of strain tensor, ε_{lij} is the alternating tensor, and the repeated indices imply Eisenstein summation. The gradient ∇u in the rate of strain tensor S_{ij} is calculated using Eq. (4.22). Second, the convection time step must reflect the cell size change resulting from the refinement/coarsening. The convection time step is limited by

$$\Delta t^n_c \le C_c \Delta t^{n-1}_c \min_f \frac{V}{|\delta V_f|} \tag{4.33}$$

where C_c is a constant 0.2, V is the cell volume, Δt_c^{n-1} is the previous time step, and δV_f is the face volume change. Unfortunately, δV_f is not available for the newly refined cells using AMR since this term is calculated in the rezoning stage whereas Eq. (4.33) is calculated at the beginning of each computational cycle. For newly refined cells, Δt_c^n can be approximated by using geometrical relationships. For a child cell, its volume is approximately one-eighth of its parent's volume, and its face volume change is approximately one-fourth of that of its parent cell. The convection timestep of each child cell can be taken as half of the timestep for the parent cell. During the cell coarsening, the face volume change δV_f for the re-activated parent cell can be approximated from its child cells. Then Eq. (4.33) can be directly applied.

4.3 Parallelization

Parallelization of KIVA-4 was performed using the Message Passing Interface (MPI) library for use in distributed memory machines. Before a parallel computation starts, a computational mesh (domain) must be decomposed into all processors. Domain decomposition influences work load balance, communication overhead, and thus overall parallel performance. In engine simulation, domain decomposition is complicated by two major factors. First, cells and nodes can become de-activated and/or activated during the calculation. For instance, the entire port can be re-activated or de-activated after a valve is opened or closed. Piston motion also causes layers of cells to be de-activated or re-activated. These transient features can cause the initially balanced workload to become unbalanced.

Second, the modeling of spray particles can also cause the imbalance of workload and communication overhead. If the spray particle is directly associated with the processor that owns the cell where the spray particle is located, the parallel implementation can be simplified but the workload may not be balanced. On the other hand, if the particles are distributed equally among processors, the implementation will become difficult and the communication overhead will be increased.

The work on parallelizing KIVA-4 was a collaborative effort with Los Alamos National Laboratory (LANL) (Li et al., 2008; Torres et al., 2009). The current study particularly contributed to the parallelization and performance for complex engine geometries. The focus of the work presented in this report is on parallelizing AMR for transient engine spray simulation (Li and Kong, 2009a).

To preserve the load balance, it is important to partition the domain such that each processor has the same number of active cells. The current strategy is a static partitioning in which an equal number of parent cells are assigned to each processor and used throughout the calculation. For spray particles, to minimize communication overhead, the current implementation is to associate each spray particle with the processor that owns the cell within which the spray particle resides. Child cells are tied to the spray particles. Once the parent cells are partitioned, the child cells are assigned to the same processor as their parent cell. The partitioning of the parent cells is accomplished by using a constrained form of mesh partitioning in **METIS** (Karypis and Kumar, 1998a). **METIS** is a software package for

partitioning unstructured graphs, partitioning meshes, and computing fill-reducing ordering of sparse matrices.

In the current partitioning, an unstructured mesh is first converted into a graph in which all cells become vertices and the faces between the cells become edges. The edges in the graph can be assigned weights to form different partitions. In reciprocating engines, a computational domain experiences periodic compression and expansion in a vertical direction. In order to obtain a balanced computational load, a mesh is generally grouped vertically into different processors. This can be achieved by assigning large weights to vertically linked edges in the graph format. **Figure 4.4** shows an example of the domain divisions of three geometries for computations using four processors using the vertical partition strategy only. These geometries are relatively simple, in particular, without port deactivation and re-activation. For engine geometry with port de-activation/re-activation, a single strategy of vertically partitioning the domain may assign processors a disproportional number of cells from the port region which will cause load imbalances. This can partially be addressed by partitioning different portions of the domain separately based on a hypergraph partition in the **hMETIS** software package (Karypis and Kumar, 1998b). This second strategy still needs to combine with a dynamic repartitioning strategy to obtain a balanced load in the whole computational cycle (Torres et al., 2009).

A parallel computation consists of the following steps. First, domain partitioning assigns each processor a subset of the total cells in the mesh. A processor owns all cells that are assigned to it and all nodes that constitute the cells. Therefore, a node can be owned by

multiple processors. Then, each processor solves the hydrodynamic equations on its set of cells. Cells and nodes around the processor boundary need the information of their neighbors that are owned by other processors. However, different processors usually do not share the memory in a distributed-memory computer cluster. Thus, information on cells and nodes around the processor boundary needs to be built and exchanged during the calculation in order to solve the equations correctly. Therefore, it is necessary to establish neighboring cells and nodes of each processor so that the information can be exchanged between processors, which is established in a so-called communication initialization.

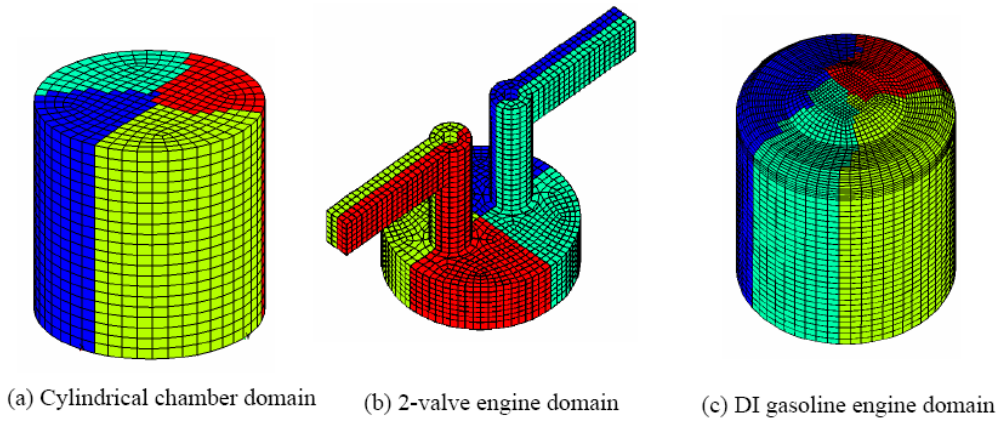

Figure 4.4. Domain partition for four processors using METIS.

Communication initialization includes assigning cells and nodes and their associated properties to each processor, establishing neighboring cells and nodes, and constructing the communication arrays. This initialization is completed before the hydrodynamic calculation begins. Data exchange is performed during the hydrodynamic calculations by calling different communication subroutines which will be described shortly. The assignment of

cells and nodes to each processor can be readily accomplished based on the partition file from the domain decomposition.

The neighboring cells of a processor are defined as the cells that do not belong to the processor but touch any of the nodes that belong to it. Similarly, the neighboring nodes of a processor are defined as the nodes of the neighboring cells of the processor but exclude those nodes that are owned by the processor itself. In the code, the neighboring cells are used to exchange cell-based properties and face properties during the calculation. The neighboring nodes are used to exchange coordinates and velocities of the nodes. The information on the neighboring cells and nodes, which usually includes lists of cells and nodes that need to be sent to and received from neighboring processors, are saved in the communication arrays.

Different communication subroutines are developed to exchange different types of data in the neighboring cells and nodes for reduced communication cost. For instance, in the present code, subroutine *communicate* is designed to communicate floating point cell-based properties. Subroutine *communicatei* is designed to communicate integer cell-based properties. Subroutine *communicatev* is designed to communicate floating point node-based properties. Subroutine *communicatederivativese* is designed to communicate derivates of cell-based properties at a face interface that lies on the processor boundary. This subroutine is called to exchange the derivatives during the convection calculations. Subroutine *communicatespd* is designed to communicate cell-based species densities. The construction of these subroutines will enhance the efficiency of code implementation as well as parallel performance by reducing the searching cost.

AMR is performed after the initial communication setup. The communication re-initialization is required due to the changes of cells, nodes, connectivity, and properties. Newly created child cells and nodes are simply assigned to the same processor as their parent cells as mentioned above. To reduce the re-initialization cost, however, the process of finding neighboring cells and nodes and constructing the communication arrays requires special attention, as will be described in the following.

Due to the hanging node structure on the local mesh interface (**Figure 4.1** (b)), it is necessary to loop through both parent cells and child cells to find the neighboring cells and nodes at each re-initialization. The search cost can be reduced by considering the cells and nodes on the processor boundaries only. The efficiency can be further improved if the neighbors do not need to be re-searched when a new refinement does not occur on any of the processor boundaries. One can also refine all the cells on the processor boundaries at first AMR so that the neighbors can be set up one time only. However, this strategy may increase unnecessary communication and can cause more communication overhead.

The communication arrays depend upon both the total numbers of cells and nodes owned by each processor and the numbers of its neighboring cells and nodes. The arrays can stay unchanged if AMR is merely an activity of cell coarsening and/or re-activation of the de-activated child cells in which both the cells and nodes owned by each processor and its neighboring cells and nodes do not change. However, only the local addresses of the

neighbors in the arrays need to be updated if a new refinement does not occur on any of the processor boundaries in which the numbers of the neighboring cells and nodes do not change.

In fact, the communication re-initialization is generally costly in computer time if it is performed frequently. Therefore, the strategy is to restrict the frequency of performing AMR, e.g., every 10 computational timesteps. The solution accuracy was sacrificed slightly to obtain better parallel performance. This strategy may be carefully tuned to obtain a good trade-off between accuracy and speed-up. Other potential strategies have been considered for future implementations such as repartitioning the cells to obtain a better load balancing among processors at each adaptation timestep. Furthermore, parallel AMR may be improved by executing the mesh refinement/coarsening on each involved processor instead of executing it on root process only, as is the case in the current implementation.

4.4 Gasoline Spray Simulation Using AMR

The baseline code used in this part of work is parallel KIVA-4. Fuel spray atomization was simulated using the Taylor Analogy Breakup (TAB) model (O'Rourke and Amsden, 1987) that was available in KIVA-4. The TAB model is known to predict gasoline spray breakup reasonably well. KH-RT models along with a nozzle flow model were also implemented into the parallel KIVA4 for modeling diesel spray atomization. Simulations using the KH-RT models and AMR were performed and validated in later work (Kolakaluri et al., 2009). Other spray sub-models included the models for collision, turbulence dispersion, vaporization, and wall film to account for related phenomena. Combustion was not

considered here. The standard $k-\varepsilon$ model was used to model the effects of turbulence on mean flow and spray. The law-of-the-wall boundary conditions were used to treat turbulence and heat transfer near walls. The fixed temperature condition was used for wall temperature. The initial spray conditions were determined from the injector geometry and injection conditions. The serial AMR implementation was first validated followed by the validation of parallel AMR. Then the parallel performance was tested on a number of engine geometries.

Verification of AMR implementation

The present AMR method was applied to simulate gasoline sprays (Li and Kong, 2009b). The engine had a cylindrical combustion chamber with the bore and stroke equal to 10 cm and 10 cm, respectively. The engine speed was 4,000 rev/min. The spray was injected at a constant rate of 135 m/s into the chamber from the center of the cylinder head. The initial drop diameter was 200 microns and the initial drop temperature was 301 K. The fuel was iso-octane and the total injected fuel was 3.6 mg. The ambient was air with an initial temperature of 301 K and pressure of 1 bar. The initial meshes were based on the Cartesian O-grid type mesh. The simulation started from 180 ATDC when the piston started to move upward, and the fuel was injected also at 180 ATDC for a duration of 30 crank angle degrees.

It is expected that a coarse mesh using AMR should give the same results as the uniformly fine mesh but with reduced computer time. Therefore, results using the uniformly fine mesh will serve as the baseline for AMR verification. Notice that “coarse” and “fine” are only relative terms for describing the mesh density. The coarsest mesh size was 5 mm. To meet the large void fraction condition of the Lagrangian method, AMR was performed up to 2

levels in this study. Thus, the comparable finest mesh size was 1.25 mm on average. Simulations were performed for the following mesh conditions: 5 mm, 2.5 mm, 1.25 mm, 5 mm with one-level refinement (5mm+L1), and 5 mm with two-level refinement (5mm+L2).

Due to the stochastic nature of spray modeling, comparisons using representative statistical data of spray would not be feasible. Therefore, the liquid and vapor penetrations, vapor mass fraction, and spray structure were chosen as parameters for comparison. The liquid penetration was defined as the distance from the nozzle orifice to a position which corresponds to 95% of the integrated amount of liquid drops from the nozzle orifice. The vapor penetration was the axial distance from the nozzle orifice to a position with the vapor mass fraction greater than 0.01.

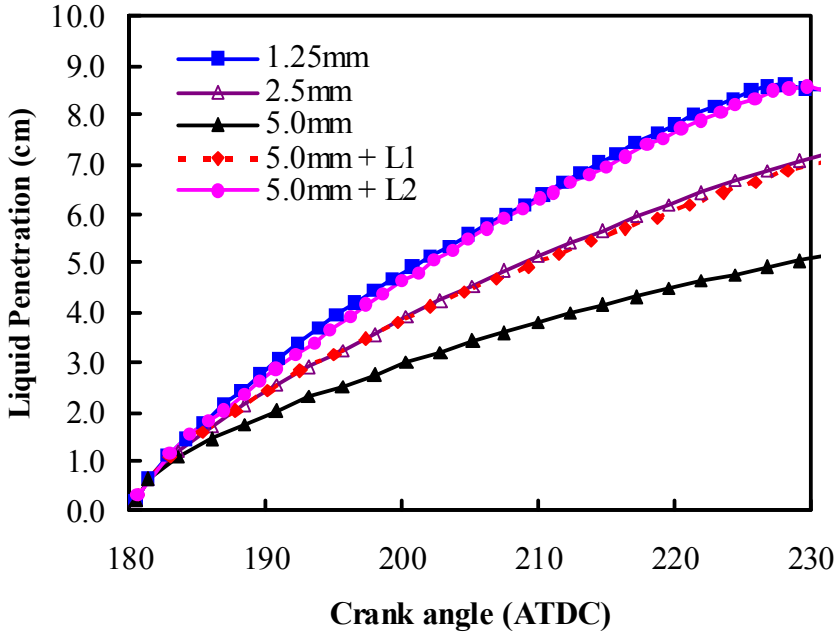

(a) Liquid penetration (cm)

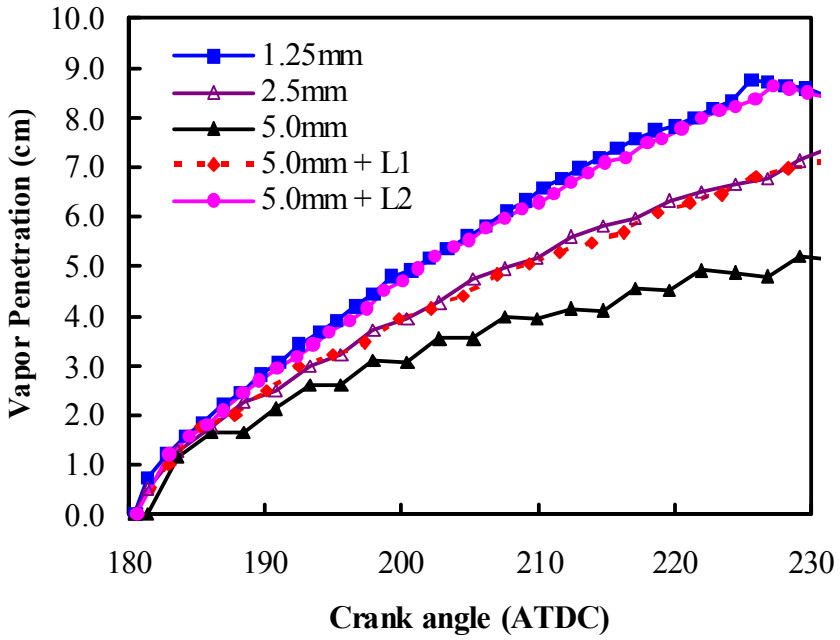

(b) Vapor penetration (cm)

Figure 4.5. Comparison of liquid and vapor penetrations using different meshes with respective refinement levels.

Table 4.1. Comparison of the computer time for different mesh sizes.

mesh size Δx	1.25 mm	2.5mm	5.0mm	5.0mm+L1	5.0mm+L2
Time (min)	4770.9	311.3	15.4	88.5	467.2
% (based on the 1.25 mm mesh case)	100.0	6.52	0.32	1.85	9.79

Figure 4.5 shows the comparisons of liquid and vapor penetrations for the five cases studied. The 5mm+L1 case produced similar penetrations to those using 2.5 mm mesh size. The 5mm+L2 case produced comparable penetrations to those using 1.25 mm mesh size. It can be seen that the case using 5 mm mesh size without AMR produced the shortest penetrations. As the mesh density increased, so were the penetrations because the increased grid resolution

improved the prediction in momentum exchange from the spray to the gas phase resulting in smaller relative velocities and thus longer penetrations, as can be seen from the maximum gas velocity prediction in **Figure 4.6**. **Table 4.1** shows the comparisons of computer times for the cases studied for computations from 180 to 360 ATDC (i.e., piston at top-dead-center). It is seen that the time saving for both level 1 and level 2 refinements are significant compared to the equivalent fine mesh cases for the same level of solution accuracy. This time saving can be justified by total active cell numbers that participated in computations in each mesh case as shown in **Figure 4.7**. The total active cell numbers in the 5mm+L1 case amounted to only 28% of the active cells using 2.5 mm mesh size at the early stage of the calculations and only to 50% of those by the end of the calculations. There were much fewer active cells participating in computation in the 5mm+L2 case compared to the 1.25 mm case.

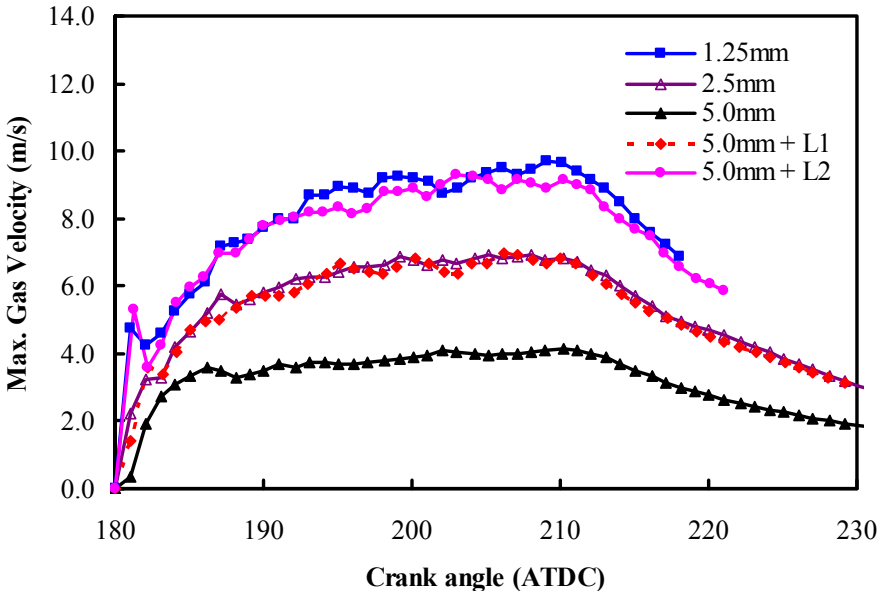

Figure 4.6. Comparison of the maximum gas velocity for different mesh refinement conditions.

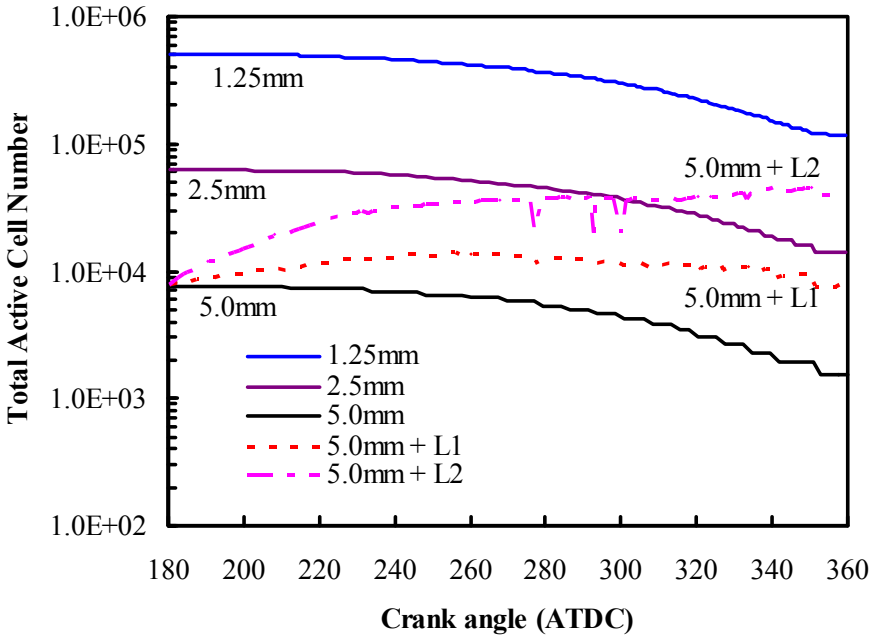

Figure 4.7. Total active cell numbers as a function of crank angle for different mesh refinement conditions.

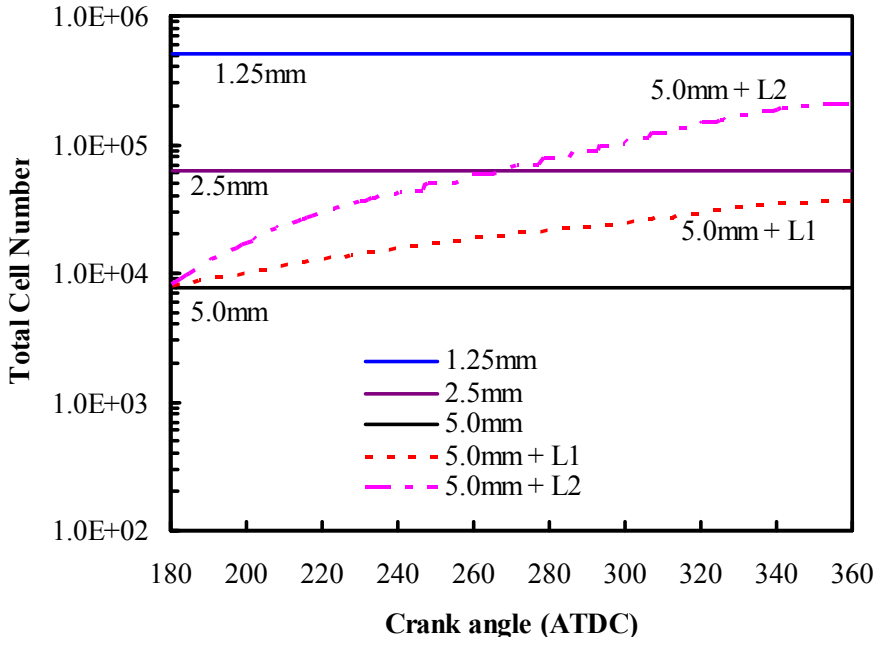

Figure 4.8. Total cell numbers as a function of crank angle for different mesh refinement conditions.

The fluctuations seen on the curves were results of the cell de-activation due to the snapping procedure that was used to de-active or re-active a layer of cells to preserve grid quality when a computational domain was compressed or expanded. **Figure 4.8** shows the total cells (active plus inactive) for the different mesh sizes. It can still be seen that the AMR cases entailed significantly fewer cells compared to the equivalent fine mesh cases.

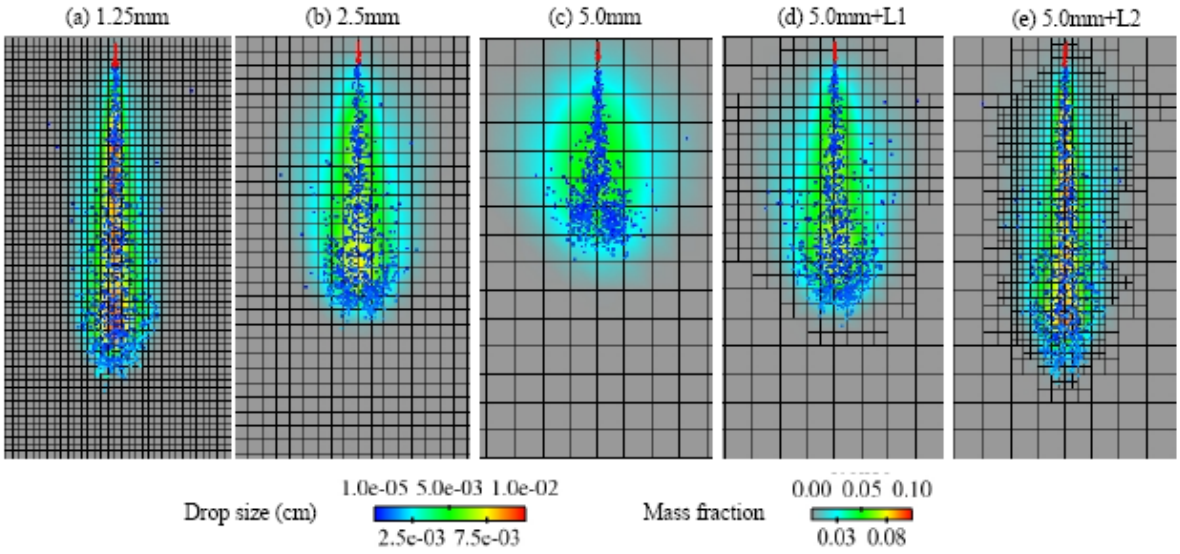

Figure 4.9. Comparison of the spray pattern and fuel vapor on a cutplane along the spray axis at 205 ATDC.

Figure 4.9 shows the fuel vapor distribution and spray pattern for the five cases on a cutplane along the spray axis at 205 ATDC with all the drops projected onto the cutplane. Similar fuel vapor distributions can be observed between the "5mm+L1" case and the "2.5 mm" case. The same is true for the results between the "5mm+L2" case and the "1.25 mm" case. In the "5.0 mm" case, fuel vapor was distributed in a wider region than in other cases due to over-estimated diffusion resulting from the coarse grid size. Due to the insufficient spatial resolution, the "5.0 mm" case produced the so-called "clover leaf" artifact (**Figure**

4.10 (c) bottom) (Schmidt and Rutland, 2000; Hieber, 2001). The artifact is a result of drop collisions that move the new drops towards the cell centers around the injector since the drops moving 90° apart in the same cell tended to move towards the cell center due to the large relative velocities between the drops. AMR refined all the cells around the injector and thus distributed drops into more cells, alleviated this artifact, and produced the pattern similar to that using the fine mesh as seen in **Figure 4.10** (a,b,d,e).

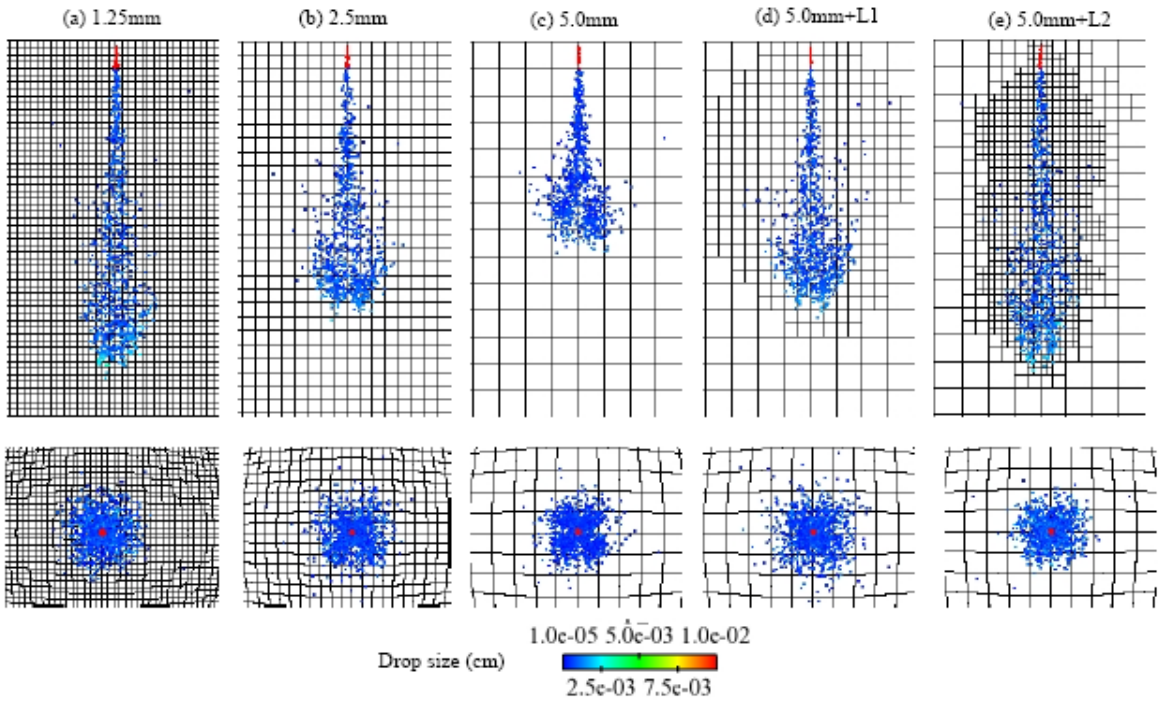

Figure 4.10. Comparison of the spray pattern on a cutplane along the spray axis (top) and at 3.0 cm above the piston surface (bottom) at 205 ATDC.

It can be seen that the spray simulation is dependent on the base mesh if AMR is not used. To further demonstrate the benefits of using AMR, simulations were performed in the same domain by injecting spray at a 40° angle from the vertical axis. The ambient pressure was 3 bars. Simulations were performed on the 1.25 mm, 5.0 mm, and 5.0mm+L2 refinement.

Figure 4.11 shows the comparisons of spray structure and vapor contour at 1 ms after injection. The coarse mesh without AMR (5.0 mm) predicted a shorter penetration and higher vapor diffusion than those using the fine mesh or the coarse mesh with AMR. It is also seen that the coarse mesh without AMR predicted asymmetric shear stresses on the top and bottom of the spray tip causing an asymmetric spray structure. The results using the L2 refinement are comparable to those using the 1.25 mm mesh.

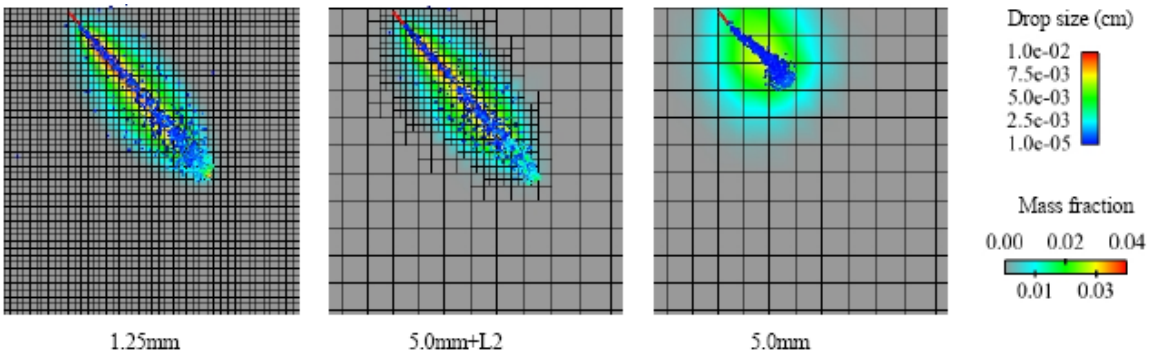

Figure 4.11. Comparison of the spray pattern and fuel vapor for injection with a slanted angle.

The above comparisons indicate that the AMR method can produce comparable results to those using the fine mesh but with much less computer time (less than 10% of the time for the fine mesh). In particular, AMR refined all cells that contained large drops or have high vapor gradients. AMR can also effectively alleviate the "clover leaf" artifact and other artifacts in the Cartesian mesh.

Verification of parallel AMR implementation

Three engine geometries were used to verify and evaluate the parallel AMR implementation (Li and Kong, 2009b). The simulation conditions are listed in Table 4.2 for these three

geometries including a cylindrical chamber, a 2-valve model, and a DI gasoline engine. To test the effects of the spray on the load balance and communication overhead, both one jet and six jets were simulated. Two types of meshes (coarse and fine) were used to evaluate the effect of mesh size on the parallel performance. Cell numbers listed in Table 4.2 were the

Table 4.2. Simulation Conditions.

Engine / Model	Cylindrical chamber	2-valve engine	DI Gasoline engine
Bore (cm)	10	14	5
Stroke (cm)	10	10	10
Piston and dome	Flat	Flat	Complex shapes
Cell numbers (coarse)	15,225	16,000	55,950
Cell numbers (fine)	124,200	128,000	193,500
Fuel	Gasoline	Gasoline	Gasoline
Number of nozzle holes	1 or 6	1 or 6	1 or 6
Start of injection (ATDC)	180	360	300
Injection duration (CAD)	30	10	40
Injection velocity (m/s)	135		
# of comp. parcels	2000		
Injection rate	constant		
Initial droplet size	100 micron	430 micron	236 micron
Initial droplet temp. (K)	301	331	301
Initial gas temp. (K)	300	800	300
Initial gas pressure (bar)	1	6	1
Engine speed (rpm)	4,000	1,000	1,500
Simulation duration (ATDC)	180 – 360	0 – 450	270 – 360

numbers of the total cells when the piston was at its bottom-dead-center position. The geometries of the three different engines are shown in **Figure 4.4**. The parallel implementation was verified by comparing the predicted results with and without parallel computing. Since the stochastic particle technique was used for modeling the spray dynamics

and the numbers of parcels from processor to processor were not generally the same, the resulting sets of random numbers associated with the parcels were not the same among processors. As a result, the spray distribution may not be identical in a parallel run to that in a serial run. Nonetheless, the comparisons of spray patterns are informative in assessing the validity of the present implementation.

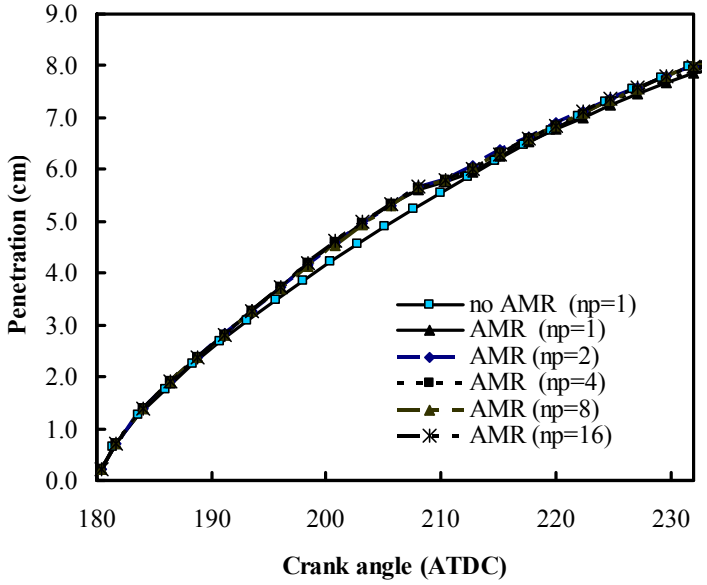

Figure 4.12. Comparison of liquid penetrations for different numbers of processors.

Figure 4.12 shows the comparison of spray penetrations predicted by using different numbers of processors for the cylindrical chamber with the grid size of 4 mm for AMR cases. Results using 2 mm grid size without AMR are also shown for comparison. Only slight differences in the penetration are seen among the different cases. Hence, it can be seen that the parallel AMR can achieve the same level of accuracy as in the serial run. The spray patterns at crank angle 205 ATDC are shown in **Figure 4.13** that includes the mesh on the central cutplane with all the drops in the plot. The slight differences in the spray patterns

among processors are thought to be due to the different sets of random numbers generated from each processor as mentioned earlier. In fact, similar differences in spray patterns were observed when simulations were performed using different numbers of processors without using AMR (not shown here). Therefore, it can be seen that the parallel AMR was implemented correctly.

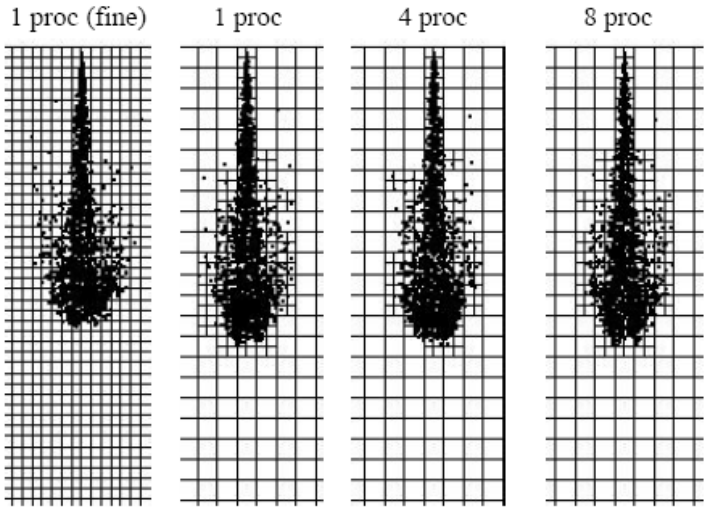

Figure 4.13. Comparison of spray patterns at crank angle 205 ATDC using different numbers of processors together with DAMR.

Figure 4.14 and **Figure 4.15** show the comparisons in penetrations and spray patterns when the 10 time-step control strategy was applied. It is seen that the penetrations are reasonably close to the results that used the fine mesh without AMR. The same tests were also performed on the other two geometries (i.e., 2-valve engine and DI gasoline engine) and similar results were found. For brevity those results are not presented here.

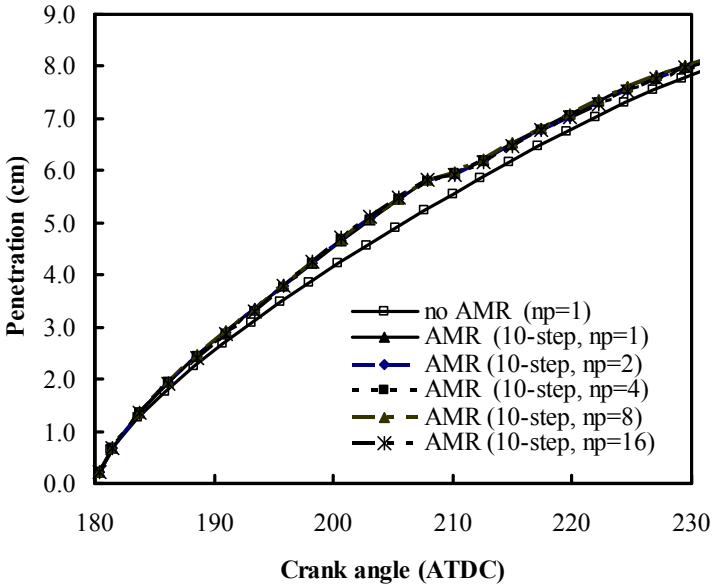

Figure 4.14. Liquid penetration comparison with the 10 timestep control strategy.

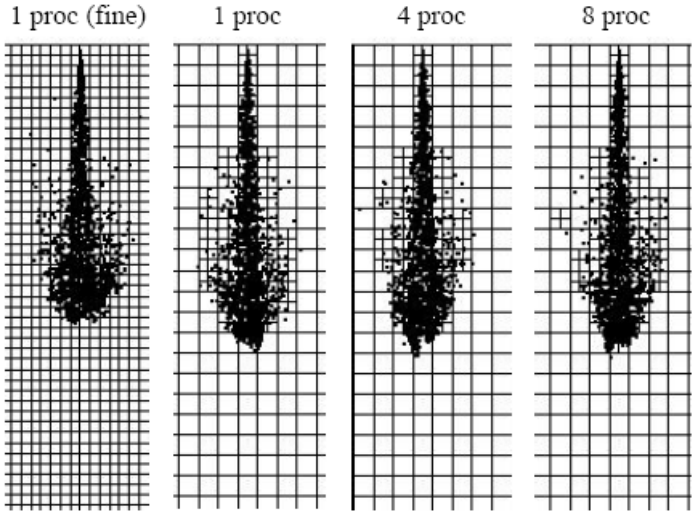

Figure 4.15. Spray pattern comparison between the baseline serial run and parallel runs with the 10-timestep control strategy.

Figure 4.16 shows the comparisons of the predicted spray structure with six jets using one processor and four processors. The start of injection was 180 ATDC and the results shown were at 310 ATDC. The top two pictures show the grids and fuel vapor contours on a cut-

plane together with all the fuel drops in the chamber. It is an artifact due to post-processing that some drops appear to be out of bounds. The bottom two pictures show the spray structures colored by the drop sizes. This geometry has irregular cells in the dome region

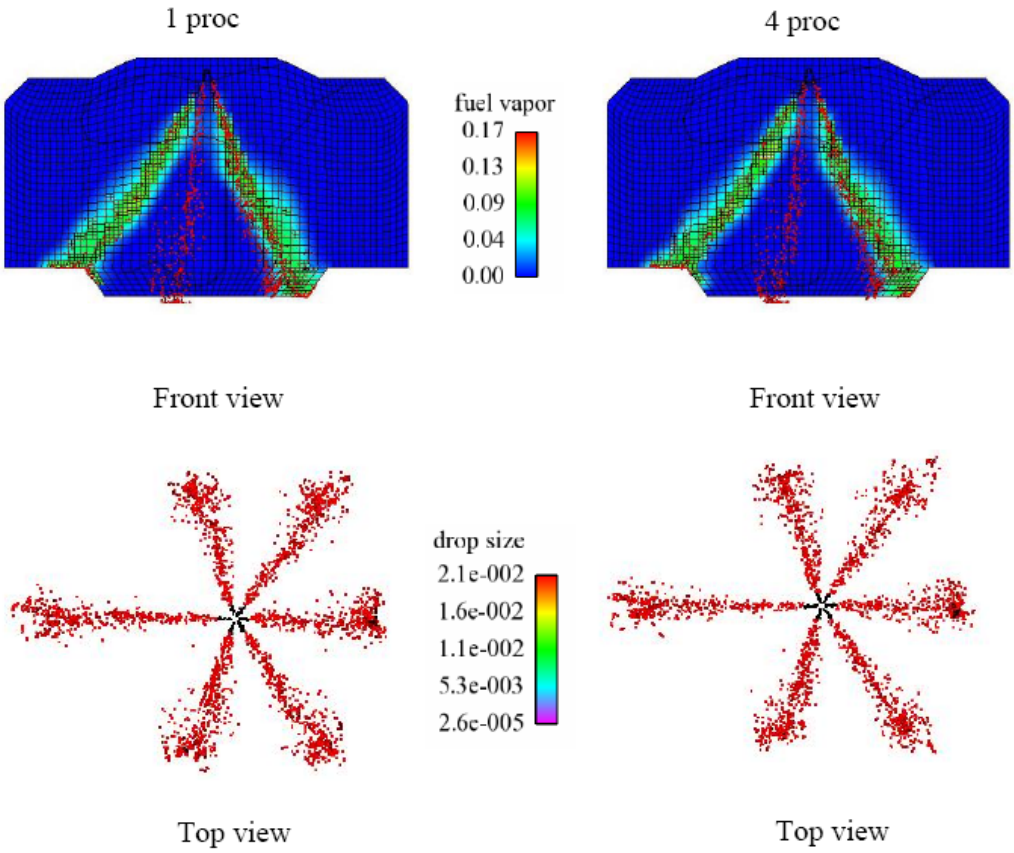

Figure 4.16. Spray pattern comparisons in the DI gasoline engine combustion chamber at crank angle 310 ATDC. Note that the start of injection was 180 ATDC.

which leads to distorted cells in the squish region on the perimeter of the cylinder during rezoning. Thus, a rezoning algorithm was implemented to alleviate the distortion of cells near the squish perimeter. This algorithm requires 10 times more iterations and needs to communicate neighboring cells during each iteration in a parallel run. Therefore, a parallel run needs additional communication cost compared to a serial run when rezoning takes place.

Nevertheless, the results demonstrated that the present parallel implementation performed properly for this geometry.

Since the goal of parallel computing was to reduce the elapsed time, the performance of the parallel AMR was assessed by the speed-up and computational efficiency. The effects of load imbalance and communication overhead can be assessed by comparing the speed-up and efficiency. Furthermore, the cases with single-hole nozzle and 6-hole nozzle were designed to test the effects of child cells on the load imbalance and communication overhead.

The speed-up S is defined as

$$S = \frac{T_1}{T_N} \tag{4.34}$$

where T_1, T_N are the elapsed times of simulations by using 1 processor and N processors, respectively. Ideally, the speed-up should scale linearly with the number of processors. In reality, due to communication overhead and other factors, S is always lower than N and is mostly dictated by the slowest processor. The computational efficiency E is defined as the speed-up relative to the number of processors,

$$E = \frac{S}{N} = \frac{T_1}{NT_N} \tag{4.35}$$

and indicates how effectively on average a processor is used for computing.

For the single-hole injection cases using AMR, **Figure 4.17** shows the speed-up and computational efficiency for the three geometries. The coarse meshes (see Table 4.2, and the

grid size is 4 mm for the cylindrical domain) were used. The speed-up was reasonable given that the mesh sizes were relatively coarse and no combustion was involved. The DI gasoline

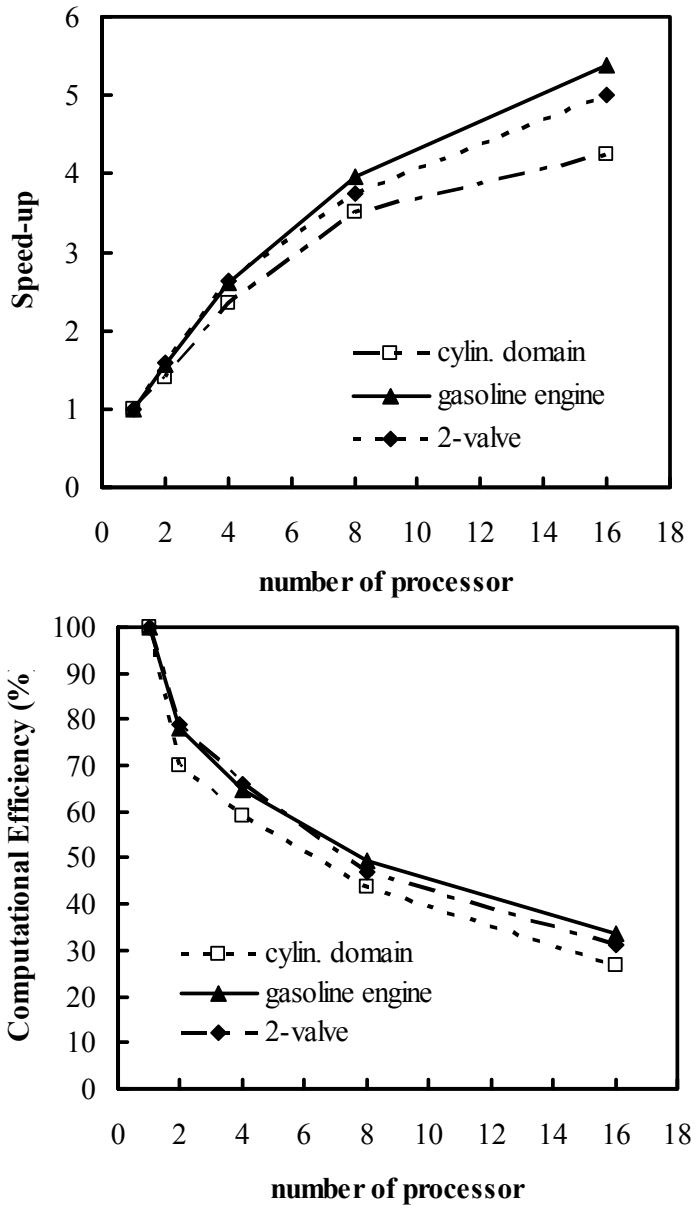

Figure 4.17. Speed-up and computational efficiency of the three geometries for single-hole injection using the coarse mesh.

engine geometry case had the best speed-up partially because this geometry had the largest number of grid points compared to the other two geometries. The computational efficiency

decreases as the number of processors increased due in part to the quality of partitioning with regard to AMR and snapping. The decrease in efficiency beyond four processors was also seen in the implementation by Bella et al. (2006) for computations without AMR.

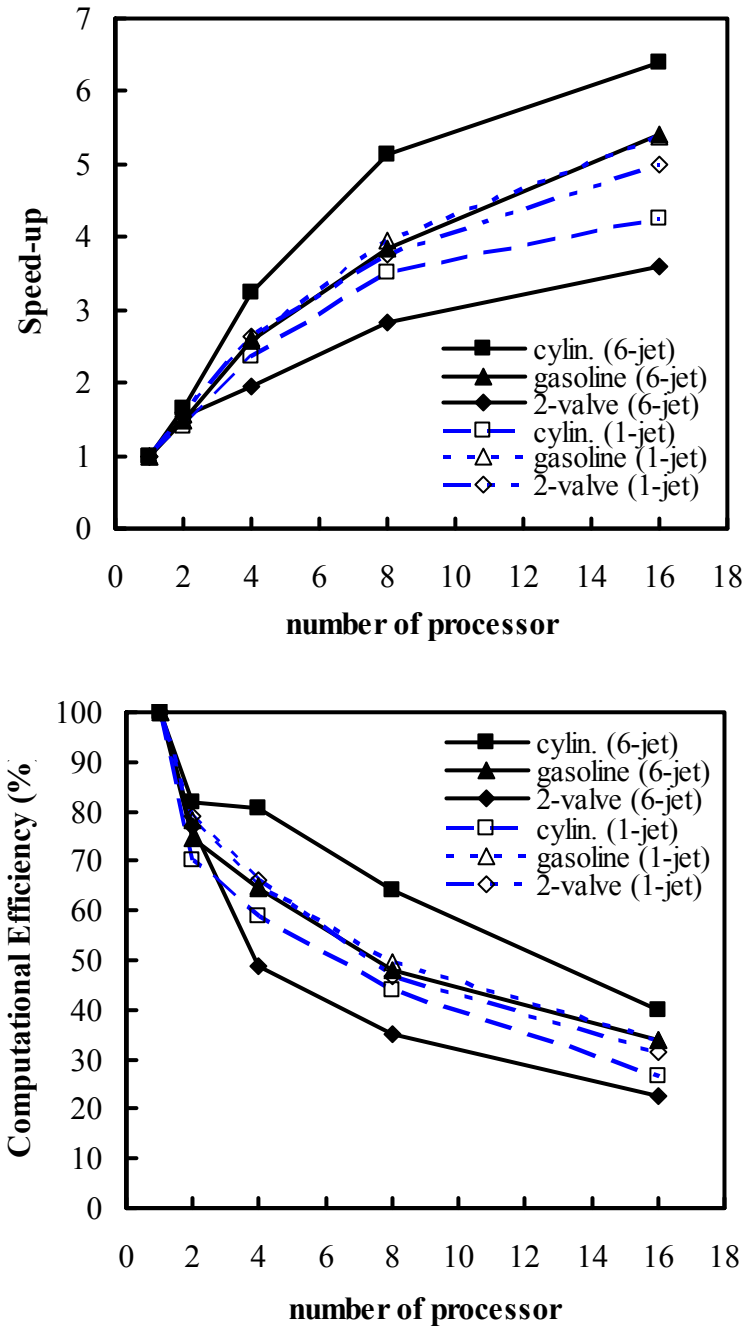

Figure 4.18. Comparisons of speed-up and computational efficiency for single-hole and six-hole injections using the coarse mesh.

Figure 4.18 shows the speed-up and computational efficiency for the 6-hole injections using the coarse meshes. Compared to the single-jet cases, the six-jet cases had mixed influences on the parallel performance for different geometries. For the cylindrical domain, a better speed-up was obtained for the six-jet injection, indicating that the six jets may promote a better partitioning of spray particles and the corresponding child cells among processors during the AMR process. By contrast, the six-jet injection in the 2-valve case resulted in a decrease in parallel performance. A possible reason for the performance decline may be because the child cells were not well distributed due to strong in-cylinder flow motion resulting from the opening and closing of the valves. Another possibility may be that the root processor was over-loaded and thus slowed down the overall performance. In addition, the 2-valve geometry suffers from extensive snapping due to the valve motion compared to the other two geometries without valve motion. On the other hand, the results of the DI gasoline engine geometry showed a similar performance for both the single-jet and the six-jet cases.

The above tests show the scalability of parallel AMR with the number of processors for different geometries. The parallel performance can also be influenced by the number of grid points of a mesh through the ratio of computation to communication. **Figure 4.19** shows the variations of the speed-up and computational efficiency, respectively, for the coarse and fine meshes (Table 4.2). The speed-up increased with the number of grid points in a domain. This was due in part to the fact that sequential overheads remain relatively constant with the

increase in the number of grid points. Consequently, the fraction of computer time designated for flow solution increased, resulting in a higher speed-up for the increased grid resolution.

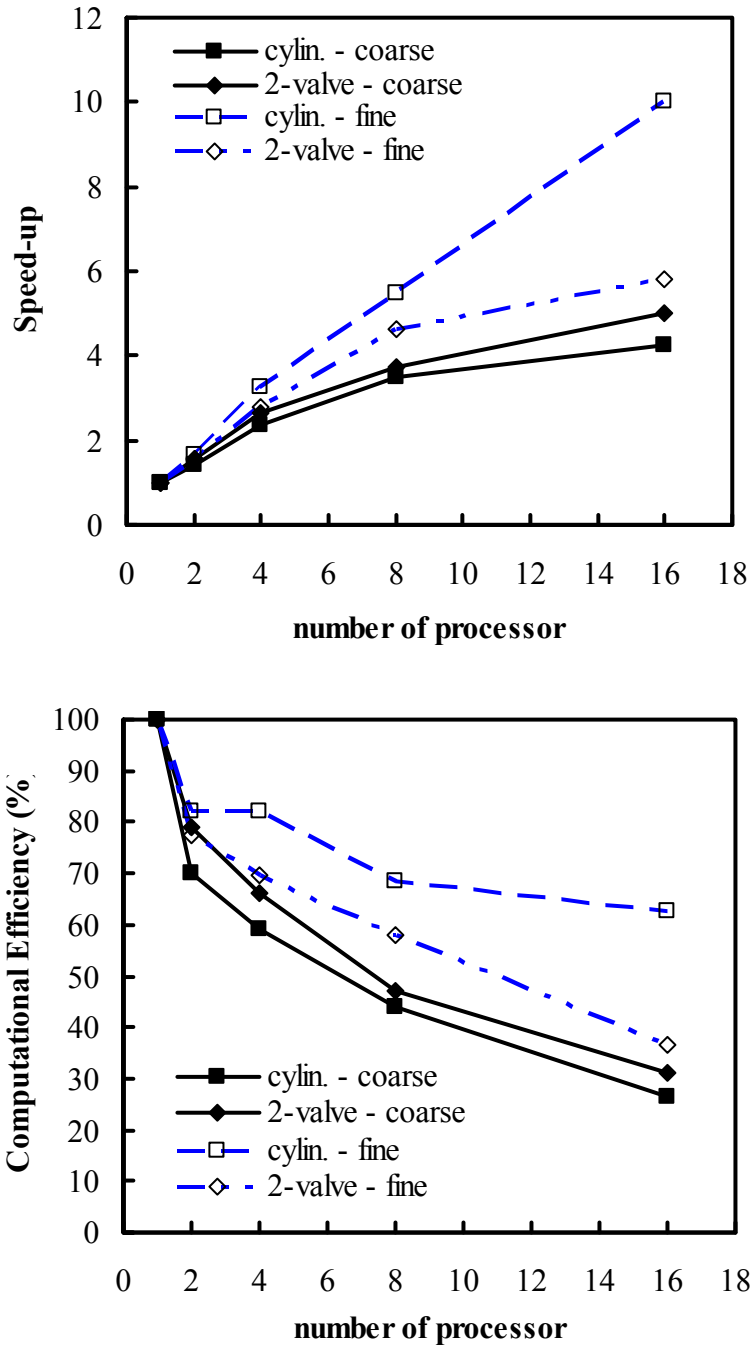

Figure 4.19. Comparisons of speed-up and computational efficiency between coarse mesh and fine mesh for using single-hole nozzle.

4.5 Gasoline Engine Simulation Using MPI-AMR

AMR was carried out on two realistic engine geometries: a 4-valve pent-roof engine and a 4-vertical-valve (4VV) engine, as shown in **Figure 4.20**. The challenges of performing AMR in these realistic geometries are twofold. First, irregular cells in the complex regions such as valves and piston in unstructured meshes pose a difficulty in defining correct connectivity data that are important to hydrodynamic calculations. Second, high aspect ratios in the irregular cells can cause the solver to be unstable.

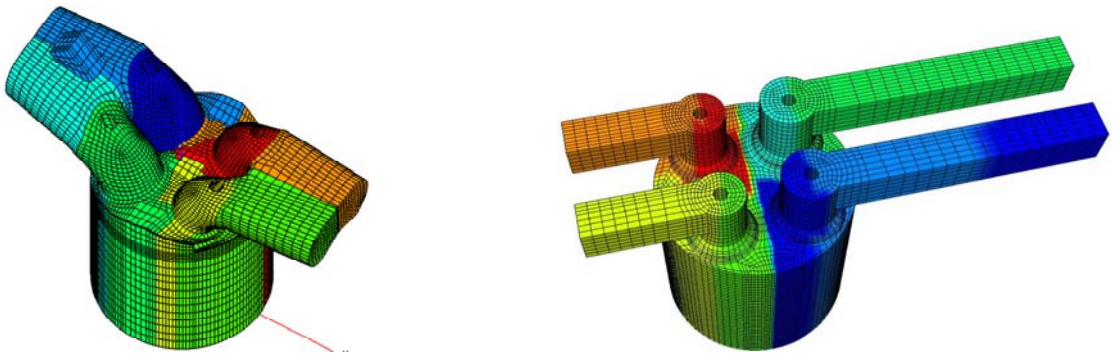

(a) A 4-valve pent-roof engine (b) A 4-vertical-valve engine

Figure 4.20. 3-D meshes of a 4-valve pent-roof engine and a 4-vertical-valve engine.

Compared to the 2-vertical-valve engine mesh, the 4-valve pent-roof mesh consists of both irregular cells around the valves and cells with higher aspect ratios. The irregular cells around the valves involve the definitions of boundary faces, edges and nodes that are critical to the application of boundary conditions. Splitting of these cells makes it more difficult to correctly define connectivity data due to possibly different scenarios of the cell splitting. The

high-aspect-ratio cells cause the solver to be unstable due to large convective fluxes in the child cells during the rezoning phase. Different scenarios of cell splitting at the valve edges were considered to fix the errors found related to the connectivity data. An alternative to address the issue related to the connectivity would be to avoid cell splitting in one layer of cells that touch the valve surfaces. The first approach was used in this study. The solver was more stable by improving the calculations of the geometric coefficients used in the diffusion calculations. This improvement results in more accurate calculations of the face volume change $(\mathbf{u}\bullet\mathbf{A})_f$ in Eq. (4.23) which is also used in the convective fluxing schemes.

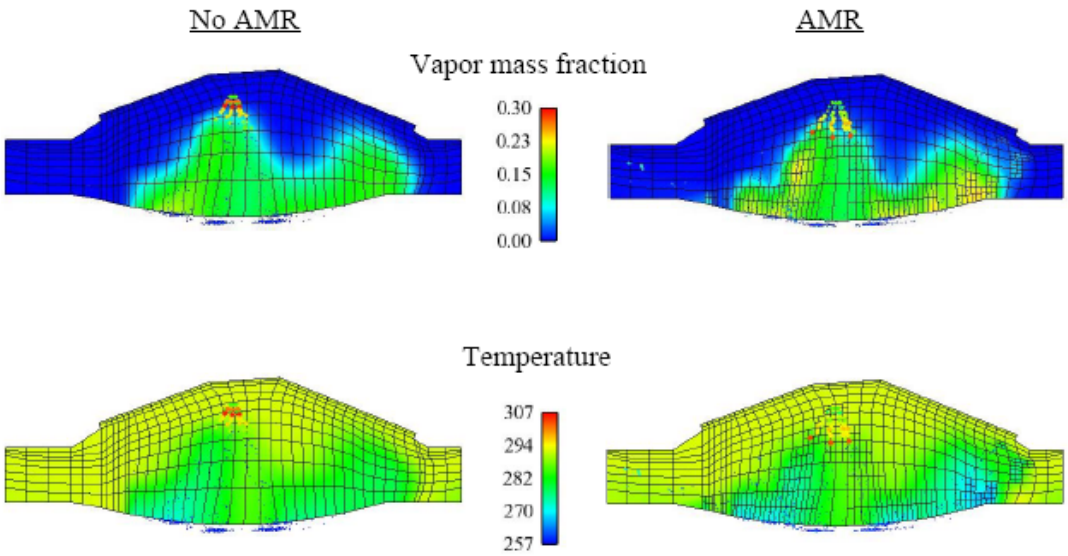

Figure 4.21. Comparisons of fuel vapor mass fraction and temperature for 4-valve pent-roof engine with and without AMR at 35 ATDC (SOI=10 ATDC).

The fuel in the 4-valve pent-roof engine was directly injected into the cylinder for testing the code robustness. The fuel was injected at 135 m/s at 10 ATDC using a 6-hole nozzle with a diameter of 200 micron. The injection duration was 48 CAD. The fuel mass was 0.07 g. The engine speed was 1500 rpm. The bore and stroke were 9.2 cm and 8.5 cm, respectively. The

standard $k-\varepsilon$ turbulence model was used along with standard spray models in KIVA-4 (i.e., TAB breakup model). The boundary conditions used the law-of-the-wall conditions. The simulation started at -15 ATDC and ended at 400 ATDC. The total cell number was 38,392 when the piston was at bottom-dead-center. **Figure 4.21** shows the comparisons of fuel vapor mass fraction and temperature at 35 ATDC for the cases with and without AMR. It is observed that AMR predicted better drop breakup due to the improved coupling from the increased spatial resolution. Fuel vapor mass fractions in the AMR case were higher in a wider region than those without AMR since the increased grid resolution in the AMR case reduced over-estimated vapor diffusion which appeared in the case without AMR, in particular, in the region right above the piston surface where the mesh was relatively coarse. The higher vapor mass fraction was also a result of more vaporization which resulted in the lower temperature in the AMR case as shown in the temperature plots. **Figure 4.22** shows the speed-up and computational efficiency, respectively. Under the current conditions, the simulations were not as efficient as those in Table 4.2 with simple geometries. Uneven particle distributions resulted from the valve motion, coarse mesh, and extensive valve snapping could be part of the reasons that attributed to the deteriorated performance. Further improvement is needed to address these issues.

The mesh for the 4-vertical-valve engine was an unstructured mesh generated by Ford Motor Company using a grid generation package **ICEM-CFD**. As with the 4-valve pent-roof mesh, many irregular cells had to be created around the valves due to the need of mesh generation topology to accommodate the 4-vertical valves. The regions with irregular cells extended from near the valves down to the piston surface. As with the 4-valve pent-roof mesh, the

splitting of cells around the valves and the piston bowl surface caused difficulties in correctly defining connectivity data; and the high-aspect-ratio cells caused the hydrodynamic calculations unstable. The improvements discussed in the case of 4-valve pent-roof mesh were also used to fix these issues.

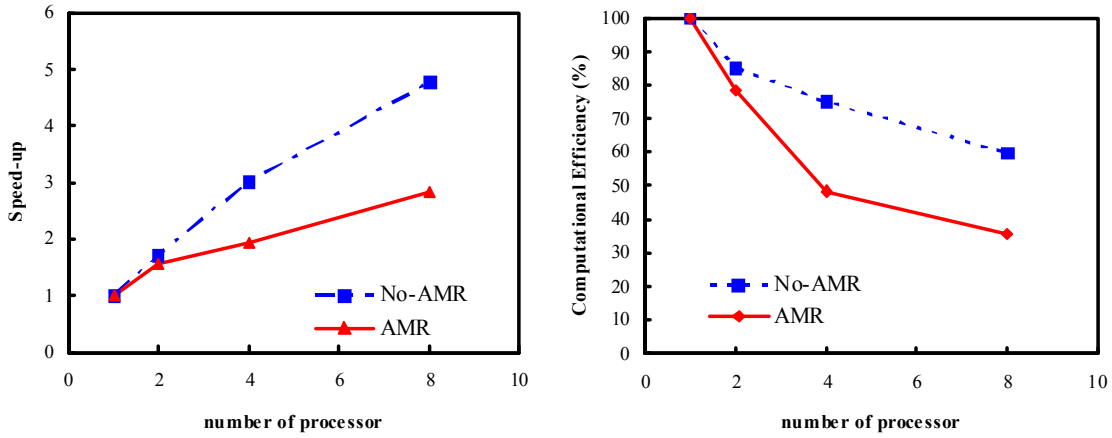

Figure 4.22. Parallel performance for 4-valve pent-roof engine with and without AMR (SOI=10 ATDC).

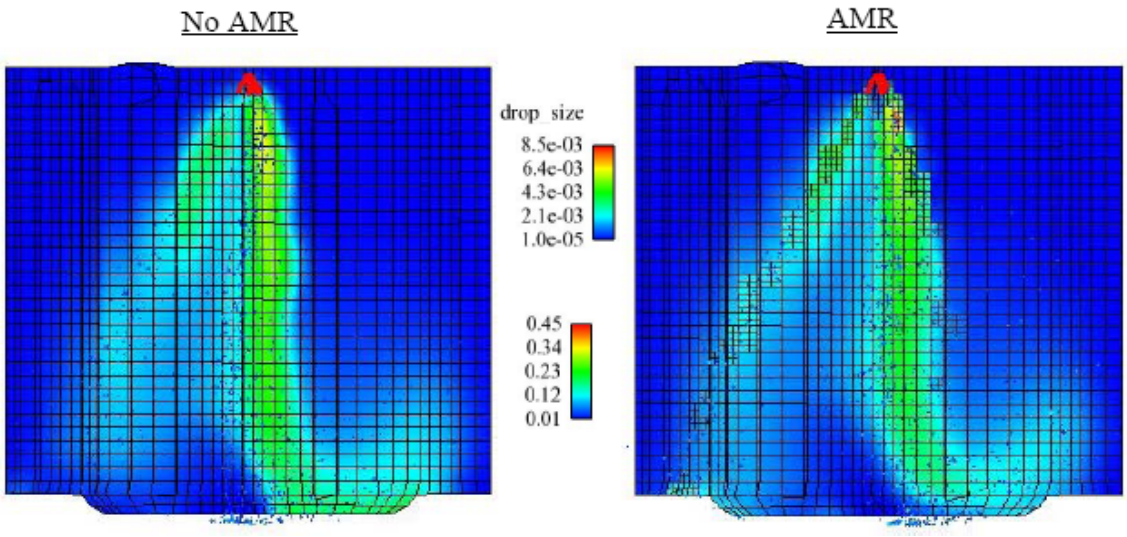

Figure 4.23. Comparisons of fuel vapor mass fraction and spray for 4-vertical-valve engine at 485 ATDC (SOI=460ATDC).

The engine bore was 103.75 mm and its stroke was 107.55 mm. The engine speed was 1,000 rpm. The fuel was injected at 135 m/s at 460 ATDC using a 6-hole nozzle with a hole diameter of 170 micron. The injection duration was 50 CAD. The fuel mass was 0.05 g. The total cell number was 81,176 when the piston was at its bottom-dead-center. The calculations started at 100 ATDC and ended at 720 ATDC. The standard $k-\varepsilon$ turbulent model and spray models were used. The boundary conditions included the law-of-the-wall conditions. **Figure 4.23** presents the comparisons of fuel vapor mass fraction at 485 ATDC for the cases with and without AMR. Due to the improved inter-phase momentum coupling resulting from the increased spatial resolution, the penetrations using AMR were predicted longer than those without AMR. As a result, more fuel vapor can be seen in the region with spray. The speed-up in parallel tests was good under the current test conditions, as can be seen in **Figure 4.24**.

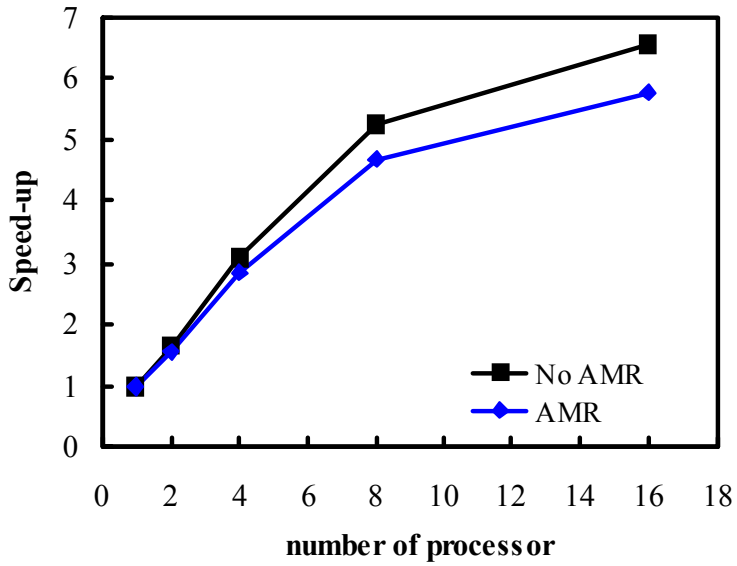

Figure 4.24. Speed-up for 4-vertical-valve engine with and without AMR (SOI=460ATDC).

In summary, the present parallel AMR algorithm was applied to simulate gasoline spray dynamics in realistic engine geometries. Results using AMR are consistent with those in the constant-volume chamber cases, i.e., AMR predicted long spray penetrations and could resolve more detailed fuel vapor structures. Although detailed in-cylinder experimental spray data are not available for model validation, it is anticipated that simulations using parallel AMR can effectively provide more accurate and detailed spray and fuel-air mixture distributions. Nonetheless, future simulations activating combustion chemistry can be performed to further compare numerical results with engine combustion data.

5 CONCLUSIONS AND RECOMMENDATIONS

5.1 Conclusions

Two major tasks have been accomplished in order to develop predictive engine simulation models based on the KIVA code. The first task was to implement the LES turbulence model coupled with detailed chemistry to simulate diesel spray combustion. The present LES adopted a one-equation dynamic structure model for the sub-grid scale stress tensor and the gradient method for the sub-grid scalar fluxes. It was found that the present models performed well in predicting the overall performance of engine combustion including the cylinder pressure history, heat release rate data, and soot and NO_x emissions trends with respect to injection timing and EGR levels. The present LES approach could also predict the unsteadiness and more detailed flow structures as compared to the RANS models. Therefore, the current LES model can be further developed into an advanced engine simulation tool to address issues such as cycle-to-cycle variations and to capture performance variations due to the subtle change in engine operating conditions or geometrical designs.

The second task was to improve spray simulation by increasing the spatial resolution of the spray region by using an adaptive mesh refinement (AMR) approach. AMR can be applied to improve the phase coupling between the gas and liquid and thus improve overall spray simulation. A grid embedding scheme was adopted in AMR to increase the spatial resolution of a hexahedral mesh. The fine grid density was coarsened if this was not needed in the spray region. These dynamic processes were controlled by using a criterion that incorporated

the normalized fuel mass and fuel vapor gradients. The grid refinement/coarsening were also parallelized based on the MPI library in memory-distributed machines.

The parallel AMR algorithm was applied to simulate transient sprays in gasoline engines. The present adaptive mesh refinement scheme was first shown to be able to produce results with the same levels of accuracy as those using the uniformly fine mesh but with much less computer time. Various spray injection conditions were tested in different geometries. In general, the computations without valve motion or using a fine mesh could give better parallel performance than those with valve motion or using a coarse mesh. Compared to the single-jet injection, the six-jet injection had mixed influences on the parallel performance for different geometries, which was considered to be related to the details of domain partitioning and local mesh refinement in different geometries. The parallelization strategy, domain partition, sprays, valve motion, and mesh density can all influence the final parallel performance. Additionally, low quality cells such as irregular cells with the high aspect-ratios in realistic engine geometries could seriously affect the robustness of the solver.

5.2 Recommendations

For the LES modeling, despite that the current sub-grid scale stress model seems to work well in a wide range of engine applications, the sub-grid scale models for scalar fluxes, turbulence-droplet interactions, and turbulence-chemistry interactions require further investigation. An improved LES wall model may also be needed to improve momentum and heat transfer modeling near walls using a RANS-type mesh. In addition, the RANS-based

spray sub-models may also need improvements in the context of LES flow field (Hu, 2008). Further improvements of the sub-models and the inter-phase couplings will be needed to reduce grid-dependent spray simulation.

The present AMR algorithm can be improved in parallel computation of complex engine geometries. Specifically, local execution of AMR on each involved process and domain re-partitioning following each adaptation may be needed to reduce communication overhead and obtain more balanced computation. It is also important to enhance the robustness of the solver in handling low quality cells that often come with meshes of realistic engine geometries.

BIBLIOGRAPHY

Abraham, J. (1997). "What is adequate resolution in the numerical computation of transient jets? ." SAE Technical Paper **970051**.

Amsden, A. A., Ramshaw, J. D., Cloutman, L. D. and O'Rourke, P. J. (1985a). Improvements and extensions to the KIVA computer program. Technical Report, Los Alamos National Laboratory. **LA-10534-MS**.

Amsden, A. A., Ramshaw, J. D., O'Rourke, P. J. and Dukowicz, J. K. (1985b). KIVA: A computer program for two- and three-dimensional fluid flows with chemical reactions and fuel sprays. Technical Report, Los Alamos National Laboratory. **LA-10245-MS**

Amsden, A. A., O'Rourke, P. J. and Butler, T. D. (1989). KIVA-II: A computer program for chemically reactive flows with sprays. Technical Report, Los Alamos National Laboratory. **LA-11560-MS**.

Amsden, A. A. (1993). KIVA-3: A KIVA Program with Block Structured Mesh for Complex Geometries. Technical Report, Los Alamos National Laboratory. **LA-12503-MS**.

Amsden, A. A. (1997). KIVA-3V: A block-structured KIVA program for engines with vertical or canted valves. Technical Report, Los Alamos National Laboratory. **LA-13313-MS**

Anderson, R. W., Elliott, N. S. and Pember, R. B. (2004). "An arbitrary Lagrangian-Eulerian method with adaptive mesh refinement for the solution of the Euler equations." Journal of Computational Physics **199**(2): 598-617.

Aneja, R. and Abraham, J. (1998). "How far does the liquid penetrate in a diesel engine: Computed results vs. measurements?" Combustion Science and Technology **138**(1-6): 233-255.

Arcoumanis, C., Gavaises, M. and French, B. (1997). "Effect of fuel injection process on the structure of diesel sprays." SAE Paper **970799**.

Are, S., Hou, S. and Schmidt, D. P. (2005). "Second-order spatial accuracy in Lagrangian-Eulerian spray calculations." Numerical Heat Transfer, Part B **48**: 25-44.

Aytekin, G. (1999). A distributed-memory implementation of KIVA-3 with refinements for Large Eddy Simulation. Ph.D. thesis, Mechanical Engineering, University of West Virginia.

Bai, C. and Gosman, A. D. (1995). "Development of methodology for spray impingement simulation." SAE Paper **950283**.

Banerjee, S., Bharadwaj, N. and Rutland, C. J. (2009). Investigation of in-cylinder mixing using Large Eddy Simulation models for LTC diesel applications. ASME International,. Milwaukee, Wisconsin, USA.

Bardina, J., Ferziger, J. H. and Reynolds, W. C. (1980). "Improved Subgrid Model for Large-Eddy Simulations." AIAA Paper **80**: 1357.

Bardina, J., Ferziger, J. H. and Reynolds, W. C. (1983). Improved Turbulence Models Based on Large Eddy Simulation of Homogeneous Incompressible, Turbulent Flows. Report TF-19, Dept. of Mechanical Engineering, Stanford University, Stanford, California.

Bauman, S. (2001). A spray model for an adaptive mesh refinement code. PhD thesis, Mathematics and Computation in Engineering, University of Wisconsin, Madison.

Baumgarten, C., Stegemann, J. and Merker, G. P. (2002). A new model for cavitation induced primary breakup of diesel sprays. ILASS-Europe. Zaragoza.

Baumgarten, C. (2006). Mixture formation in internal combustion engines. Berlin ; New York, Springer.

Beard, P., Duclos, J. M., Habchi, C., Bruneaux, G., Mokkadem, K. and Baritaud, T. (2000). "Extension of Lagrangian-Eulerian spray modeling: application to high pressure evaporating diesel spray." SAE Technical Paper **2000-01-1893**.

Bedford, K. W. and Yeo, Y. K. (1993). Conjunctive Filtering Procedures in Surface Water Flow and Transport. Large Eddy Simulation of Complex Engineering and Geophysical Flows. B. Galperin and S. A. Orszag, Cambridge University Press**:** 513-537.

Bell, J., Berger, M. J., Saltzman, J. and Welcome, M. (1994a). "Three-dimensional adaptive mesh refinement for hyperbolic conservation laws." SIAM Journal on Scientific Computing **15**: 127-138.

Bell, J., Berger, M., Saltzman, J. and Welcome, M. (1994b). "Three-Dimensional Adaptive Mesh Refinement for Hyperbolic Conservation Laws." SIAM Journal on Scientific Computing **15**: 127.

Bella, G., Bozza, F., De Maio, A., Del Citto, F. and Filippone, S. (2006). "An enhanced parallel version of KIVA-3V, coupled with a 1D CFD code, and its use in general purpose engine applications." High Performance Computing and Communications, Proceedings **4208**: 11-20.

Berg, E. v., Alajbegovic, A., Greif, D., Poredos, A., Tatschl, R., Winkelhofer, E. and Ganippa, L. C. (2002). Primary break-up model for diesel jets based on locally resolved flow field in the injection hole. ILASS-Europe. Zaragoza.

Berger, M. (1982). Adatpive mesh refinement for hyperbolic partial differential equations. PhD thesis, Computer Science Department, Stanford University.

Berger, M. and LeVeque, R. (1998). "Adaptive Mesh Refinement Using Wave-Propagation Algorithms for Hyperbolic Systems." SIAM Journal on Numerical Analysis **35**: 2298-2316.

Berger, M. J. and Oliger, J. (1984). "Adaptive Mesh Refinement for Hyperbolic Partial-Differential Equations." Journal of Computational Physics **53**(3): 484-512.

Blokkeel, G., Borghi, R. and Barbeau, B. (2003). "A 3d Eulerian model to improve the primary breakup of atomizing jet." SAE Paper **2003-01-0005**.

Boger, M., Veynante, D., Boughanem, H. and Trouve, A. (1998). Direct numerical simulation analysis of flame surface density concept for large eddy simulation of turbulent premixed combustion. 27th Symposium (International) on Combustion, The Combustion Institute. **1:** 917-926.

Brazier-Smith, P. R., Jennings, S. G. and Latham, J. (1972). "The interaction of falling water drops: coalescence." Proceedings of the Royal Society London, Series A, Mathematical and Physical Sciences **326**: 393-408.

Brennen, C. E. (1995). Cavitation and bubble dynamics. New York, Oxford University Press.

Chumakov, S. and Rutland, C. J. (2004). "Dynamic structure models for scalar flux and dissipation in large eddy simulation." AIAA Journal **42**(6): 1132-1139.

Chumakov, S. (2005). Subgrid Models for Large Eddy Simulation: Scalar Flux, Scalar Dissipation, and Energy Dissipation PhD Dissertation, Mechanical Engineering, University of Wisconsin, Madison.

Coelho, P. J. (2007). "Numerical simulation of the interaction between turbulence and radiation in reactive flows." Progress in Energy and Combustion Science **33**(4): 311-383.

Colin, O., Ducros, F., Veynante, D. and Poinsot, T. (2000). "A thickened flame model for large eddy simulations of turbulent premixed combustion." Physics of Fluids **12**: 1843.

Cook, A. W. and Riley, J. J. (1998). "Subgrid-scale modeling for turbulent reacting flows." Combustion and Flame **112**(4): 593-606.

Dan, T., Takagishi, S., Senda, J. and Fujimoto, H. G. (1997). "Organized Structure and Motion in Diesel Spray." SAE Paper **970641**.

Dec, J. E. (1997). "A conceptual model of DI diesel combustion based on laser-sheet imaging." SAE Paper **970873**.

Divis, M. and Macek, J. (2004). "Eulerian Multidimensional Model for Computing the Fuel Sprays." SAE Paper **2004-01-0537**.

Divis, M. (2005). "Fuel Injection Process Computations Using the Eulerian Multidimensional Model." SAE Paper **2005-01-1243**.

Domingo, P., Vervisch, L. and Veynante, D. (2006). Auto-ignition and flame propagation effects in LES of burned gases diluted turbulent combustion. Proceedings of the Summer Program 2006. Center for Turbulence Research, Stanford University**:** 337-348.

Drew, D. (1983). "Mathematical modeling of two-phase flow." Annual Review of Fluid Mechanics **15**(1): 261-291.

Dubief, Y. and Delcayre, F. (2000). "On coherent-vortex identification in turbulence." Journal of Turbulence **1**(1): 1-22.

Dukowicz, J. K. (1980). "A Particle-Fluid Numerical-Model for Liquid Sprays." Journal of Computational Physics **35**(2): 229-253.

Durbin, P. A. and Reif, B. A. P. (2001). Statistical theory and modeling for turbulent flows. Chichester ; New York, Wiley.

Faeth, G. M. (1977). "Current status of droplet and liquid combustion." Progress in Energy and Combustion Science **3**: 191-224.

Ferziger, J. H. and Peric, M. (2002). Computational methods for fluid dynamics. Berlin ; New York, Springer.

Filippone, S., Bella, G. and D'Ambra, P. (2002). "Parallelizating KIVA-3 to get the right simulation time in engine design." Proceedings of the IASTED International Conference, Applied Simulation and Modelling

Fox, R. O. (2003). Computational models for turbulent reacting flows. Cambridge, U.K. ; New York, Cambridge University Press.

Fujimoto, H. G., Hori, T. and Senda, J. (2009). Effect of Breakup Model on Diesel Spray Structure Simulated by Large Eddy Simulation SAE Conference. **2009-ICE-0026**.

Gavaises, M. and Tonini, S. (2006). "Prediction of liquid and vapor penetration of high pressure diesel sprays." SAE Paper **2006-01-0242**.

Georjon, T. L. and Reitz, R. D. (1999). "A drop-shattering collision model for multidimensional spray computations." Atomization and Sprays **9**(3): 231-254.

Germano, M., Piomelli, U., Moin, P. and Cabot, W. H. (1991). "A Dynamic Subgrid-Scale Eddy Viscosity Model." Physics of Fluids a-Fluid Dynamics **3**(7): 1760-1765.

Ghosal, S. and Moin, P. (1995). "The Basic Equations for the Large-Eddy Simulation of Turbulent Flows in Complex-Geometry." Journal of Computational Physics **118**(1): 24-37.

Ghosal, S. (1998). "Mathematical and Physical Constraints on LES." AIAA Journal **98-2803**.

Hallmann, M., Scheurlen, M. and Wittig, S. (1995). "Computation of Turbulent Evaporating Sprays - Eulerian Versus Lagrangian Approach." Journal of Engineering for Gas Turbines and Power-Transactions of the ASME **117**(1): 112-119.

Han, Z., Uludogan, A., Hampson, G. J. and Reitz, R. D. (1996). "Mechanism of Soot and NO_x Emission Reduction Using Multiple-Injection in a Diesel Engine." SAE Paper **960633**.

Hieber, S. (2001). An investigation of the mesh dependence of the stochastic droplet applied to dense liquid sprays. Master's Thesis, Mathematics Department, Michigan Technological Univ.

Hinze, J. O. (1975). Turbulence. New York, McGraw-Hill.

Hori, T., Senda, J., Kuge, T. and Fujimoto, H. G. (2006). "Large Eddy Simulation of Non-Evaporative and Evaporative Diesel Spray in Constant Volume Vessel by Use of KIVALES." SAE Paper **2006-01-3334**.

Hori, T., Kuge, T., Senda, J. and Fujimoto, H. G. (2008). "Effect of Convective Schemes on LES of Fuel Spray by Use of KIVALES." SAE Paper **2008-01-0930**.

Hu, B. (2008). Development of a General Diesel Combustion Model in the Context of Large Eddy Simulation. Ph.D. thesis, Mechanical Engineering, University of Wisconsin-Madison.

Huh, K. Y. and Gosman, A. D. (1991). A phenomenological model of diesel spray atomization International Conference on Multiphase Flows '91. Tsukuba, Japan.

Hunt, J. C. R., Wray, A. A. and Moin, P. (1988). Eddies, streams, and convergence zones in turbulent flows. Annual Research Briefs, Center for Turbulence Research.

Hwang, S. S., Liu, Z. and Reitz, R. D. (1996). "Breakup mechnisms and drag coefficients of high-speed vaporizing liquid drops." Atomization and Sprays **6**: 353-376.

Ibrahim, E. A., Yang, H. Q. and Przekwas, A. J. (1993). "Modeling of Spray Droplets Deformation and Breakup." Journal of Propulsion and Power **9**(4): 651-654.

Jasak, H. and Gosman, A. D. (2000a). "Automatic resolution control for the finite-volume method, Part 2: Adaptive mesh refinement and coarsening." Numerical Heat Transfer Part B-Fundamentals **38**(3): 257-271.

Jasak, H. and Gosman, A. D. (2000b). "Automatic resolution control for the finite-volume method, Part 3: Turbulent flow applications." Numerical Heat Transfer Part B-Fundamentals **38**(3): 273-290.

Jhavar, R. and Rutland, C. J. (2006). "Using Large Eddy Simulations to Study Mixing Effects in Early Injection Diesel Engine Combustion." SAE Paper **06P-556**.

Jones, W. P. and Launder, B. E. (1972). "Prediction of Laminarization with a 2-Equation Model of Turbulence." International Journal of Heat and Mass Transfer **15**(2): 301-&.

Karypis, G. and Kumar, V. (1998a). "A fast and high quality multilevel scheme for partitioning irregular graphs." SIAM Journal on Scientific Computing **20**(1): 359-392.

Karypis, G. and Kumar, V. (1998b). Multi-level k-way hypergraph partitioning. Technical Report, Department of Computer Science, University of Minnesota. **TR 98-036**.

Klingbeil, A., Juneja, H., Ra, Y. and Reitz, R. D. (2003). "Premixed Diesel Combustion Analysis in a Heavy-Duty Diesel Engine." SAE Paper **2003-01-0341**.

Kolakaluri, R., Li, Y. H. and Kong, S.-C. (2009). "A Unified Spray Model for Engine Spray Simulation Using Dynamic Mesh Refinement." International Journal of Multiphase Flow (in review).

Kong, S.-C., Han, Z. and Reitz, R. D. (1995). "The Development and Application of a Diesel Ignition and Combustion Model for Multidimensional Engine Simulation." SAE Technical Paper **950278**.

Kong, S.-C., Senecal, P. K. and Reitz, R. D. (1999). "Developments in spray modelling in diesel and direct-injection gasoline engines." Oil & Gas Science and Technology - Rev. IFP **54**(2): 197-204.

Kong, S.-C. (2007). "Drop/Wall Interaction Criteria and Their Applications in Diesel Spray Modeling." Atomization and Sprays **17**(6): 473.

Kong, S.-C., Sun, Y. and Rietz, R. D. (2007a). "Modeling diesel spray flame liftoff, sooting tendency, and NO_x emissions using detailed chemistry with phenomenological soot model." Journal of Engineering for Gas Turbines and Power-Transactions of the ASME **129**(1): 245-251.

Kong, S.-C., Kim, H., Reitz, R. D. and Kim, Y. (2007b). "Comparisons of diesel PCCI combustion simulations using a representative interactive flamelet model and direct integration of CFD with detailed chemistry." Journal of Engineering for Gas Turbines and Power-Transactions of the ASME **129**(1): 252-260.

Kuensberg, S. C., Kong, S.-C. and Reitz, R. D. (1999). "Modeling the effects of injector nozzle geometry on diesel sprays." SAE Paper **1999-01-0912**.

Kuo, K. (1986). Principles of combustion, Wiley New York.

Launder, B. E. (1996). "Advanced turbulence models for industrial applications." Turbulence and transition modelling 163-192.

Law, C. (2006). Combustion physics, Cambridge University Press.

Lebas, R., Blokkeel, G., Beau, P.-A. and Demoulin, F. X. (2005). "Coupling vaporization model with the Eulerian-Lagrangian spray atomization (ELSA) model in diesel engine conditions." SAE Paper **2005-01-0213**.

Lee, S. H. and Ryou, H. S. (2001). "Development of a new model and heat transfer analysis of impinging diesel sprays on a wall." Atomization and Sprays **11**(1): 85-105.

Leonard, A. (1997). "Large Eddy Simulation of Chaotic Convection and Beyond." AIAA Paper **97-0204**.

Li, Y. H. and Kong, S.-C. (2008). "Diesel combustion modelling using LES turbulence model with detailed chemistry." Combustion Theory and Modelling **12**(2): 205-219.

Li, Y. H., Kong, S.-C. and Torres, D. J. (2008). Parallel KIVA-4 in Realistic Geometries. 18th International Multidimensional Engine Modeling User's Group Meeting at the SAE Congress. Detroit, MI.

Li, Y. H. and Kong, S.-C. (2009a). "Integration of parallel computation and dynamic mesh refinement for transient spray simulation." Computer Methods in Applied Mechanics and Engineering **198**(17-20): 1596-1608.

Li, Y. H. and Kong, S.-C. (2009b). "Mesh refinement algorithms in an unstructured solver for multiphase flow simulation using discrete particles." Journal of Computational Physics (in press), DOI: 10.1016/j.jcp.2009.05.018.

Libby, P. A. and Williams, F. A. (1980). Turbulent reacting flows, Springer-Verlag.

Lilly, D. K. (1992). "A Proposed Modification of the Germano-Subgrid-Scale Closure Method." Physics of Fluids a-Fluid Dynamics **4**(3): 633-635.

Lippert, A. M., Chang, S., Are, S. and Schmidt, D. P. (2005). "Mesh independence and adaptive mesh refinement for advanced engine spray simulations." SAE Technical Paper **2005-01-0207**.

Liu, A. B. and Reitz, R. D. (1993). "Modeling the effects of drop drag and breakup on fuel sprays." SAE Paper **930072**.

Liu, S. W., Meneveau, C. and Katz, J. (1994). "On the Properties of Similarity Subgrid-Scale Models as Deduced from Measurements in a Turbulent Jet." Journal of Fluid Mechanics **275**: 83-119.

Loth, E. (2000). "Numerical approaches for motion of dispersed particles, droplets and bubbles." Progress in Energy and Combustion Science **26**(3): 161-223.

Magnussen, B. F. and Hjertager, B. H. (1977). "On mathematical modeling of turbulent combustion with special emphasis on soot formation and combustion." 16th Symposium (International) on Combustion: 719-729.

Magnussen, B. F. (1981). On the structure of turbulence and a generalized eddy dissipation concept for chemical reaction in turbulent flow. 19th AIAA Aerospace Meeting. St. Louis, Missouri, USA.

Meneveau, C., Lund, T. S. and Cabot, W. H. (1996). "A Lagrangian dynamic subgrid-scale model of turbulence." Journal of Fluid Mechanics **319**: 353-385.

Menon, S., Yeung, P. K. and Kim, W. W. (1996). "Effect of subgrid models on the computed interscale energy transfer in isotropic turbulence." Computers & Fluids **25**(2): 165-180.

Menon, S. and Pannala, S. (1997). "Subgrid modeling of unsteady two-phase turbulent flows." AIAA Paper **97**: 3113.

Moin, P., Squires, K., Cabot, W. and Lee, S. (1991). "A Dynamic Subgrid-Scale Model for Compressible Turbulence and Scalar Transport." Physics of Fluids a-Fluid Dynamics **3**(11): 2746-2757.

Naber, J. D. and Reitz, R. D. (1988). "Modeling engine spray/wall impingement " SAE Paper **880107**.

Nishimura, A. and Assanis, D. N. (2000). A model for primary diesel fuel atomization based on cavitation bubble collapse energy. 8th International Conference on Liquid Atomization and Spray Systems (ICLASS)**:** 1249-1256.

Nordin, N. (2001). Complex chemistry modeling of diesel spray combustion. Ph.D. thesis, Mechanical Engineering, Chalmers University of Technology.

Nurick, W. H. (1976). "Orifice cavitation and its effect on spray mixing." Journal of Fluids Engineering **98**: 681-687.

O'Rourke, P. and Amsden, A. A. (2000). "A Spray/Wall Interaction Submodel for the KIVA-3 Wall Film Model." SAE Paper **2000-01-0271**.

O'Rourke, P. J. and Bracco, F. V. (1980). "Modelling of drop interactions in thick sprays and a comparison with experiments." Proceedings of the Institution of Mechanical Engineers Part C-Journal of Mechanical Engineering Science **9**: 101-116.

O'Rourke, P. J. and Amsden, A. A. (1987). "The TAB method for numerical calculation of spray droplet breakup." SAE Paper **872089**.

Pai, M. G. and Subramaniam, S. (2006). "Modeling interphase turbulent kinetic energy transfer in Lagrangian-Eulerian spray computations." Atomization and Sprays **16**(7): 807-826.

Park, S. W., Kim, H. J. and Lee, C. S. (2002). An experimental and numerical study on atomization characteristics of gasoline injector for direct injection engine. 15th Annual conference on Liquid Atomization and Spray Systems, ILASS-Americas. **:** 47-51.

Patel, A., Kong, S.-C. and Reitz, R. D. (2004). "Development and validation of a reduced reaction mechanism for HCCI engine simulations." SAE Paper **2004-01-0558**.

Patterson, M. A. and Reitz, R. D. (1998). "Modelling the effect of fuel spray characteristics on diesel engine combustion and emission." SAE Paper **980131**.

Pember, R., Bell, J., Colella, P., Crutchfield, W. and Welcome, M. (1995). "An adaptive Cartesian grid method for unsteady compressible flow in irregular regions." Journal of Computational Physics **120**(2): 278–304.

Peters, N. (1984). "Laminar Diffusion Flamelet Models in Non-Premixed Turbulent Combustion." Progress in Energy and Combustion Science **10**(3): 319-339.

Peters, N. (2000). Turbulent combustion. Cambridge, U.K.; New York, Cambridge University Press.

Pickett, L. M. and Siebers, D. L. (2004). "Soot in diesel fuel jets: effects of ambient temperature, ambient density, and injection pressure." Combustion and Flame **138**(1-2): 114-135.

Piomelli, U., Cabot, W. H., Moin, P. and Lee, S. S. (1991). "Subgrid-Scale Backscatter in Turbulent and Transitional Flows." Physics of Fluids a-Fluid Dynamics **3**(7): 1766-1771.

Piomelli, U. and Liu, J. H. (1995). "Large-Eddy Simulation of Rotating Channel Flows Using a Localized Dynamic-Model." Physics of Fluids **7**(4): 839-848.

Pitsch, H. (2005). "A consistent level set formulation for large-eddy simulation of premixed turbulent combustion." Combustion and Flame **143**(4): 587-598.

Pitsch, H. (2006). "Large-eddy simulation of turbulent combustion." Annual Review of Fluid Mechanics **38**: 453-482.

Poinsot, T. and Veynante, D. (2001). Theoretical and numerical combustion. Philadelphia, PA, R.T. Edwards.

Pomraning, E. (2000). Development of Large Eddy Simulation Turbulence Models. PhD thesis, Mechanical Engineering, University of Wisconsin Madison.

Pomraning, E. and Rutland, C. J. (2002). "A Dynamic One-Equation Non-Viscosity LES Model." AIAA Journal **44**: 689--701.

Pope, S. B. (2000). Turbulent flows. Cambridge ; New York, Cambridge University Press.

Reitz, R. D. and Bracco, F. V. (1986). "Mechanisms of Breakup of Round Liquid Jets " In Encyclopedia of Fluid Mechanics, Gulf Pub, NJ **3**: 233-249.

Reitz, R. D. (1987). "Modeling atomization processes in high-pressure vaporizing sprays." Atomisation and Spray Technology **3**: 309-337.

Reitz, R. D. and Diwakar, R. (1987). "Structure of high-pressure fuel sprays." SAE Paper **870598**.

Reynolds, W. C. (1980). Modeling of fluid motions in engines-an introductory overview. Combustion modeling in reciprocating engines. J. N. Mattavi and C. A. Amann, Plenum Press**:** 41-68.

Sazhin, S. (2006). "Advanced models of fuel droplet heating and evaporation." Progress in Energy and Combustion Science **32**(2): 162-214.

Schmidt, D. P., Nouar, I., Senecal, P. K., C.J.Rutland, Martin, J. K., Reitz, R. D. and Hoffman, J. A. (1999). "Pressure-swirl atomization in the near field." SAE Paper **1999-01-0496**.

Schmidt, D. P. and Rutland, C. J. (2000). "A new droplet collision algorithm." Journal of Computational Physics **164**(1): 62-80.

Schmidt, D. P. and Rutland, C. J. (2004). "Reducing grid dependency in droplet collision modeling." Journal of Engineering for Gas Turbines and Power-Transactions of the ASME **126**(2): 227-233.

Senecal, P. K., Schmidt, D. P., Nouar, I., Rutland, C. J., Reitz, R. D. and Corradini, M. L. (1999). "Modeling high-speed viscous liquid sheet atomization." International Journal of Multiphase Flow **25**(6-7): 1073-1097.

Shotorban, B. and Mashayek, F. (2005). "Modeling subgrid-scale effects on particles by approximate deconvolution." Physics of Fluids **17**(8).

Sinnamon, J. F., Lancaster, D. R. and Stiner, J. C. (1980). "An experimental and analytical study of engine fuel spray trajectories." SAE Paper **800135**.

Sirignano, W. A. (1986). "The Formulation of Spray Combustion Models - Resolution Compared to Droplet Spacing." Journal of Heat Transfer-Transactions of the ASME **108**(3): 633-639.

Smagorinsky, J. (1963). "General Circulation Experiments with the Primitive Equations." Monthly Weather Review **93**: 99-164.

Smith, G. P., Golden, D. M., Frenklach, M., Moriarty, N. W., Eiteneer, B., Goldenberg, M., Bowman, C. T., Hanson, R. K., Song, S., Gardiner, W. C., Lissianski, V. V. and Qin, Z. (2000). http://www.me.berkeley.edu/gri-mech/.

Spalding, D. (1981). "A general purpose computer program for multidimensional one and two phase flow." Mathematics and Computers in Simulation **23**(3): 267-276.

Spalding, D. B. (1977). Development of the eddy-break-up model of turbulent combustion. 16th Symposium (International) on Combustion Cambridge, Massachusetts, USA**:** 1657-1663.

Stalsberg-Zarling, K., Feigl, K., Tanner, F. X. and Larmi, M. J. (2004). "Momentum coupling by means of Lagrange polynomials in the CFD simulation of high-velocity dense sprays." SAE Paper **2004-01-0535**.

Stanton, D. W. and Rutland, C. J. (1996). "Modelling fuel film formation and wall interaction in diesel engines." SAE Paper **960628**.

Stiesch, G. (2003). Modeling engine spray and combustion processes. Berlin ; New York, Springer.

Subramaniam, S. and O'Rourke, P. J. (1998). Numerical convergence of the KIVA-3 code for sprays and its implications for modeling. Technical Report, Los Alamos National Laboratory. **LAUR 98-5465**.

Tamin, J. and Hallett, W. L. H. (1995). "A continuous thermodynamics model for multicomponent droplet vaporization." Chemical Engineering Science **50**(18): 2933-2942.

Tannehill, J. C., Anderson, D. A. and Pletcher, R. H. (1997). Computational fluid mechanics and heat transfer. Washington, DC, Taylor & Francis.

Tanner, F. X. (1997). "Liquid Jet atomization and droplet breakup modeling of non-evaprating diesel fuel sprays." SAE Paper **970050**.

Taylor, G. I. (1963). "The instability of liquid surfaces when accelerated in a direction perpendicular to their planes." In Batchelor GK (1963) The Scientific Papers of Sir Geoffery Ingram Taylor **3**: 532-536.

Tennekes, H. and Lumley, J. L. (1972). A first course in turbulence. Cambridge, Mass., MIT Press.

Tennison, P. J., Georjon, T. L., Farrell, P. V. and Reitz, R. D. (1998). "An experimental and numerical study of sprays from a common rail injection system for use in an HSDI diesel engine." SAE Paper **980810**.

Tonini, S., Gavaises, M. and Theodorakakos, A. (2008). "Modelling of high-pressure dense diesel sprays with adaptive local grid refinement." International Journal of Heat and Fluid Flow **29**(2): 427-448.

Torres, D. J., O'Rourke, P. J. and Amsden, A. A. (2003). "Efficient multicomponent fuel algorithm." Combustion Theory and Modelling **7**(1): 67-86.

Torres, D. J. and Trujillo, M. F. (2006). "KIVA-4: An unstructured ALE code for compressible gas flow with sprays." Journal of Computational Physics **219**(2): 943-975.

Torres, D. J., Li, Y. and Kong, S.-C. (2009). "Partitioning Strategies for Parallel KIVA-4 Engine Simulations." Computers and Fluids (accepted).

Tsui, Y. Y. and Pan, Y. F. (2006). "A pressure-correction method for incompressible flows using unstructured meshes." Numerical Heat Transfer Part B-Fundamentals **49**(1): 43-65.

Van Leer, B. (1979). "Towards the Ultimate Conservative Difference Scheme 5. 2nd-Order Sequel to Godunovs Method." Journal of Computational Physics **32**(1): 101-136.

Vreman, A. W., Geurts, B. J. and Kuerten, J. G. M. (1994). "Direct and Large-Eddy Simulation VI." P. R. Voke, L. Kleiser, and J.-P. Chollet, Eds., Kluwer Academic Publishers: 133--144.

Wang, Y. and Peters, N. (1997). "Applications of the cross-sectional average method to calculations of the dense spray region in a diesel engine." SAE Paper **972866**.

Wang, Z. J. and Chen, R. F. (2002). "Anisotropic solution-adaptive for turbulent viscous Cartesian grid method flow simulation." AIAA Journal **40**(10): 1969-1978.

Watkins, A. P. (1987). "Computation of diesel sprays by a non-iterative implicit solution scheme." Atomisation and Spray Technology **3**: 261-290.

Wiedenhoefer, J. and Reitz, R. (2003). "Multidimensional Modelling of the Effects of Radiation and Soot Deposition in Heavy-Duty Diesel Engines." SAE Paper **2003-01-0560**.

Wilcox, D. C. (1993). Turbulence modeling for CFD, La Canada, California: DCW industries Inc.

Yasar, O., Zacharia, T., Aggarwal, R., Amsden, A. A. and Baumgardner, J. R. (1995). Implementation of KIVA-3 on distributed memory MIMD computers. Technical Report. **CONF-950431-2**.

Yeo, W. K. (1987). A Generalized High Pass/Low Pass Averaging Procedure for Deriving and Solving Turbulent Flow Equations. Ph.D. thesis, The Ohio State University.

Yoshizawa, A. and Horiuti, K. (1985). "A Statistically-Derived Subgrid-Scale Kinetic-Energy Model for the Large-Eddy Simulation of Turbulent Flows." Journal of the Physical Society of Japan **54**(8): 2834-2839.

Zhang, L. and Kong, S.-C. (2009). "Modeling of Multi-Component Fuel Vaporization and Combustion in Internal Combustion Engines." Chemical Engineering Science (accepted for publication).

Zolver, M., Klahr, D., Bohbot, J., Laget, O. and Torres, A. (2003). "Reactive CFD in Engines with a new unstructured parallel solver." Oil & Gas Science and Technology - Rev. IFP **58**(1): 33-46.